Rafael de Camargo Catapan

MODELAGEM MULTIESCALA DAS REAÇÕES DE REFORMA A VAPOR DE ETANOL E DE DESLOCAMENTO ÁGUA-GÁS SOBRE NÍQUEL

Tese de Doutorado apresentada ao Programa de Pós-Graduação em Engenharia Mecânica da Universidade Federal de Santa Catarina para obtenção do grau de Doutor em Engenharia Mecânica

Orientador: Prof. Amir Antônio Martins de Oliveira Jr, Ph.D.

Florianópolis
2012

Catalogação na fonte pela Biblioteca Universitária
da
Universidade Federal de Santa Catarina

C357m Catapan, Rafael de Camargo
Modelagem multiescala das reações de reforma a vapor de etanol e de deslocamento água-gás sobre níquel [tese] / Rafael de Camargo Catapan ; orientador, Amir Antônio Martins de Oliveira Jr. - Florianópolis, SC, 2012.
158 p.: il., grafs., tabs.

Tese (doutorado) - Universidade Federal de Santa Catarina, Centro Tecnológico. Programa de Pós-Graduação em Engenharia Mecânica.

Inclui referências

1. Engenharia mecânica. 2. Álcool. 3. Hidrogênio. 4. Catálise heterogênea. I. Oliveira Junior, Amir Antonio Martins de. II. Universidade Federal de Santa Catarina. Programa de Pós-Graduação em Engenharia Mecânica. III. Título.

CDU 621

Rafael de Camargo Catapan

MODELAGEM MULTIESCALA DAS REAÇÕES DE REFORMA A VAPOR DE ETANOL E DE DESLOCAMENTO ÁGUA-GÁS SOBRE NÍQUEL

Esta Tese foi julgada adequada para obtenção do Título de "Doutor em Engenharia Mecânica", e aprovada em sua forma final pelo Programa de Pós Graduação em Engenharia Mecânica.

Florianópolis, 20 de abril de 2012.

_____
Prof. Júlio César Passos, Dr.
Coordenador do Curso

_____
Prof. Amir Antônio Martins de Oliveira Jr., Ph.D.
Orientador
Universidade Federal de Santa Catarina

Banca Examinadora:

_____
Prof. Amir Antônio Martins de Oliveira Jr., Ph.D.
Presidente

_____
Prof.ª Patrícia Regina Pereira Barreto, Dr.ª
Relatora
Instituto Nacional de Pesquisas Espaciais

_____
Prof.ª Soraia Teixeira Brandão, Dr.ª
Universidade Federal da Bahia

_____
Prof. Luismar Marques Porto, Ph.D.
Universidade Federal de Santa Catarina

_____
Prof. Giovanni Finoto Caramori, Dr.
Universidade Federal de Santa Catarina

_____
Prof. Jader Riso Barbosa, Ph.D.
Universidade Federal de Santa Catarina

Este trabalho é dedicado à minha esposa Josiane e ao meu amigo Elio. Tenho a absoluta certeza de que eu não estaria aqui se não fosse por eles.

AGRADECIMENTOS

Gostaria de agradecer aos que estivem presentes nestes últimos tempos. Ao seu jeito, todos contribuíram para que eu conseguisse. Por isso, são sinceros os meus agradecimentos:

Aos meus familiares, em especial a minha esposa Josiane que sempre me apoiou.

Ao professor Amir Oliveira pela orientação e amizade.

Ao professor Dion Vlachos da Universidade de Delaware pela sua orientação e disponibilidade de recursos para a minha estada.

Ao Conselho Nacional de Desenvolvimento Científico e Tecnológico (CNPq) pela bolsa de doutorado e de doutorado sanduíche (processos 140562/2007-9 and 201653/2009-5).

To Catalysis Center for Energy Innovation, an Energy Frontier Research Center funded by the U.S. Department of Energy, Office of Science, Office of Basic Energy Sciences under Award Number DE-SC0001004.

A todos os amigos do LabCET, UFSC e de Newark.

Ao Elio de Mello Castanho pelo constante incentivo e inspiração.

You take the blue pill - the story ends, you wake up in your bed and believe whatever you want to believe. You take the red pill - you stay in Wonderland and I show you how deep the rabbit-hole goes.

Morpheus.

RESUMO

A presente tese consiste na modelagem multiescala e na análise das reações de reforma a vapor de etanol e de deslocamento água-gás sobre níquel. Foram usadas duas técnicas diferentes de modelagem para estudar os fenômenos que ocorrem nas diferentes escalas de comprimento. Em nível atômico e molecular, a análise das reações elementares foi realizada utilizando o programa SIESTA. Este programa utiliza a da teoria do funcional da densidade para encontrar as soluções da equação de Schrödinger e correlacioná-las com as propriedades de um sistema tais como as energias de ligação entre as espécies químicas e a superfície do níquel e as energias das estruturas de transição das reações elementares. Já no nível macroscópico, um mecanismo de cinética detalhada de reação em superfície foi desenvolvido com base nas mais recentes técnicas de modelagem. Este mecanismo foi inserido na rotina de um código de cinética química (SURFACE CHEMKIN) e seus resultados foram comparados com uma série de medições relatadas na literatura. Para fazer tal comparação, os reatores descritos na literatura foram representados com o modelo de reator tubular de leito empacotado com escoamento de fluxo pistonado. A taxa de reação superficial foi calculada pelo mecanismo detalhado desenvolvido. Os resultados em nível molecular da reação de deslocamento água-gás sobre as superfícies de Ni (111) e (211) sugerem que a superfície (111) é ligeiramente mais ativa. No entanto, esta superfície tem uma atividade mais baixa para a quebra da ligação C-O, sendo, portanto, menos suscetível à desativação por deposição de carbono. Estas conclusões são confirmadas pela análise dos resultados do mecanismo detalhado. As previsões do mecanismo detalhado para a reforma a vapor de etanol estão de acordo com as medições descritas na literatura nas condições experimentais estudadas. Os resultados indicam que a superfície de níquel é preenchida principalmente pelas espécies CHCH e CCOOH, e que estas espécies têm uma influência significativa sobre a atividade do catalisador. A população destas duas espécies é governada pela proporção de água e etanol na entrada do reator. A análise do caminho de reação mostra que a seguinte sequência de reações elementares é favorecida sobre níquel: $CH_3CH_2OH \rightarrow CH_3CH_2O \rightarrow CH_3CHO \rightarrow CH_3CO \rightarrow CH_3 + CO$ ou $CH_3CO \rightarrow CH_3C \rightarrow CH_2C \rightarrow CH_2CH \rightarrow CHCH \rightarrow$

$2CH \rightarrow CHO \rightarrow CO \rightarrow CO_2$. A água é decomposta em oxigênio atômico, que é responsável pela oxidação de espécies menores tais como o CH e o CO. O resultado principal da presente tese é um mecanismo detalhado de reação superficial de reforma de etanol sobre níquel composto por 205 reações elementares que ocorrem entre 70 espécies químicas. Este mecanismo é uma ferramenta poderosa para ser usada em projeto de reatores, *e.g.*, utilizando códigos de CFD tais como o CHEMKIN.

Palavras chave: etanol, hidrogênio, catálise heterogênea, modelagem multiescala.

ABSTRACT

The present thesis consists of the multiscale modeling and analysis of the steam reforming of ethanol (SRE) and water-gas shift (WGS) reactions on Ni catalysts. Two different modeling techniques were applied to represent the different length scales. At the atomic and molecular level, the SIESTA package was applied to study the elementary-like reactions. SIESTA employs the *Density Functional Theory* (DFT) to find the solutions of the Schrödinger equation, correlating them with adsorption proprieties of the system. The mean field assumption, *i.e.*, considering adsorbates and reactions homogenously distributed over the catalyst particle, was evoked to develop a microkinetic model based on the recent techniques and concepts. The resulting mechanism was used within the SURFACE CHEMKIN framework and its results were compared to measurements at the macroscopic level reported in the literature. In order to do this, the reactors reported in the literature were modeled by a packed bed plug flow reactor model. Specifically, the DFT results of the WGS reaction on Ni (111) and Ni (211) surfaces suggest that the flat surface is slightly more active for the WGS reaction. Ni (111) has a much lower activity for C-O bond breaking, and thus, flat surfaces are less susceptible to deactivation by coking. These conclusions are supported by the microkinetic analysis. Model predictions of the SRE agree with the measurements in the range of experimental conditions analyzed. Mostly, CHCH and CCOOH species populate the surface and they have a significant influence on the activity of this catalyst. The population of these two species is governed by the ratio of water/ethanol. The reaction path analysis shows that the SRE follows: $CH_3CH_2OH \rightarrow CH_3CH_2O \rightarrow CH_3CHO \rightarrow CH_3CO \rightarrow CH_3 + CO$ or $CH_3CO \rightarrow CH_3C \rightarrow CH_2C \rightarrow CH_2CH \rightarrow CHCH \rightarrow 2CH \rightarrow CHO \rightarrow CO \rightarrow CO_2$. Water is mostly decomposed into atomic oxygen, which is responsible for oxidizing C1 species CH and CO. The main outcome of the present thesis is a surface reaction mechanism composed of 205 elementary-like steps among 70 adsorbates to represent the steam reforming of ethanol and the WGS reactions. This detailed surface reaction mechanism is a powerful tool to be used in reactor design, *e.g.*, using CFD codes such as CHEMKIN.

Keywords: ethanol, hydrogen, heterogeneous catalysis, multiscale modeling

LIST OF FIGURES

LIST OF TABLES

LIST OF SYMBOLS

C1	Group of chemical species with one carbon atom
C2	Group of chemical species with two carbon atoms
R	Chemical reaction, elementary-like step
S	Sticking coefficient
$A_{f,j}$	Pre-exponential factor
$E_{a,f,j}$	Activation energy
ΔH_j°	Enthalpy of the surface reaction
ΔS_j°	Entropy of the surface reaction
k_B	Boltzmann's constant
T	Temperature
h	Planck's constant
R	Ideal gas constant
G	Gibbs energy
H	Enthalpy
S	Entropy
k	Reaction constant
β_j	Temperature exponent
Γ	Concentration of binding sites
n	Number of reactants that are surface species (including vacancies)
Z_w	Flux of molecules
N_A	Avogadro's number
P_k	Partial pressure
W_k	Molecular weight of the k^{th} species
$K_{c,j}$	Equilibrium constant in concentration units
ν_{ij}	Stoichiometric coefficient of species i in reaction j
$K_{p,j}$	Thermodynamic equilibrium constant
E	Energy
α_{ik}	The lateral interaction parameter of species k on species i
ε_{jk}	Lateral interaction of species k on the barrier of reaction j.
θ_k	Coverage of species k
ω_j	Proximity factor
ΔZPE_i	Zero point energy correction
$H_i^{gas}(T_0)$	Enthalpy of formation in gas-phase at T_0
C_p	Heat capacity at constant pressure
Θ_{vk}	Characteristic vibrational temperature

ν_k	Vibrational frequency
M_{ads}	Mass of one adsorbate
N_{sites}	Number of sites occupied by the adsorbates
A	Area of one site, intercept of the BEP correlation
B	Slope of the BEP correlation
$\gamma(x)$	Relates to the valence of A
x_{max}	Maximum number of hydrogen atoms that can bond to A
ξ	Interception
δ_i	Temperature dependency parameter
$S_{3D,trans}(T_0)$	Translational contribution to the entropy
F_{loc}	Fraction of the rotational and vibrational contributions to entropy
$\dot{r}_i$	Net production rate of species i
$\dot{q}_j$	Production rate of the j^{th} elementary-like step
$[C_i]$	Concentration of species i
RP_{ij}	Fraction of either net production or net consumption rate
PE_j	Partial equilibrium ratio
$X_{rc,j}$	Campbell 's degree of rate control
f_i	Enthalpy or entropy of adsorbate i
X	Overall conversion
α_i	Reaction order with respect to the reactant i
$E_{a,app}$	Apparent activation energy
d	Bond distance at the transition state

SUBSCRIPTS

f	Forward
b	Backward
j	Elementary-like step
i	Species
k	Species, degree of freedom
ik	Species i on species k
0	Zero coverage limit
o	Standard state (T = 298 K)
ads	Adsorbed, adsorption
A	isolated adsorbates in vacuum, species
B	species
Surface	clean surface
A/surface	isolated adsorbate + clean surface
eff	Effective
vib	Vibrational
trans	Translational
rr	Rigid rotor
3D	Three-dimensional
T	Temperature
p	Pressure
y	Mole fraction
app	Apparent
TS	Transition state
FS	Final state
Rms	Root mean square

SUPERSCRIPTS

$^\circ$	Standard condition (p = 1 atm, T = 298K)
DFT	DFT-predicted
‡	Transition state
$\theta = 0$	Zero coverage limit
θ_k	Coverage of the species k
*	Stands for the site occupied by the species
gas	Gas-phase
surf	surface
A	heteroatom
AH_x	molecular species
α	Stands for the carbon of the C-O bond
β	Stands for the carbon of the C-C bond

ACRONYMS

SRE	Steam Reforming of Ethanol
WGS	Water-Gas Shift
DFT	Density Functional Theory
fcc	Face-centered cubic
CFD	Computational Fluid Dynamics
SOFC	Solid Oxide Fuel Cells
RDS	Rate Determining Step
NASF	Natural Amorphous Silica Microfibers
SEM	Scanning Electron Microscopy
TD	Thermal Decomposition
BEP	Brønsted-Evans-Polanyi
TST	Transition State Theory
LDA	Local Density Approximation
GGA	Generalized Gradient Approximation
PW91	Perdew-Wang 1991
PBE	Perdew-Burke-Ernzerhof
RPBE	Hammer-Hansen-Nørskov Modified PBE
ML	Monolayer
PV	Pressure * Volume
2D	Two-Dimensional
3D	Three-Dimensional
BOC	Bond-Order Conservation
RPA	Reaction Path Analysis
RP	Reaction Path Fraction
PEA	Partial Equilibrium Analysis
PE	Partial Equilibrium Ratio
PCA	Principal Component Analysis
MISI	Most Important Surface Intermediates
MASI	Most Abundant Surface Intermediates
rWGS	reverse Water-Gas Shift
TDS	Thermal Desorption Spectroscopy
FTIR	Fourier Transform Infrared Spectroscopy
XANES	X-Ray Absorption Near Edge Structure
DRIFTS	Diffuse Reflectance Infrared Fourier Transform Spectroscopy
HREELS	High Resolution Electron Energy Loss Spectroscopy
IRAS	Infrared Reflection Absorption Spectroscopy
DZP	Double Zeta Plus Polarization

BSSE	Basis Set Superposition Error
UBI-QEP	Unity Bond Index-Quadratic Exponential Potential
TPD	Temperature Programmed Desorption
RAIR	Reflection Absorption Infrared Spectroscopy

SUMMARY

CHAPTER 1. INTRODUCTION

1.1. BACKGROUND

The development of technologies based on renewable energy sources has received great attention around the world due to the current drive to decrease the emission of greenhouse gases and to attain energy security. Brazil has a peculiar position in the world scenario due to its large-scale use of ethanol as an automotive fuel, displacing gasoline, making use of a well established structure for production, storage and transportation. All this structure allows the development of new technologies for the use of ethanol in others sectors of the economy. Some innovative, but not yet commercially available alternative to use ethanol include the local generation of electricity by using an internal high temperature reformer coupled with Solid Oxide Fuel Cells (SOFC) or the generation of a H_2-rich syngas to be used in industries as a source of chemicals or gaseous fuel in heating processes. For both alternatives, the most feasible route nowadays is to promote the syngas production at a catalytic reactor prior to feeding it to the process itself. This calls for highly efficient, effective and low cost reformers and catalysts.

In the steam reforming of ethanol reaction (SRE) (R1), one mol of ethanol reacts ideally with one mol of water generating carbon monoxide (CO) and hydrogen (H_2). CO is well known as a poison of the active sites of the reformers and fuel cells, making these devices less active. In order to decrease the CO concentration, the water-gas shift reaction (WGS) (R2) is employed. In this reaction, two mols of CO react with two mols of water, generating carbon dioxide (CO_2) and hydrogen gas (H_2). R3 represent the combined SRE and WGS reactions. The overall reaction is strongly endothermic.

$$C_2H_5OH + H_2O \rightleftharpoons 2CO + 4H_2, \qquad \Delta H_{298\,K} = 388 \text{ kJ mol}^{-1}, \qquad \text{(R1)}$$

$$2CO + 2H_2O \rightleftharpoons 2CO_2 + 2H_2 \qquad \Delta H_{298\,K} = -41 \text{ kJ mol}^{-1}, \qquad \text{(R2)}$$

$$C_2H_5OH + 3H_2O \rightleftharpoons 2CO_2 + 6H_2, \quad \Delta H_{298\,K} = 347.4 \text{ kJ mol}^{-1}. \qquad \text{(R3)}$$

In the past ten years, a great amount of experimental work has been developed to study the catalytic SRE and good reviews can

be found elsewhere (Vaidya and Rodrigues, 2006a; Ni et al., 2007). Ni *et al*. (Ni et al., 2007) reviewed several works that applied noble metal catalysts and concluded that Rh is the most active for ethanol conversion and produces the higher hydrogen selectivity. Liguras *et al.* (Liguras et al., 2003) showed that the activity for SRE follows the sequence: Rh > Pt > Pd > Ru. Although highly active, the high costs and low availability of noble metals, *e.g.*, platinum and rhodium, as a resource justify the development of alternatives technologically, economically and environmentally viable. One of them is the use of Ni-based catalysts. Ni-based catalysts have been used industrially over the past 50 years in steam reforming of natural gas (Sehested, 2006) and methanation (Goodman et al., 1980; Sehested et al., 2005). Its activity is lower than that of noble metals (Ni et al., 2007), however, promising results in terms of ethanol conversion and selectivity towards hydrogen have been reported in partial oxidation and steam reforming of ethanol over Ni-based catalysts (Sun et al., 2005; Liberatori et al., 2007; Mas, Baronetti, Amadeo and Laborde, 2008; Comas et al., 2004; Akande et al., 2006; de Lima et al., 2010). In this class of catalysts, the deactivation due to surface deposition of carbon is still a great challenge. Interestingly, the tendency of Ni for carbon deposition has been recently studied to combine the production of hydrogen and carbon nanotubes under ethanol decomposition over Ni/Al_2O_3 catalyst (Wang, Wang, Tang, Li and Bai, 2009; Mezalira et al., 2011). Seelam *et al.* (Seelam et al., 2010) synthesized a series of catalysts made from metal particle over carbon nanotubes and found that activity and selectivity towards hydrogen decrease following Co > Ni > Rh > Pt.

Although a great amount of work has been done to develop new catalytic materials, works related to the kinetics of the steam reforming of ethanol are scarce. Most part of them focused on global kinetics analysis at the macroscale and proposed reduced kinetic expressions (lumped modeling) (Mas, Bergamini, Baronetti, Amadeo and Laborde, 2008; Akpan et al., 2007; Vaidya and Rodrigues, 2006b). For example, in the work of Mas *et al.* (Mas, Bergamini, Baronetti, Amadeo and Laborde, 2008), the effect of the reactants, including co-feeding of methane, on the conversion in the steam reforming of ethanol on Ni/Al_2O_3 at 823 K to 923 K is analyzed and two models based on the Langmuir-Hinshelwood approach were proposed. The work of Akpan *et al.* (Akpan et al., 2007) applies Langmuir-Hinshwood and Eley-Rideal approaches to

describe the kinetics of ethanol on Ni-based catalyst at 673 K to 863 K. Vaidya and Rodrigues (Vaidya and Rodrigues, 2006b) studied the steam reforming of ethanol on $Ru/\gamma\text{-}Al_2O_3$ and proposed a kinetic expression assuming that the decomposition of a complex formed by the reaction of adsorbed ethanol and water is the rate determining step (RDS).

Recently, we evaluated the steam reforming, partial oxidation and thermal decomposition of ethanol over Ni supported on natural amorphous silica microfibers (NASF). The reactions of ethanol on metal surfaces generate a series of surface as well as gas-phase intermediates. The selectivity for a specific species is in general governed by the catalyst, but also a product of the reaction conditions. For example, Figure 1.1 shows the main C2 species formed by the thermal decomposition of ethanol on Ni/NASF. Acetaldehyde (CH_3CHO), as well as ethane (C_2H_6) and ethylene (C_2H_4) were detected. Besides C2 species, CO, CO_2, H_2 and CH_4 are also formed. While they help stabilizing the catalyst, H_2O and O_2 change selectivity toward important species, *e.g.*, H_2. It was visually observed that the formation of coke was higher on the thermal decomposition and decreased with the presence of H_2O or O_2 in the feed. Coke formation is related to the presence of C_2H_4, which polymerizes forming resistant carbon deposits. Clearly, the improvement of the catalyst and reaction conditions is desirable.

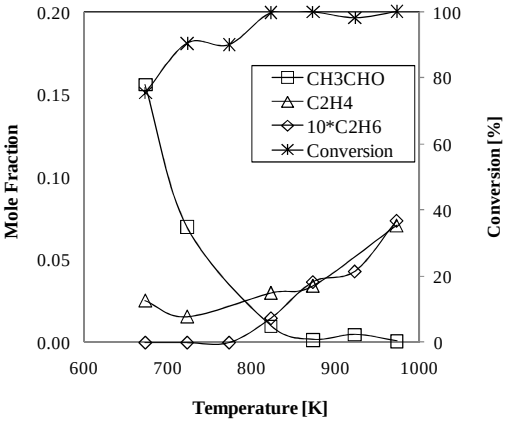

Figure 1.1. Gas-phase mole fraction of C2 species from thermal decomposition (TD) of ethanol on Ni/NASF.

Ideally, one may want to construct a catalyst using a minimum loading of the metal, with activity, selectivity towards a desired component and stability in terms of coke formation. Additionally, it is desirable to operate the reactor in a condition that favors these characteristics. Obviously, this is not an easy task simply because the catalyst and the reaction conditions are not known for the greater part of the reactions of interest. The traditional and successful approach to do this is the 'trial and error' method based on a series of *a priory* assumptions, taking advantage of the researcher's experience to build the catalyst and kinetic modeling. However, such method uses intensive experimental analysis usually time consuming and is in general focused on a specific range of reaction conditions.

1.2. THE NEED FOR A MOLECULAR LEVEL UNDERSTANDING OF CATALYTIC CHEMICAL REACTIONS

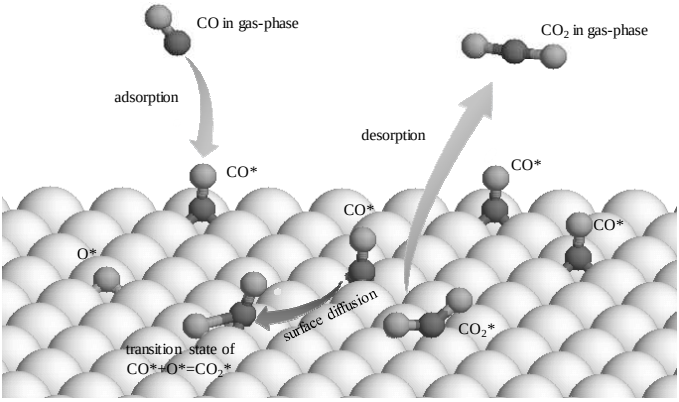

Figure 1.2. Molecular-level overview of a catalytic chemical reaction. Selected elementary-like steps of the CO oxidation reaction: CO adsorption, surface diffusion of CO*, the transition state of the CO*+O* surface reaction, the CO_2* desorption, and various adsorbed species.

Aside from predicting reaction rates, which has been carried out using reduced rate expressions, the development of new catalytic materials and converting complex feedstocks, *e.g.*, biomass, into useful chemicals and fuels demands a molecular level understanding of the reaction chemistry. At the molecular level, a

catalytic chemical reaction can be represented by several elementary-like steps including adsorption and desorption of reactants, products and intermediates, surface diffusion of adsorbates, and bond breaking/making steps that generate new reactive intermediates. As an example, elementary-like steps in the CO catalytic oxidation on an fcc metal surface are shown in Figure 1.2. Depending on the molecular weights of the reactants, the reaction network of elementary steps can be large.

Industrial catalysts are not ideal single-crystal surfaces like the one presented in Figure 1.2. Rather, they consist of multiple surfaces, edges, corners, defects and interfaces between metallic particles and supports, resulting in multiple binding sites that may favor different pathways in a reaction network. Heterogeneity in an actual catalyst, which is often responsible for its activity (Honkala et al., 2005; Beebe et al., 1987) and possibly selectivity (Vang et al., 2006), often makes it challenging to understand a reaction mechanism. The advance of computational quantum mechanics tools (VASP, n.d.; Soler et al., 2001; DACAPO, n.d.; CASTEP, n.d.) as well as the increase in computational power over the last ten years have contributed to narrowing the gap between molecular level understanding and experimental measurements. *Density Functional Theory* (DFT) has been successfully applied to calculate adsorption properties of adsorbates and reaction barriers on well-defined surfaces (Blaylock et al., 2009; Huang et al., 2010). Nevertheless, accounting for the effect of heterogeneities of catalysts on macroscopic performance is a challenge that only recently has been addressed (Salciccioli, Stamatakis, Caratzoulas and Vlachos, 2011; Stamatakis et al., 2011).

Microkinetic modeling, presented in this thesis, aims at understanding how the surface and adsorbate properties affect thermodynamic and kinetic phenomena at the meso- and macro-scales. Drawing connections between quantum mechanical calculations and macroscopic measurements is difficult due to the vast differences in characteristic length and time scales (Raimondeau and Vlachos, 2002). Quantum mechanics calculations target systems of 10-100 atoms to obtain parameters for estimating rate constants, whereas systems of industrial interest span much larger scales. Developing a microkinetic model of a surface-catalyzed reaction and incorporating its results in a reactor model provides a consistent, systematic way of bridging the gap between

scales as well as getting insights into more stable catalysts. The detailed surface reaction mechanism resulting from the microkinetic modeling is a powerful tool to be used in reactor design, *e.g.*, using CFD codes such as CHEMKIN.

1.3. OVERVIEW OF THE MODELING WORKS

The majority of theoretical works addressing reactions with ethanol on metallic surfaces at the molecular level focus on noble metal catalyst (Kapur et al., 2010; Li et al., 2010; Wang et al., 2010; Pallassana and Neurock, 2002), in particular Pt surfaces (Gursahani et al., 2001; Alcalá et al., 2005; Alcalá et al., 2003), bimetallic catalyst (Pallassana and Neurock, 2002; Alcalá et al., 2005; Skoplyak et al., 2008) and trends among transition metal (Pallassana and Neurock, 2002; Ferrin et al., 2009). Under steam reforming conditions, the presence of water in the feed generates OH and O over the metallic surfaces (Blaylock et al., 2009; Phatak et al., 2009). The elementary steps and the reaction pathways may be different from those of pure decomposition and few works have taken this into account (Wang et al., 2010; Gursahani et al., 2001). Nonetheless, few studies have included Ni surfaces, mostly in the analysis of trends among metals.

The C1 chemistry, *i.e.*, WGS, methane and methanol chemistries, is more studied over Ni surfaces due to the fact that Ni is vastly applied for reforming of hydrocarbons. Most studies have focused on the reforming of methane (Blaylock et al., 2009; Bengaard et al., 2002; Zhu et al., 2009), trends of the WGS reaction over transition metals (Huang et al., 2010; Jelic and Meyer, 2010; Schumacher et al., 2005), CO methanation via direct C-O bond breaking mechanism (Bengaard et al., 2002; Watwe et al., 2000) and methanol synthesis (Remediakis et al., 2004). Formate (HCOO) is not commonly accounted for in DFT or microkinetic modeling. Very few DFT studies have addressed formate on Ni surfaces, *e.g.*, formate adsorption on Ni (111), (100) and (110) (Pang et al., 2010), formate decomposition on Ni (111) and (211) surfaces (Cao et al., 2009) as well as on Ni (110) (Vesselli et al., 2008). The nature of the active sites has been discussed for WGS reaction on Pt (111) and (211) surfaces (Stamatakis et al., 2011) and for the bond breaking of diatomic molecules, *e.g.*, CO (Nørskov et al., 2002). Specifically on nickel, the activity for steam reforming and methanation reactions has been attributed to the ability of surface steps and defects to

decrease the activation energy of C-H bond breaking/forming reactions (Bengaard et al., 2002; Abild-Pedersen et al., 2005; Rostrup-Nielsen and Nørskov, 2006).

The works on microkinetic models for ethanol and its intermediates on Ni are scarse. Blaylock *et al.* (Blaylock et al., 2009) presented a microkinetic model of the steam reforming of methane on Ni (111) surface, not adapted to represent experimental conditions. Aparicio (Aparicio, 1997) developed a microkinetic model of the steam reforming of methane based on kinetic parameters composed of a series of calorimetric and DFT studies from the literature. Grabow *et al.* (Grabow et al., 2008) presented a combined DFT study with microkinetic model of the WGS reaction on Pt. Maestri *et al.* (Maestri et al., 2008) showed a detailed modeling of the CH_4 combustion on Rh-based catalyst. To the best of our knowledge, the steam reforming of ethanol on Ni catalyst has not been studied using a combination of DFT and microkinetic modeling as the present thesis aims.

1.4. OBJECTIVE AND SCOPE OF THE RESEARCH

The overall aim of this research is to gain fundamental understanding of the catalytic steam reforming of ethanol over Ni catalysts. The focus is on the development of a surface reaction mechanism for predicting reaction rates at the macroscopic scale as well as on the improvement of the molecular level understanding of this reaction. The following specific tasks were undertaken to reach the overall objective.

1. Perform a review of current techniques used to develop mean field microkinetic models.
2. Develop a microkinetic model to predict rates and global kinetics of the WGS reaction on Ni. The specific tasks included:
    a. Perform a systematic DFT study of the energetics of the WGS reactions on Ni (111) and Ni (211) surfaces in order to identify the main pathways for the surface reaction and the role of these surfaces on the activity and coke formation;
    b. Develop a comprehensive treatment for thermodynamic consistency of the energetics predicted by DFT;

   c. Develop a surface reaction mechanism in order to represent experimental data reported in the literature;
   d. Perform an analysis of the main pathway and rate determining step of this reaction.
3. Develop a microkinetic model to predict rates of the SRE on Ni catalyst. The specific tasks included:
   e. Calculate via DFT the heat of adsorption of all ethanol intermediates and the activations energy of a selected group of reactions. Based on that, propose BEP correlations to calculate the activation energies of the remaining steps.
   f. Generate a thermodynamic consistent database of thermodynamic properties comprising all ethanol intermediates and to structure the surface reaction mechanism following the method proposed for the WGS mechanism;
   g. Perform the adjustment of the sensitive kinetic parameters within accepted errors to represent experimental data reported in the literature;
   h. Perform an analysis of the main pathways of the SRE and compare the results with findings reported in the literature.

1.5. OVERVIEW OF THE PRESENT THESIS

In the next chapter, the supporting techniques for the microkinetic modeling are organized in a compendium. Chapter 3 brings the DFT study of the WGS reaction on Ni (111) and (211) surfaces. Chapter 4 brings the microkinetic modeling of the WGS reaction on Ni, built over the energetics predicted in the Chapter 3. Chapter 5 brings the DFT calculations ethanol intermediates and surface reactions on Ni (111) surface. Finally, Chapter 6 brings the microkinetic modeling of the steam reforming of ethanol on Ni catalyst. In order to make the relative large scope of the present thesis more comprehensive, each chapter has been written as an individual work. Specific conclusions are then presented at the end of each chapter. In the last chapter, a series of concluding remarks and suggestions for future work are summarized.

CHAPTER 2. CATALYTIC KINETICS AND DYNAMICS

This chapter aims at introducing all the concepts and techniques used in the following chapters. Figure 2.1 summarizes the methods discussed here and their hierarquical relations. The techniques presented here focus on mean-field microkinetic models, in which the adsorbates are homogeneously distributed over the catalytic surface at each location of a chemical reactor, *i.e.*, the distribution of adsorbates at each reactor location is assumed to be uniform but possibly varying with location. This makes averaging over microscopic configurations to compute the (mesoscale) reaction rate rather trivial. As a result, the well-known mass action kinetics for estimation of the reaction rate from the rate constants and local concentrations of adsorbates can be employed.

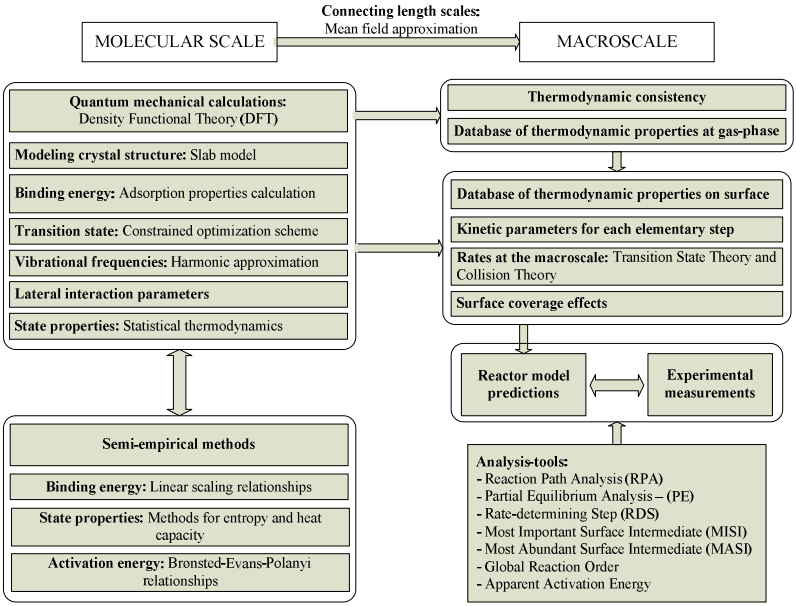

Figure 2.1. Overview of microkinetic modeling and supporting techniques.

The organization of this chapter is as follows. First, methods for calculating the rate constant of an elementary step is described.

Then DFT is briefly introduced for estimation of adsorption properties and barriers, followed by an outline of selected statistical thermodynamics. Examples of the thermochemistry on Ni(111) and Pt(111) are presented to address thermodynamic consistency of the DFT-predicted adsorption properties. Semi-empirical methods for predicting adsorbate thermodynamic properties and kinetic parameters are also presented. With this input, microkinetic models can be solved. Finally, analytical tools are described to develop and analyze a microkinetic model, with the water-gas shift reaction on Pt-based catalysts taken as an example.

This entire chapter was submitted for publication as a chapter in the book "Heterogeneous Catalysis at the Nanoscale for Energy Applications" (Catapan et al., to be published) and contains part of the work of M. Christiansen, co-author of the book chapter, on WGS reaction on Pt catalyst. Such data were kept here for clarity of the text. The data on Ni (111) surface was calculated in the context of the present thesis.

2.1. BASICS OF CATALYST FUNCTIONALITY, MECHANISMS, AND ELEMENTARY REACTIONS ON SURFACES

The role of a catalyst can be described using simple concepts: the surface stabilizes reactive intermediates, increases the likelihood of reaction due to proximity, *i.e.*, by bringing reactive intermediates close to each other (especially when surface diffusion is fast), and lowers the barrier of a reaction thereby increasing the reaction rate constant. In addition, the modification of the potential energy surface, compared to the gas-phase, often results in processes that are intrinsically more selective. A consequence of the aforementioned concepts is the Sabatier principle, which states that there is an optimum interaction between the adsorbate and the surface to maximize the reaction rate. If the interaction is too weak, the coverage of the adsorbate is low due to fast desorption and the reaction rate is low. On the other hand, if the interaction is too strong, the catalyst sites are blocked by adsorbates and the reaction rate is also low.

Elementary steps describe fundamental bond-breaking and bond-forming reactions. An overall reaction is made up of multiple elementary steps. As an example, consider the stoichiometric, global water-gas shift (WGS) reaction,

$$CO + H_2O \rightleftharpoons CO_2 + H_2 \,. \qquad (2.1)$$

Table 2.1. Summary of elementary steps and associated parameters of the WGS reaction on Pt (111) (see the footnotes for the nomenclature of the chemical species). Data from M. Christiansen in (Catapan et al., to be published).

	Elementary Step	$A_{f,j}$ [s^{-1}] or S_0	$E_{a,f,j}$ [kJ/mol]	ΔH_j° [kJ/mol]	ΔS_j° [J/mol K]
R1	$H_2O+*\rightleftharpoons H_2O*$	0.50	0.0	-34.7	-145.6
R2	$CO+*\rightleftharpoons CO*$	0.80	0.0	-156.1	-151.5
R3	$H_2+2*\rightleftharpoons 2H*$	0.10	0.0	-78.2	-119.2
R4	$CO_2+*\rightleftharpoons CO_2*$	0.50	0.0	-2.9	-55.2
R5	$OH*+H*\rightleftharpoons H_2O*+*$	$9.15\cdot10^{12}$	27.2	-41.4	-1.7
R6	$OH*+*\rightleftharpoons O*+H*$	$3.88\cdot10^{12}$	111.3	26.8	-15.9
R7	$2OH*\rightleftharpoons H_2O*+O*$	$3.56\cdot10^{12}$	27.6	-14.6	-17.2
R8	$CO_2*+*\rightleftharpoons CO*+O*$	$3.35\cdot10^{10}$	96.2	0.0	-95.0
R9	$CO*+OH*\rightleftharpoons COOH*+*$	$1.65\cdot10^{13}$	74.9	37.7	8.4
R10	$CO_2*+H*\rightleftharpoons COOH*+*$	$1.42\cdot10^{11}$	76.6	10.9	-70.7
R11	$CO_2*+OH*\rightleftharpoons COOH*+O*$	$5.52\cdot10^{10}$	46.0	37.7	-86.6
R12	$COOH*+OH*\rightleftharpoons CO_2*+H_2O*$	$6.44\cdot10^{14}$	9.6	-51.9	69.5
R13	$HCO*+O*\rightleftharpoons HCOO**$	$1.55\cdot10^{13}$	121.3	-18.4	7.1
R14	$HCOO**\rightleftharpoons CO_2*+H*$	$5.82\cdot10^{14}$	72.4	-72.4	67.8
R15	$HCOO**+O*\rightleftharpoons CO_2*+OH*+*$	$1.50\cdot10^{15}$	119.2	-99.2	83.3
R16	$HCOO**+OH*\rightleftharpoons CO_2*+H_2O*+*$	$5.33\cdot10^{14}$	76.1	-113.8	66.1
R17	$HCO*+*\rightleftharpoons CO*+H*$	$3.01\cdot10^{12}$	34.7	-91.2	-20.1

Notes: Here, the symbol * denotes an active site and it is used after a chemical species to denote an adsorbed species, e.g., the reaction $H_2O+*\rightleftharpoons H_2O*$ stands for a gas-phase species (H_2O) plus an active site (*) resulting in an adsorbed species (H_2O*). The advantage of this nomenclature is that a species that occupies two active sites on the surface may be represented followed by two asterisks, *e.g.*, HCOO**. The forward reaction rate constant is governed by the modified Arrhenius Eq. (2.16). Reaction rate constant of the surface reactions and adsorption reactions are governed by Eq. (2.3) and (2.7), respectively. The pre-exponential factors ($A_{f,j}$) were obtained using an order of magnitude value of k_BT/h and adjusted for thermodynamic consistency using Eq. (2.16) assuming $\Delta S_j^{\circ DFT} = 0$. Activation energies were for thermodynamic consistency using Eq. (2.17), assuming $\omega_j = 0$ for R12 and $\omega_j = 0.5$ for the remaining reactions. DFT method: SIESTA, GGA-PBE, 2x2 unit cell, four-layer slab, 5x5x1 k-points in the Monkhorst-Pack grid and energy cutoff of 200 Ry. Gas-phase thermochemical data were obtained from the GRI mechanism (Frenklach et al., n.d.). Pre-exponential of R5, R9 and R17 were adjusted within error to fit experimental data (factor 10 or less).

An overall reaction shows only reactants and products, and therefore, depicts only the *overall stoichiometry*. On the other hand, elementary steps describe how reactants transform to products by single bond breaking/making steps, including adsorption and desorption of reactants and products.

Table 2.1 lists the elementary steps considered in the WGS reaction. The mechanism consists of 17 elementary, reversible steps, involving 4 gas-phase species and 9 adsorbates. The main steps involve adsorption and desorption of reactants and products (R1 to R4), water and OH activation (R5 to R7), CO oxidation (R8 and R9), and carboxyl (R10 to R12), formate (R13 to R16) and formyl (R17) chemistry. Adsorption/desorption steps of intermediates (*i.e.*, H, O, OH, COOH, HCOO, HCO) have been omitted since they are usually only important at high temperatures when gas-phase chemistry occurs (Maestri et al., 2008). The decision of which intermediates and reactions must be included in a detailed surface reaction mechanism is based on the modeler's experience and experimental evidence when available. A general guidance is that the mechanism must be comprehensive and grow upon the submechanisms of smaller species in a hierarchical way (Mhadeshwar and Vlachos, 2004). Although the discussion on reaction mechanism generation is beyond the scope of this chapter, sensitivity and reaction path analyses, presented later, can assist with assessing the completeness of a reaction mechanism.

Microkinetic modeling predicts thermodynamic properties for species and kinetic parameters of elementary steps of a mechanism, as described in subsequent sections. The kinetic parameters, *i.e.*, sticking coefficient (S_0) of a species, pre-exponential factor ($A_{f,j}$) and activation energy ($E_{a,f,j}$), as well as the change in enthalpy (ΔH_j°) and entropy (ΔS_j°) in each elementary step at 298 K on Pt (111) are also presented in Table 2.1. Here, j stands for reaction index and f for forward. This mechanism will be used throughout this chapter to illustrate the capabilities of microkinetic modeling tools.

2.2. TRANSITION STATE THEORY, COLLISION THEORY AND RATE CONSTANTS

Transition State Theory (TST) connects thermodynamic properties of adsorbates and of the transition state (TS) with the

rate constant. Two main assumptions are made in TST. The first is that the time scale to either break or form a bond is longer than the time needed for energy redistribution among internal energy levels of a state along the reaction coordinate. This means that states, either initial or final, can be described using thermodynamics. The second assumption is that the molecules at the transition state are in quasi-equilibrium with the reactants. Under these assumptions, the reaction rate constant is described by the *Eyring-Polanyi* equation (Jensen, 2007)

$$k = \frac{k_B T}{h} \exp(-\Delta G^{\ddagger}/RT)\,, \tag{2.2}$$

where k_B is the Boltzmann's constant, T is the temperature, h is the Planck's constant, R is the ideal gas constant, and $\Delta G^{\ddagger} = G^{\ddagger} - \sum_i G_i$, where $G^{\ddagger}$ is the Gibbs energy at the transition state and G_i is the Gibbs energy of reactant i (‡ denotes transition state).

The rate constant of a surface reaction is often expressed using the modified Arrhenius' law

$$k_{f,j} = \frac{A_{f,j}}{\Gamma^{n-1}} \left(\frac{T}{T_o}\right)^{\beta_j} \exp\left(\frac{-E_{a,f,j}}{RT}\right). \tag{2.3}$$

Here, T_o is a reference temperature, generally 298 K, β_j is a temperature exponent, Γ is the concentration of binding sites (*e.g.*, 2.491 x 10^{-5} mol/m^2, assuming four binding sites per 2 x 2 unit cell in a Pt(111) surface), and n is the number of reactants that are surface species (including vacancies). Comparing Eqs. (2.2) and (2.3) and recognizing that the factor involving Γ is needed to account for the units of the surface concentrations, one can easily map the Arrhenius's parameters to those of TST

$$A_{f,j} \left(\frac{T}{T_o}\right)^{\beta_j} = \frac{k_B T}{h} \exp\left[\frac{(S^{\ddagger} - \sum_i S_i)}{R}\right] \text{ and} \tag{2.4}$$

$$E_{a,f,j} = H^{\ddagger} - \sum_i H_i\,. \tag{2.5}$$

Adsorption reactions link the gas phase with the catalyst surface, and its physics is described via collision theory. A general approach describing the adsorption process can be found elsewhere (Coltrin et al., 1991). The rate of adsorption is calculated from the flux of molecules (Z_w) that impinge on a surface multiplied by a probability of a molecule to bind to the surface. This probability, the

so called sticking coefficient (S), is a property of the adsorbate/surface pair. The sticking coefficient at zero coverage is denoted as S_0. The net flux of molecules (in molecules/m^2/s) impinging on a surface is calculated using the *Hertz-Knudsen* equation (Kolasinski, 2008)

$$Z_w = \frac{N_A P_k}{\sqrt{2\pi W_k RT}}. \quad (2.6)$$

In this expression, N_A is Avogadro's number, P_k is the partial pressure and W_k is the molecular weight of the k^{th} species. Assuming an ideal gas, the rate constant of (activated) adsorption at zero coverage is expressed by

$$k_{f,j} = \frac{S_0}{\Gamma^n}\sqrt{\frac{RT}{2\pi W_k}}\exp\left(\frac{-E_{a,f,j}}{RT}\right). \quad (2.7)$$

In order to describe the rate of the backward reactions, the principle of microscopic reversibility is employed. This permits the computation of the rate constant in the backward direction using the forward rate constant and the equilibrium constant

$$K_{c,j} = \frac{k_{f,j}}{k_{b,j}}\frac{1}{\Gamma^{\left(\sum_k \nu_{k,j,surface}\right)}}. \quad (2.8)$$

Here $K_{c,j}$ is the equilibrium constant in concentration units and $\sum_k \nu_{k,j,surface}$ is the sum of stoichiometric coefficients of surface-phase reactant species (including vacancies) in reaction j. $K_{c,j}$ can be obtained from the thermodynamic equilibrium constant $K_{p,j}$. The equilibrium constant is calculated for each elementary step at a given temperature T by taking into account the thermodynamic properties of reactions through

$$K_{p,j} = \exp\left(\frac{\Delta S_j}{R} - \frac{\Delta H_j}{RT}\right), \quad (2.9)$$

where ΔS_j and ΔH_j are the entropy and enthalpy change of the surface reaction.

2.3. DENSITY FUNCTIONAL THEORY (DFT) CALCULATIONS

The development of DFT is based on Kohn and Hohenberg's mathematical theorem, which states that the ground state of the electronic energy can be calculated as a functional of the electron

density (Hohenberg and Kohn, 1964). The task of finding the electron density was solved by Kohn and Sham (Kohn and Sham, 1965). They derived a set of equations in which each equation is related to a single electron wave function. From the single electron wave functions one can calculate the electron density. Usually in DFT computer codes, the electron density of the core electrons, *i.e.*, those electrons that are not important for chemical bonds, are often represented by a pseudopotential that reproduces important physical features, so that the Kohn-Sham equations span only a limited number of electrons. For each type of pseudopotential, a cutoff energy must be specified.

The challenge of DFT modeling is to design an exchange-correlation energy functional that correlates energy with the electron density. Failure to accurately account for Columbic interactions between electrons and other quantum mechanical effects can result in poor prediction of the total energy. Several forms of the exchange-correlation functional have been proposed that achieve good results in a number of physical problems. A good review can be found elsewhere (Jensen, 2007). The simplest type of exchange-correlation functional is the so-called *local density approximation* (LDA). LDA assumes that the electron density behaves like the electron-gas density, which is constant, and therefore no higher orders terms are included. The exchange-correlation functionals used for most calculations of adsorption employ the *generalized gradient approximation* (GGA), which includes the first derivative of the electron density. In this family, PW91 (Perdew, 1991) (*Perdew-Wang 1991*), PBE (Perdew et al., 1996) (*Perdew-Burke-Ernzerhof*) and RPBE (Hammer et al., 1999) (*Hammer-Hansen-Nørskov modified PBE*) functionals are the most popular. Hammer et al. (Hammer et al., 1999) compared the ability of various functionals to predict adsorption properties of simple adsorbates on well-defined surfaces using periodic slabs. In general, GGA functionals are better than LDA functionals at predicting adsorption properties due to the presence of a higher order scheme. Although PW91 has the worst performance among GGAs, it predicts better the lattice constant, and therefore, it is used in surface reconstruction problems (Zhai et al., 2010; Kitchin et al., 2005). RPBE exhibits better performance when compared to PBE. PBE uses parameters that are non-empirical and results in a good tradeoff

between accuracy and the computational cost inherent to higher-order functionals.

A periodic slab calculation takes advantage of the symmetry of a surface. A supercell is set with atoms in a certain number of layers and vacuum space in the third dimension. The surface adjacent to the vacuum represents the active surface. DFT codes are generally written using periodic boundary conditions in three dimensions. Figure 2.2 presents a rendering of (111) and (211) surfaces of an fcc metal and their respective supercells. To calculate the energy of a surface with, for example, four atomic layers, the bottom two layers of the slab are *frozen* in their initial position to mimic the bulk phase and the top layers and adsorbates are allowed to relax. The initial positions are defined from the crystal structure using the corresponding computationally-determined lattice constant.

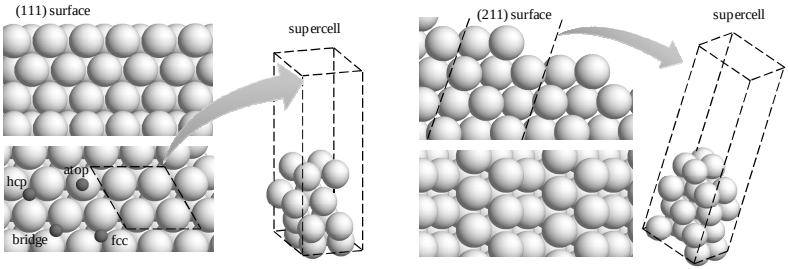

Figure 2.2. Rendering of (111) and (211) surfaces of an fcc metal. The binding sites on (111) surface are shown. The surpercells used in DFT calculations are also presented.

DFT packages that apply periodic boundary conditions use either the plane wave method, *e.g.*, VASP (VASP, n.d.; Kresse and Furthmüller, 1996), DACAPO (DACAPO, n.d.) and CASTEP (CASTEP, n.d.) or a linear combination of atomic orbitals, *e.g.*, SIESTA (Soler et al., 2001).

There are multiple methods for transition state searches (Sholl and Steckel, 2009). As an example, the one implemented in the SIESTA code is the constrained optimization scheme (Alavi et al., 1998; Zhang et al., 1999). Initially, the distance between atoms participating in the bond that forms or breaks is constrained at an estimated value, and the total energy of the system is minimized

with respect to all the other degrees of freedom. Then, this procedure is repeated with a new distance until the transition state is found so that all forces on atoms vanish and the total energy is a maximum along the reaction coordinate but a minimum with respect to the remaining degrees of freedom.

2.3.1. Calculation of Energetics and Coverage Effects

Binding energies are calculated as

$$E_{ads} = E_{A/surface} - E_A - E_{surface}\,, \tag{2.10}$$

where E_A and $E_{surface}$ are the total energies of the isolated adsorbates in vacuum and the clean surface, respectively. $E_{A/surface}$ is the lowest energy among the different sites tested. In Figure 2.2, the different binding sites, typically investigated on the (111) surface, are also shown. For transition state calculations, $E_{A/surface}$ is the energy at the transition state and E_A is the summation of the total energies of the reactants in vacuum. Therefore, E_{ads} becomes the energy at the transition state in relation to the gas-phase reactants. The activation energy is then calculated as the difference between the transition and initial state energies. The initial state energy is generally taken as the summation of the binding energies of reactants on separate slabs.

The binding energy of an adsorbate depends on the coverage of adsorbates on the surface. For example, the heat of adsorption of CO on Ni (111) decreases by ~125 kJ/mol due to lateral interactions as the CO coverage increases from zero to 0.5 monolayer (ML) (Stuckless et al., 1993). Hydrogen bonding can also occur for certain species, such as water (Hodgson and Haq, 2009; Meng et al., 2004), increasing the binding energy of such species. Lateral interactions also affect the activation barrier of a reaction by stabilizing or destabilizing the transition state with respect to the initial or final state (Hammer, 2001; Mhadeshwar et al., 2004). As an example, Hammer (Hammer, 2001) showed using DFT calculations that the barrier for dissociation of N_2 on Ru (0001) strongly increases with increasing coverage of N*, O* and H*. This behavior was attributed to the repulsive interactions between the reaction complex and the adsorbates.

The binding energy is calculated at a certain coverage of adsorbates depending on the unit cell size. This coverage is 1/4 ML

when a monodentate adsorbate is placed on a 2x2 unit cell, 1/9 ML on a 3x3, and so on. In order to obtain the heat of adsorption in the zero-coverage limit, the unit cell must be sufficiently large so that the effect of lateral interactions is small. Alternatively, one can perform a number of DFT calculations at various coverages, as explained next, and extrapolate the heat of adsorption to the zero coverage limit. To account for the effect of coverage, the heat of adsorption and activation energy are computed as follows:

$$\Delta H_{ads,i}(\theta) = \Delta H_{ads,i}^{\theta=0} + \sum_{k=1}^{n} \alpha_{ik}\theta_k \text{ and} \quad (2.11)$$

$$E_{a,f,j}(\theta) = E_{a,f,j}^{\theta=0} + \sum_{k=1}^{n} \varepsilon_{jk}\theta_k\,, \quad (2.12)$$

where α_{ik} is the lateral interaction parameter of species k on species i and ε_{jk} is the lateral interaction of species k on the barrier of reaction j. θ_k is the coverage of species k and n is the number of species. The superscript $\theta = 0$ stands for adsorption properties in the zero coverage limit. The above models assume a linear dependence on coverage (Inoglu and Kitchin, 2010). While this is a reasonable approximation for the heat of adsorption, there is limited data to support such as model for reaction barriers.

In order to calculate the lateral interaction parameters, DFT calculations are performed on species i in the presence of different coverages of species k, θ_k. Eq. (2.13) is used repeatedly, at each value of θ_k, to compute the effective adsorption energy of species i in the presence of a coverage θ_k,

$$E_{eff,i}(\theta_k) = \left(E_{i/surface}^{\theta_k} - E_i - E_{surface}^{\theta_k}\right), \quad (2.13)$$

Here $E_{i/surface}^{\theta_k}$ is the energy of species i on the surface and also species k on the same surface with a coverage θ_k, E_i is the energy of species i isolated in vacuum, and $E_{surface}^{\theta_k}$ is the energy of the surface with species k adsorbed onto it with a coverage θ_k in an identical configuration as species k in $E_{i/surface}^{\theta_k}$. Note that Eq. (2.10) and Eq. (2.13) are similar formulae for computing the adsorption energy of a surface species. The main difference is that in Eq. (2.10) the adsorbate (A) is alone on the slab, while in Eq. (2.13) the adsorbate (i) is surrounded by species k with a coverage θ_k. The various $E_{eff,i}(\theta_k)$ are then plotted as a function of θ_k. Then, assuming that the effective adsorption energies vary linearly with the coverage

(Inoglu and Kitchin, 2010), a linear regression is performed. The value of α_{ik} is ½ the value of the slope parameter of the regression. The factor of ½ is used because of an assumed pairwise interaction. Since α_{ik} is a slope parameter, it represents the change in the adsorption energy of species i with changes in θ_k. The pairwise interaction assumption implies that half of the change in energy is associated with destabilization or stabilization of species i and half with species k. The parameter ε_{ji} is calculated in a similar manner, except that species i is the transition state of interest.

A priori computation of the entire interaction matrix, even when neglecting many body effects, requires a total number of DFT calculations of the order of the square of the number of species. This approach is prohibitive for large mechanisms. Various hierarchical approaches have been suggested to avoid this large number of DFT calculations (Salciccioli, Stamatakis, Caratzoulas and Vlachos, 2011). Based on those hierarchical approaches and the methods described in this section, the interaction parameters listed in Table 2.2 were obtained and utilized in the WGS model.

Table 2.2. Coverage dependent heats of adsorptions for the adsorbates used in the model of WGS on Pt(111). Data from M. Christiansen in (Catapan et al., to be published).

Adsorbates	$\Delta H_{ads,i}$[a] + $\alpha_{i,k}$[c]θ_k [kJ/mol]
CO*	-179.9[b] + 93.7[d]θCO + 69.0[d]θH
H_2O*	-34.7
CO_2*	-2.09
OH*	-235.6
O*	-379.1
H*	-264.4 + 37.7[e]θH + 27.2θCO
COOH*	-249.8 + 25.1θCO
HCOO*	-233.5
HCO*	-256.5

[a] Zero-coverage adsorption energies obtained from DFT unless otherwise indicated. Same DFT method of Table 2.1. [b] Adsorption energy taken from experimental measurements (Yeo et al., 1997). [c] Calculated according to Eq. (2.13), and adjusted within the 95% confidence intervals of the slope parameter in order to fit to experimental data. DFT method: 3x3 unit cell used for COOH*. [d] From Ref. (Stamatakis et al., 2011). [e] From Ref. (Chen and Vlachos, 2010b).

Surface species with the highest coverages have the greatest possibility of influencing the binding energies of other surface

species. Herein, CO* is present in high coverages on Pt at low temperatures, and it has been shown that coverage effects for CO on Pt are important under WGS conditions. (Mhadeshwar and Vlachos, 2005a) H* was also present in appreciable amounts and so its coverage effects were included. Computing the normalized sensitivity coefficient (see Eq. ((2.35) showed that in addition to CO* and H*, the overall conversion is sensitive to the adsorption energy of COOH*. Additional details on how the lateral interaction parameters were obtained are available in the footnotes of Table 2.2.

2.3.2. Calculation of Vibrational Frequencies

Vibrational frequencies of the adsorbates are required to calculate thermodynamic properties using statistical thermodynamics as well as zero point energy corrections of the adsorbates. As an example, within SIESTA code (Soler et al., 2001) the vibrational frequencies are computed using the harmonic oscillator approximation based on numerical calculation of the Hessian matrix (Soler et al., 2001). First, the energy calculation for the structure, including the adsorbate, is well converged using tight convergence for the forces on atoms to minimize numerical errors. Then, the atoms of the metal are fixed in their optimized position while each atom of the adsorbate is slightly displaced independently in the three Cartesian directions. Diagonalization of the resulting Hessian matrix produces eigenvalues that represent the vibrational frequencies of the normal vibrational modes of the adsorbates.

2.4. THERMODYNAMIC CONSISTENCY OF THE DFT-PREDICTED ENERGETICS

In general, energies predicted using DFT methods differ from experimental or high level *ab initio* data. This is best illustrated when a thermodynamic loop is drawn. Consider the activation of CO on a surface ($CO^* + * \rightleftharpoons C^* + O^*$). The thermodynamic cycle for this reaction can be written as

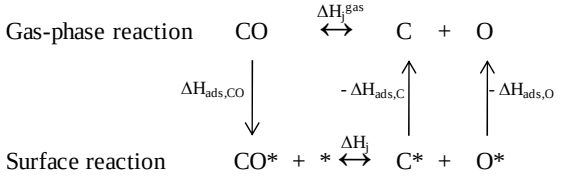

,

where ΔH_j^{gas} is the heat of reaction in the gas-phase, $\Delta H_{ads,i}$ is the heat of adsorption of species i, defined here as negative for an exothermic process, and ΔH_j is the heat of the surface reaction. In order to ensure thermodynamic consistency at the enthalpic level of a surface reaction mechanism, the heat of each surface reaction must satisfy the following constraints, based on the thermodynamic cycle and microscopic reversibility

$$\Delta H_j = \Delta H_j^{gas} + \sum_{i=1}^{k_s} \nu_{ij} \Delta H_{ads,i} \quad \text{and} \tag{2.14}$$

$$\Delta H_j = E_{a,f,j} - E_{a,b,j}, \tag{2.15}$$

where ν_{ij} is the stoichiometric coefficient of species i in reaction j, and k_s is the number of adsorbates in the thermodynamic cycle of the surface reaction. The subscripts f and b in the activation energy terms refer to the forward and backward reactions, respectively. For convenience, the coverage dependency on the energies is not shown. Assuming that ΔH_j^{gas} is taken from a thermodynamic database, for example Burcat's database (Goos et al., 2011), the difference between the DFT-predicted energies and the gas-phase thermodynamic value can be considered as the error in using DFT.

For the specific example, the heat of the CO activation reaction in gas-phase ($CO \rightleftharpoons C + O$) at 298 K evaluated by the DFT method used here, including temperature correction, is 1034.7 kJ/mol as compared to 1075.7 kJ/mol calculated from (Goos et al., 2011). This difference (of ~40 kJ/mol in this example) makes the DFT calculations inconsistent with high level *ab initio* methods used to compute thermodynamic properties in the gas-phase. Use of DFT values only, without employing literature or *ab initio* gas-phase thermodynamics, can overcome this inconsistency at the expense of having less accurate thermodynamics with implications for error in energy balances, equilibrium conversions, and gas-phase species

concentrations. Similarly to enthalpic inconsistency, entropic inconsistency may also exist.

Generally, a method must be devised to satisfy Eq. (2.14), as well as the corresponding equation for entropic consistency. Such a method was first discussed in (Mhadeshwar et al., 2003), based on the number of linearly independent degrees of freedom one has in a microkinetic model. As a specific example for entropic consistency, consider that Table 2.1 lists pre-exponential factors that must maintain consistency with thermodynamics. This is accomplished using Eq (2.16) (Salciccioli, Stamatakis, Caratzoulas and Vlachos, 2011),

$$A_{f,j} = A_{f,j}^{DFT} \exp\left[\omega_j \left(\Delta S_j^{\circ} - \Delta S_j^{\circ DFT}\right)/R\right] \tag{2.16}$$

where ΔS_j° and $\Delta S_j^{\circ DFT}$ are the corrected and DFT-predicted entropies, respectively, and ω_j is a proximity factor that takes on a value between 0 and 1 inclusive. Values of $A_{f,j}^{DFT}$ are obtained from DFT calculations using Eq. (2.4). Alternatively, to reduce computational expense, $\Delta S_j^{\circ DFT}$ may be assumed to have a value of 0 and $A_{f,j}^{DFT}$ may be estimated using an order of magnitude estimate of $k_B T/h$.

Regarding enthalpic consistency, Grabow *et al.* (Grabow et al., 2008) have proposed a method in which the enthalpy of adsorption is kept as predicted from DFT, and the heat of surface reaction is adjusted to make the mechanism thermodynamically consistent for each thermodynamic loop. The difference between the corrected (ΔH_j) and the DFT-predicted (ΔH_j^{DFT}) heats of reaction is then distributed over the forward and backward activation energies through a proximity factor (ω_j)

$$E_{a,f,j} = E_{a,f,j}^{DFT} + \omega_j\left(\Delta H_j - \Delta H_j^{DFT}\right). \tag{2.17}$$

Besides ensuring thermodynamic consistency, this method allows for fitting a microkinetic model to experimental data by adjusting ω_j. Table 2.3 compares the activation energies and heats of reaction of select WGS reactions predicted from DFT and calculated using Eq. (2.17). As expected, this method changes considerably the DFT-predicted activation energies of reactions, especially those for which the surface thermodynamics differ

considerably from that of the corresponding gas-phase thermochemistry (*e.g.*, CO* + OH* ⇌ COOH* + *).

Blaylock *et al.* (Blaylock et al., 2009) have proposed to correct the enthalpy of adsorption of key species based on experimental values, keeping the enthalpy of surface reactions and activation energies as predicted from DFT calculations. This approach is closer to that proposed by Mhadeshwar and Vlachos (Mhadeshwar et al., 2003). They argue that accurate adsorption energies are harder to predict (due to the gas-phase reference being based on *ab initio* methods) than reaction energies since the latter calculations take advantage of cancelation of errors when bonds are formed and broken in a reaction. Taking the example of the CO activation reaction discussed earlier, one can calculate the heat of adsorption of C* using as inputs the heats of adsorption of CO* and O*, the heat of surface reaction predicted from DFT and the heat of reaction in gas-phase from (Goos et al., 2011). The heats of adsorption of the remaining species are calculated using Eq. (2.14) applied to all other reactions in the mechanism.

Table 2.3. Comparison between the activation energies and heats of reaction of selected WGS reactions on Ni(111) and Pt(111) predicted using DFT and corrected using Eq. (2.17). Data on Pt are from M. Christiansen in (Catapan et al., to be published).

Reactions	DFT-predicted [a]		Corrected [b]	
	$Ea_{f,j}^{DFT}$ [kJ/mol]	ΔH_j^{DFT} [kJ/mol]	$Ea_{f,j}$ [kJ/mol]	ΔH_j [kJ/mol]
	Ni (111)			
$H_2O^* + * \rightleftharpoons OH^* + H^*$	87.4	-18.0	75.3	-42.3
$OH^* + * \rightleftharpoons O^* + H^*$	93.3	-17.2	111.3	18.8
$CO^* + O^* \rightleftharpoons CO_2^* + *$	146.0	91.2	161.9	123.0
$CO^* + OH^* \rightleftharpoons COOH^* + *$	112.5	65.7	163.6	163.6
	Pt (111)			
$H_2O^* + * \rightleftharpoons OH^* + H^*$	75.3	54.8	68.2	41.4
$OH^* + * \rightleftharpoons O^* + H^*$	90.8	-14.6	111.3	26.8
$CO^* + O^* \rightleftharpoons CO_2^* + *$	103.3	13.4	96.7	0.0
$CO^* + OH^* \rightleftharpoons COOH^* + *$	44.4	-23.0	74.9	37.7

[a] Same DFT method as in Table 2.1. [b] Here, we assume $\omega_j = 0.5$.

Table 2.4 presents the thermodynamically consistent heats of adsorption of the water-gas shift adsorbates on Ni. The most significant difference between the experimentally corrected and the

DFT data is in the CO* adsorption, which is 71 kJ/mol. This is thought to be mostly due to the inability of the PBE functional to predict correctly the CO heat of adsorption (Hammer et al., 1999). The large differences indicate that matching surface and gas-phase thermochemistries is an important aspect of a model that needs careful consideration.

It was mentioned previously that the enthalpy of adsorption is coverage- and temperature-dependent. Thus, the enthalpy of reaction is also coverage and temperature dependent. One implication of this dependence is that it is not possible to preserve the DFT-predicted forward and backward activation energies while still satisfying Eq. (2.15). In a recent publication (Salciccioli, Chen and Vlachos, 2011), the approach introduced by Grabow *et al.* (Grabow et al., 2008) was extended to distribute the coverage and temperature effects of the heat of reaction on the activation energies. In this extended approach, the term in parentheses in Eq. (2.17) represents the difference between the zero-coverage heat of reaction and the heat of reaction at any coverage and temperature.

Table 2.4. Thermodynamically consistent heat of adsorption of the WGS-adsorbates on Ni(111) corrected with the method of Blaylock *et al.* (Blaylock et al., 2009). For comparison, DFT-predicted heats of adsorption are also shown.

Adsorbates	$\Delta H_{ads,i}{}^{a} + \alpha_{i,CO}{}^{b}\theta_{CO}$ [kJ/mol]	$\Delta H_{ads,i}^{DFT}{}^{c}$ [kJ/mol]
C*	-682.0	-636.0
CO*	-129.7[d] + 71.1θCO	-200.8
CO_2*	-12.6	-8.4
COOH*	-242.7+ 133.0θCO	-242.7
H*	-267.8	-267.8
H_2O*	-50.2[d] - 25.1θCO	-41.8
HCOO*	-313.8	-284.5
O*	-468.6[d] + 71.1θCO	-464.4
OH*	-284.5 + 66.9θCO	-318.0

[a] The values are valid at 298 K. The correction includes the zero point energy correction. [b] Lateral interaction parameters calculated according to Eq. (2.13). [c] Same DFT method as presented in Table 2.1. [d] Experimental heat of adsorption for species CO*, H2O* and O* were used as inputs. (Stuckless et al., 1993; Schulze et al., 1995; Stuckless et al., 1997)

Building on the method of experimentally correcting the heat of adsorption (Blaylock et al., 2009; Mhadeshwar et al., 2003), a new approach is proposed to ensure thermodynamic consistency for the activation energies in all surface reactions (Catapan et al., 2011). First, all reactions are written in the exothermic direction, keeping the forward activation energies as predicted using Eq. (2.12), and accounting for the coverage dependent activation energy predicted from DFT. The backward activation energy is then calculated to ensure thermodynamic consistency using Eq. (2.15), taking into account temperature and coverage effects. The most sensitive reactions are identified using sensitivity and partial equilibrium analyses as discussed later. Then, all sensitive reactions must be rewritten in such a way that the forward reaction rate controls the net reaction rate, keeping the important activation energies as predicted by DFT. This new approach makes the surface reaction mechanism thermodynamically consistent while adjusting important reactions to predict experimental measurements, without losing the accuracy of the DFT method in predicting activation energies.

2.5. STATE PROPERTIES FROM STATISTICAL THERMODYNAMICS

Here, two approaches to calculate state properties are presented. First, a fundamental formulation based on statistical thermodynamics is introduced. In the next section, a non-computationally demanding, semi-empirical-estimation-based approach is presented.

The coverage-dependent enthalpy of formation of the adsorbates, including the zero point energy correction, is defined as

$$H_i(T,\theta) = H_i^{gas}(T_0) + \Delta H_{ads,i} + \Delta ZPE_i + \int_{T_0}^{T} C_p dT + \sum_{k=1}^{n_k} \alpha_{ik}\theta_k \,. \quad (2.18)$$

In Eq. (2.18), $H_i^{gas}(T_0)$ is the enthalpy of formation in gas-phase at T_0 that is obtained from standard thermodynamic databases. The value of $\Delta H_{ads,i}$ depends on the method used for thermodynamic consistency at the enthalpic level. When Eq. (2.17) is used, the DFT-predicted heat of adsorption is assumed for $\Delta H_{ads,i}$. On the other hand, in the method of Blaylock *et al.* (Blaylock et al., 2009), thermodynamically corrected values such as those presented in

Table 2.4 are used. C_p is the heat capacity at constant pressure of a species on the surface. The zero point energy correction is given by

$$\Delta ZPE_i = \sum_k \frac{h\nu_k}{2}^{surf} - \sum_k \frac{h\nu_k}{2}^{gas}, \quad (2.19)$$

where ν_k is the vibrational frequency on the surface or in the gas-phase.

To compute the entropy and heat capacity from statistical thermodynamics, one has to consider the type of adsorption, depending on how strongly the adsorbate binds to the surface. In general, adsorbates that bind weakly to surfaces, *e.g.*, closed shell adsorbates, such as H_2O and CO_2, have a low barrier for surface diffusion, which makes them highly mobile on the surface. On the other hand, strongly bound adsorbates have a high barrier for surface diffusion and are assumed to be immobile on the surface. As a result of differences in adsorption, the statistical thermodynamics formulae for calculating state properties differ for each type of adsorption as discussed in the following sections.

2.5.1. Strongly Bound Adsorbates

For strongly bound adsorbates, all translational and rotational degrees of freedom present in gas-phase are assumed to be frustrated and converted into vibrational modes between adsorbates and the surface. Assuming that the PV contribution to the internal energy is small (see (Salciccioli, Stamatakis, Caratzoulas and Vlachos, 2011) and references therein), the state properties can be calculated from the vibrational contributions only, according to

$$S_{vib,i} = R\sum_k^N \left[\frac{\Theta_{\nu k}/T}{e^{\Theta_{\nu k}/T}-1} - \ln\left(1 - e^{-\Theta_{\nu k}/T}\right)\right] \text{ and} \quad (2.20)$$

$$C_{p,vib,i} = R\sum_k^N \left[\left(\frac{\Theta_{\nu k}}{T}\right)^2 \frac{e^{-\Theta_{\nu k}/T}}{\left(1-e^{-\Theta_{\nu k}/T}\right)^2}\right], \quad (2.21)$$

where $\Theta_{\nu k}$ stands for the characteristic vibrational temperature for each mode and is calculated as $\Theta_{\nu k} = h\nu_k/k_B$. The summation runs over all vibrational frequencies corresponding to a particular adsorbate.

2.5.2. Weakly Bound Adsorbates

For weakly bound adsorbates, vibrational analysis may produce vibrational frequencies close to zero or even negative for bonds with small barriers to translation or rotation. Such calculated vibrational frequencies can produce erroneous results in the thermodynamic properties since Eq. (2.20) diverges as the frequency approaches zero. This situation can be avoided by assuming that the three smallest vibrational frequencies in weakly bound adsorbates are due to rotational and two-dimensional (2D) translational degrees of freedom. Then the state properties for weakly bound adsorbates are

$$S_i = S_{vib,i} + S_{2D,trans} + S_{rr} \text{ and} \tag{2.22}$$

$$Cp_i = Cp_{vib,i} + Cp_{2D,trans} + Cp_{rr}\,, \tag{2.23}$$

where rr stands for rigid rotor contribution. The vibrational contributions are calculated with the summation in Eqs. (2.20) and (2.21) running over the remaining N-3 vibrational frequencies.

Assuming the partition function for 2D translation (Blaylock et al., 2009), one can easily derive the translational contributions to the state properties by applying the standard thermodynamic definitions as

$$S_{2D,trans} = R\left[\ln\left(\frac{2\pi M_{ads} k_B T}{h^2} N_{sites} A\right) + 1\right], \tag{2.24}$$

$$Cp_{2D,trans} = 2R\,, \tag{2.25}$$

where M_{ads} is the mass of one adsorbate, N_{sites} is the number of sites occupied by the adsorbates and A is the area of one site.

The rotational contribution to the state properties is in general one order of magnitude lower than the translational contributions at room temperature. A good approximation is that each rotational degree of freedom contributes to the thermodynamic properties as $S_{rr} = R/2$ and $Cp_{rr} = R$ (Jensen, 2007).

2.6. SEMI-EMPIRICAL METHODS FOR PREDICTING THERMODYNAMIC PROPERTIES AND KINETIC PARAMETERS

DFT-based microkinetic modeling is a powerful tool to provide a molecular-level understanding of chemical reactions, in particular for those involving small molecular weight molecules on single metals. However, the need for screening different metals and modeling reactions for larger molecules calls for developing semi-empirical methods that are much less computationally demanding for predicting thermodynamic properties and kinetic parameters (Salciccioli, Stamatakis, Caratzoulas and Vlachos, 2011).

Recently, semi-empirical methods based on DFT calculations have been developed for catalyst screening. These methods include linear scaling relationships (Abild-Pedersen et al., 2007; Salciccioli et al., 2010) to transfer thermochemistry from one metal to another and *Brønsted-Evans-Polanyi* (BEP) relationships (Chen and Vlachos, 2010b; Jiang et al., 2009; Jelic and Meyer, 2010; Nørskov et al., 2002; Alcalá et al., 2003). Here, these methods and also methods for estimation of the surface entropy and heat capacity are briefly discussed. Because of their screening capabilities, semi-empirical methods can be used to produce a first pass microkinetic model. This first pass model can then be refined using more detailed theory aided by analytical tools that identify key features of the model. The empirical bond-order conservation (BOC) method, which has shown good success in developing microkinetic models of small molecules, has recently been reviewed (Salciccioli, Stamatakis, Caratzoulas and Vlachos, 2011) and will not be covered here.

2.6.1. Linear Scaling Relationships

Linear scaling relationships correlate the heat of adsorption of molecules with the heat of adsorption of a descriptor, generally of the heteroatom of the molecule. Abild-Pedersen *et al.* (Abild-Pedersen et al., 2007) observed that the heat of adsorption of AH_x fragments correlates with the heat of adsorption of A on flat and stepped surfaces of transition metals (A=C, O, N). They proposed the following relationship

$$\Delta H_{ads}^{AH_x} = \gamma(x)\Delta H_{ads}^{A} + \xi, \qquad (2.26)$$

where the superscript "AH_x" stands for a molecular species and "A" for the heteroatom. $\gamma(x)$ relates to the valency of A, approximated from $\gamma(x) = (x_{max} - x)/x_{max}$, where x_{max} is the maximum number of hydrogen atoms that can bond to A. The parameter ξ must be calculated for each molecule. Recently, this method was extended to account for other species connected to the central heteroatom, instead of only hydrogen, in order to predict the binding energies of C_2 oxygenates on Pt, Ni and Pt-Ni bimetallic catalysts using group additivity methods (Salciccioli et al., 2010).

2.6.2. Heat Capacity and Surface Entropy Estimation

Assuming that the heat of adsorption is calculated using scaling relations and that a DFT vibrational analysis has not been performed, the enthalpy of formation of the adsorbates, analogous to Eq. (2.18), is defined as

$$H_i(T,\theta) = H_i^{gas}(T) + \Delta H_{ads,i} + \delta_i R(T - T_o) + \sum_{k=1}^{n_k} \alpha_{ik}\theta_k \,. \qquad (2.27)$$

The differences between Eq. (2.27) and Eq. (2.18) are that no zero point energy correction is included and the integral of the heat capacity ($\int_{T_0}^{T} C_p dT$) in Eq. (2.18) is replaced by the heat capacity in gas-phase, which is implicit in the first term ($H_i^{gas}(T)$), and the term $\delta_i R(T - T_o)$. This last term accounts for the change in the heat of adsorption with temperature. The so called temperature dependency parameter (δ_i) depends on the degrees of freedom lost and gained upon adsorption and is explained in detail elsewhere (Mhadeshwar et al., 2003; Mhadeshwar and Vlachos, 2005b).

The entropy of the adsorbates is estimated from (Santiago et al., 2000)

$$S_i(T) = F_{loc}\left[S_i^{gas}(T) - S_{3D,trans}(T_0)\right], \qquad (2.28)$$

where $S_{3D,trans}(T_0)$ is the translational contribution to the entropy at T_0 and F_{loc} is a fitting parameter that represents the fraction of the rotational and vibrational contributions to entropy that are maintained by the adsorbate. Usual values for F_{loc} vary from 0.95 (Salciccioli, Chen and Vlachos, 2011) to 0.98 (Santiago et al., 2000). The translational contribution to the entropy is calculated using standard statistical thermodynamics (Jensen, 2007).

The enthalpies and entropies of surface reactions listed in Table 2.1 were computed from state properties derived using the methods described in this section.

2.6.3. Brønsted-Evans-Polanyi Relationships

The *Brønsted-Evans-Polanyi* Relationship (BEP) is a linear relationship between the activation energy and the reaction enthalpy of an elementary reaction. In a generic way, a BEP relation can be written as

$$E_a = A + B\Delta H\,, \tag{2.29}$$

where A and B are the intercept and the slope, respectively. Single-step bond-breaking reactions on transition metals follow BEP correlations. Example chemistries include CO oxidation reactions on flat and stepped surfaces (Jiang et al., 2009) and WGS reactions on flat bimetallic surfaces (Jelic and Meyer, 2010). Nørskov *et al.* (Nørskov et al., 2002) observed the validity of BEP relationships not only for elementary steps on different metals, but also for a group of similar reactions involving CO, O_2, NO and N_2 on flat and stepped surfaces of several metals. Acalá *et al.* (Alcalá et al., 2003) observed that C-C and C-O bond breaking reactions give a BEP when the energies at the transition state are correlated to those of the final states. Figure 2.3 shows one example of a BEP correlation for ethylene and ethane chemistry (Chen and Vlachos, 2010b).

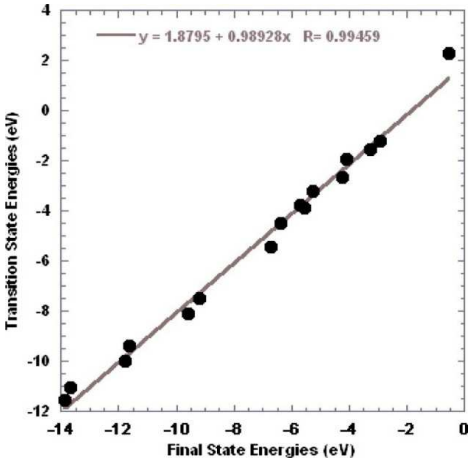

Figure 2.3. BEP correlation for ethylene and ethane chemistry (Chen and Vlachos, 2010b). The energy of the transition state of C-C bond breaking reactions correlates with the energy at the final state.

2.7. ANALYSIS TOOLS FOR MICROKINETIC MODELING

The previous sections described techniques employed for parameter estimation. These thermodynamic and kinetic parameters are input to a microkinetic model that is solved numerically. This section describes tools for the subsequent model analysis, which can be used in multiple ways. Initially during mechanism development, they can be used to assess which reactions and reactive intermediates are important in the model, which helps the modeler to focus on important features of the surface reaction mechanism. During this process, simulated macroscopic observables, *e.g.*, global reaction orders and apparent activation energies, can be compared directly to experimental data. Then, once the model describes experimental data reasonably well, analytical tools can be used to develop further insights into the reaction mechanism, with applications that include catalyst design (Hansgen et al., 2010).

2.7.1. Rates in Microkinetic Modeling

Before describing the analytical tools, basic definitions about reaction rates in microkinetic modeling are reviewed. The species net production rate through surface reactions is

$$\dot{r}_i = \sum_j \nu_{ij} \dot{q}_j \,, \tag{2.30}$$

where ν_{ij} is the stoichiometric coefficient of species i in reaction j. The summation in Eq. (2.30) runs over all reactions in the mechanism. The net rate of the j^{th} surface reaction is defined as

$$\dot{q}_j = k_{f,j} \prod_i [C_i]^{|\nu_{ij}|} - k_{b,j} \prod_i [C_i]^{|\nu_{ij}|} \,, \tag{2.31}$$

where $[C_i]$ is the concentration of species i either on the surface (including vacancies) or in gas-phase. The products in Eq. (2.31) run over all reactants of reaction j in the respective direction (either forward or backward). The units of the reaction rate constants, $k_{f,j}$ and $k_{b,j}$, depend on the type of reaction (either adsorption or surface reaction) and on the reaction order.

2.7.2. Reaction Path Analysis and Partial Equilibrium Analysis

The main objective of reaction path analysis (RPA) is to determine which reactions exhibit the highest rates in converting reactants to products, and thus obtain an overall reaction map of the reaction network. The idea is to calculate which reactions are responsible for the production or consumption of species i through

$$RP_{ij} = \frac{\dot{q}_j}{\sum_j \dot{q}_j} \,, \tag{2.32}$$

where RP_{ij} is the fraction of either net production or net consumption rate of species i by reaction j. The summation in the denominator runs over either all production or all consumption reaction rates. After computing RP_{ij} for each species, one can reduce the mechanism by eliminating reactions whose RP_{ij} for all species falls below a small threshold.

Partial equilibrium analysis investigates which reactions in the mechanism are partially equilibrated, *i.e.*, the reactions for which the forward rate is nearly equal to the backward rate. The partial equilibrium ratio is defined as

$$PE_j = \frac{\dot{q}_{j,f}}{\dot{q}_{j,f}+\dot{q}_{j,b}}, \quad (2.33)$$

where the subscripts f and b stand again for the forward and backward reaction rates, respectively. A value of PE_j of 0.5 means that the reaction is equilibrated. PE_j = 1 or 0 means that the forward or backward reaction dominates, respectively. A value of PE between 0.45 and 0.55 implies that the specific reaction is practically partially equilibrated.

Figure 2.4 depicts an example from the Pt WGS model of the output from RPA regarding the formation and consumption of a select surface species, *e.g.*, H_2O*. For display purposes, the absolute values of net rates and values of RP_{ij} for both consumption and production reactions are shown; normally consumption values are negative. The first three reactions displayed are those in which H_2O* is produced. The reaction representing adsorption of gas-phase water has the largest value of RP_{ij} for the H_2O*-producing reactions; it also has the highest net rate, which is expected because net rates are used directly to compute values of RP_{ij} according to Eq. (2.32). Since the value of RP_{ij} for water adsorption is 1, this means that at 250°C all H_2O* is produced by the adsorption of gas-phase water onto the surface. The last two reactions in Figure 5 are H_2O*-consuming reactions. For reasons similar to those discussed for H_2O production, all consumption of H_2O* takes place via water activation, generating OH* and H*. The logarithmic scale emphasizes that the two fastest reactions are orders of magnitude faster than the other reactions involving H_2O* at 250°C.

Figure 2.5 summarizes the information about the PE ratios of several reactions in the WGS mechanism. The values shown are actually "PE_i - 0.5", so that reactions in partial equilibrium would appear as "0" in the chart. Reactions far from PE exhibit bars of the largest magnitude. Displaying the PE ratios in this way facilitates the rapid identification of reactions that are furthest away from equilibrium. Combining information about PE with the net rates of reaction provides a good indication which reactions should be included in a reduced model. The most systematic way to do this is through principal component analysis (PCA) (Mhadeshwar and Vlachos, 2005a). A discussion of PCA is beyond the scope of this chapter.

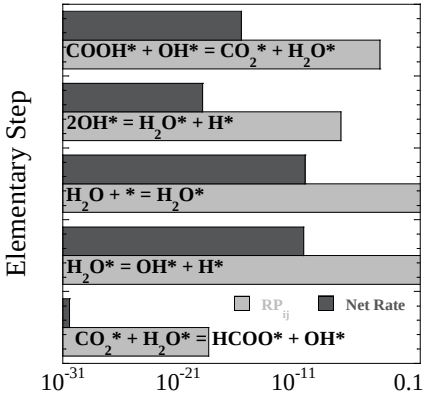

Figure 2.4. Fraction of production or consumption of a species and absolute value of net reaction rate (see text for definitions) of elementary reactions involving H_2O^* in the WGS mechanism over Pt at 250°C. The horizontal axis is in logarithmic scale; units of net rate are [moles cm^{-2} s^{-1}], and RP_{ij} is dimensionless. Data from M. Christiansen in (Catapan et al., to be published).

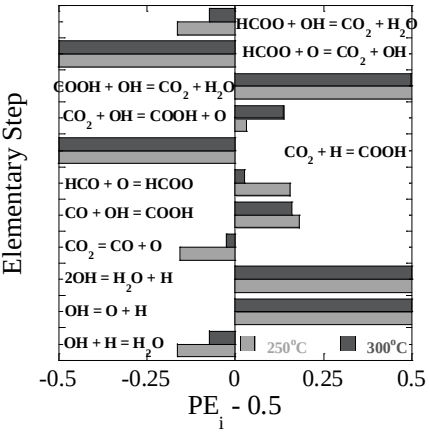

Figure 2.5. Chart of 'centered' partial equilibrium ratios for several reactions in the WGS mechanism on platinum. Only surface reactions are presented and the (*) symbols are omitted for clarity. The bars with the largest magnitudes indicate the elementary steps furthest away from partial equilibrium. Data from M. Christiansen in (Catapan et al., to be published).

RPA and PE analyses permit the creation of diagrams representing major surface reaction pathways. Figure 2.6 is an example of such a diagram for WGS on Pt. Note that adsorption-desorption reactions are in partial equilibrium (indicated by double-headed arrows), while the three surface reactions are far from partial equilibrium (indicated by single arrows).

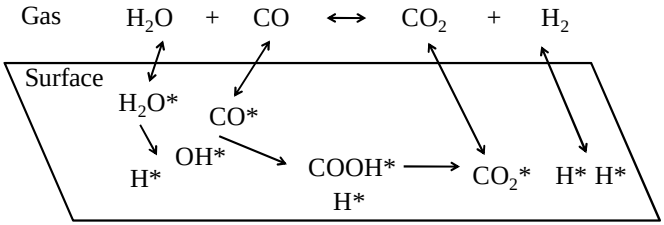

Figure 2.6. Diagram of major reaction pathways for WGS on platinum at 250°C, based on reaction path analysis (RPA) and partial equilibrium analysis (PE). Data from M. Christiansen in (Catapan et al., to be published).

2.7.3. Rate-Determining Steps (RDS), Most Important Surface Intermediates (MISI) and Most Abundant Surface Intermediates (MASI)

The concept of a rate-determining step (RDS) is common and useful in heterogeneous catalysis. It has been used as an *a priori* assumption in the development of reduced rate expressions from experimental data (Xu and Froment, 1989). Knowledge of the RDS can provide insights into how to improve a catalyst. The definition of the RDS has been discussed in the past two decades (Campbell, 1994; Dumesic, 1999). Considering the definition proposed by Campbell (Campbell, 1994), the degree of rate control by an elementary step is

$$X_{rc,j} = \frac{k_{j,f}}{\dot{r}} \left(\frac{\partial \dot{r}}{\partial k_{j,f}} \right)_{K_{p,j}, k_{k \neq j,f}}, \qquad (2.34)$$

where $\dot{r}$ is the overall reaction rate. $\dot{r}$ is usually computed for one of the reactants. When there is a single RDS in a mechanism, the degree of rate control is 1 for this step and zero for the others. Similar to the degree of rate control, the sensitivity analysis can be

performed using normalized sensitivity coefficients calculated using conversion instead of reaction rate in Eq. (2.34).

Analogous to the RDS, the important adsorbates are those which exert the most influence on the overall reaction rate. The concept of important intermediates is not commonly employed but is extremely useful to refine large mechanisms. Most important surface intermediates (MISI) are identified by the normalized sensitivity coefficient

$$\mathrm{MISI_i} = \frac{f_i}{X}\left(\frac{\partial X}{\partial f_i}\right)_{K_{p,j},f_{k\neq i}}, \qquad (2.35)$$

where f_i stands for the enthalpy or entropy of adsorbate i and X is the overall conversion. A species can be mechanistically important because it is a key in converting reactants to products; however, it may also be important simply because it is a spectator that blocks sites and affects the overall reaction rate.

Figure 2.7 displays the three reactions in the WGS model with the largest normalized sensitivity coefficients. These were computed using Eq. (2.35) , except that f_j is the pre-exponential factor of reaction j, A_{fj}. This is similar to the degree of rate control defined in Eq. (2.34) except that the overall conversion is used rather than the reaction rate. Important insights from this plot are that the sensitivity (kinetic relevance) of a reaction depends on reaction conditions, *e.g.*, temperature, and that there is not always a single rate-determining step; rather, multiple reactions can be simultaneously kinetically important.

Surface intermediates with high coverage have a higher probability to interact and change the thermochemistry of other intermediates and possibly be involved in surface reactions. By identifying the most abundant surface intermediate (MASI), model development is expedited because computational time can be allocated to account for the effects, *e.g.*, lateral adsorbate interactions, of the MASI on thermochemistry and reaction barriers. This hierarchical approach, identifying first the dominant species and then including coverage effects on thermochemistry and reaction barriers, renders first-principles modeling tractable by reducing computational cost significantly, since only part of the interaction matrix is computed. In some cases, abundant intermediates can be identified by spectroscopy in ultra-high vacuum experiments, which helps to validate models. In the case of

the WGS model on Pt, CO* is the most abundant reactive intermediate. This is in agreement with the well-known fact that high coverages of CO* are present on Pt surfaces.

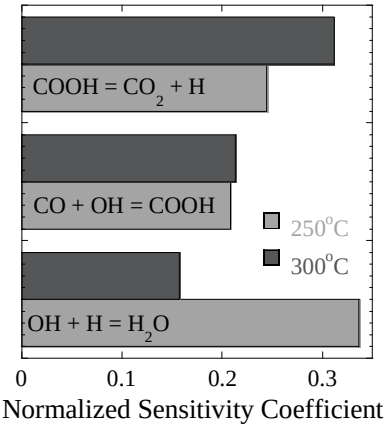

Figure 2.7. Chart of kinetically relevant steps in the WGS reaction on Pt(111), based on values of the normalized sensitivity coefficient. Data from M. Christiansen in (Catapan et al., to be published).

In closing, aside from the RDS, which is a well-established output of a microkinetic model, one can perform sensitivity analyses in other ways to determine the thermodynamic and kinetic parameters that most affect the response of interest. Examples of responses include the selectivity, the concentration of a pollutant, the maximum reactor temperature, and the location of the temperature maximum.

2.7.4. Calculation of the Overall Reaction Order and Apparent Activation Energy

Two important quantities that are often evaluated from a microkinetic model are the reaction order with respect to each reactant and the apparent activation energy. Both quantities can be estimated from experiments using flow reactors (Grenoble et al., 1981; Wei and Iglesia, 2004), which makes them valuable parameters in validating and fine tuning a model. Reaction order data are also some of the best indicators of the kinetics of the

mechanism, and agreement with experimental orders is a good indication that the model is capturing the correct kinetics.

Assuming that the overall rate constant follows Arrhenius' law, the reaction order with respect to the reactant i (α_i) and the apparent activation energy ($E_{a,app}$) are calculated from

$$\alpha_i = \left(\frac{\partial \ln(\dot{r})}{\partial \ln(y_i)}\right)_{T,p}, \tag{2.36}$$

$$E_{a,app} = RT^2 \left(\frac{\partial \ln(\dot{r})}{\partial T}\right)_{p,y_i}, \tag{2.37}$$

where y_i is the mole fraction of species i in the gas-phase.

Table 2.5 compares measured (Grabow et al., 2008) and calculated reaction orders and apparent activation energies for the WGS on Pt. The model is capable of reproducing the experimental results quite well.

Table 2.5. Comparison of reaction orders and the apparent activation energy obtained from supported catalyst experiments (Grabow et al., 2008) with corresponding values obtained from the WGS model on Pt.

Reaction Orders	Experiment	Model
H_2O	0.56 ± 0.05	0.78
CO	-0.14 ± 0.05	0
H_2	-0.33 ± 0.04	-0.40
CO_2	0.02 ± 0.09	0.01
$E_{a,app}$ [kJ/mol]	71.5	63.2

2.8. CONCLUDING REMARKS

In this chapter, an overview of microkinetic modeling was given. Microkinetic modeling aims at understanding how surface structure and adsorbate properties at the molecular level affect thermodynamic and kinetic phenomena at the macroscale. Inputs to microkinetic modeling via first principles and semi-empirical methods were discussed, followed by an explanation of several microkinetic analysis tools. The modeling of the water-gas shift

reaction on platinum was presented as an example of using these tools in the assessment of the surface reaction mechanism.

While first-principles' microkinetic modeling is feasible for small molecules, it becomes computationally demanding for large mechanisms. In order to overcome this computational bottleneck, a hierarchical approach was proposed. In this approach, semi-empirical methods are first employed to identify key intermediates and reactions, followed by DFT calculations to refine the parameters of those species and reactions. In addition, lateral interactions are computed via DFT only after the most abundant surface species have been predicted. This hierarchical approach minimizes the computational effort by focusing on the most important features of a mechanism (Salciccioli, Stamatakis, Caratzoulas and Vlachos, 2011). Such a methodology allows the development of larger mechanisms for which a DFT-based approach can be time demanding and even lack accuracy. The overall outcome is the generation of important insights into reaction pathways, as well as insights that enable rational catalyst development (Hansgen et al., 2010).

CHAPTER 3. A DFT STUDY OF THE WATER-GAS SHIFT REACTION AND COKE FORMATION ON NI (111) AND (211) SURFACES

3.1. INTRODUCTION

Ni-based catalysts have been used industrially over the past 50 years in steam reforming of natural gas (Sehested, 2006) and methanation (Goodman et al., 1980; Sehested et al., 2005). Newer applications using Ni catalysts includes the production of syngas (H_2 + CO) via steam reforming of biofuels (Busca et al., 2009; Vaidya and Rodrigues, 2006a; Comas et al., 2004; Fajardo and Probst, 2006) and the CO_2 capture via dry reforming of methane (Seok et al., 2001; Wei and Iglesia, 2004). The water-gas shift (WGS) and the reverse water-gas shift (rWGS) reactions (1)

$$CO + H_2O \rightleftharpoons CO_2 + H_2, \qquad \Delta H_{298\,K} = -41\ \text{kJ mol}^{-1}, \qquad (2)$$

are important in these processes. While steam and dry reforming of methane occurs at high temperatures, methanation takes place at low temperatures (~523-623). The temperatures in steam reforming of ethanol span a much larger range, from 573 K to 1073 K. Lower temperatures, where the WGS is kinetically relevant, are common. This calls for the development of detailed kinetic models to provide insights into pathways and improvement of catalyst stability.

The surface reaction mechanism of WGS on Ni is currently not as well understood. Recent focus is centered on the nature of important intermediates and reactions that take place on Ni particles, on the role of the support and on the nature of the active sites involved in the reaction. Grenoble *et al.* (Grenoble et al., 1981) postulated a WGS mechanism that proceeds via formic acid, which is formed over acidic Al_2O_3 sites and is decomposed to CO_2 and H_2 on metal sites. In addition, the redox mechanism has been postulated on Ni/Al_2O_3 (Wheeler et al., 2004; Xu and Froment, 1989) and Ni/CeO_2 (Hilaire et al., 2004) catalysts, whereby CO_2 is produced via the direct oxidation of CO ($CO^* + O^* \rightleftharpoons CO_2^{**}$).

A number of recent observations based on *in-situ* spectroscopy reported formate, carboxyl and carbonate intermediates over Ni surfaces under a variety of feed conditions

(Seok et al., 2001; Jacobs et al., 2004; Sanchez-Escribano et al., 2007; Xie et al., 2011). For example, carbonate species was identified via Fourier Transform Infrared spectroscopy (FTIR) in dry reforming of methane over Ni/γ-Al_2O_3 (Seok et al., 2001), while carbonate and carboxyl species were identified via X-ray Absorption Near Edge Structure (XANES) under liquid hydrocarbon reforming on Ni/CeO_2-Al_2O_3 (Xie et al., 2011). In addition, formate has been identified via FTIR spectroscopy over Ni/Al_2O_3 under methanation conditions (Sanchez-Escribano et al., 2007) and via Diffuse Reflectance Infrared Fourier Transform Spectroscopy (DRIFTS) under WGS conditions over Ni/CeO_2 catalysts (Jacobs et al., 2004). Jacobs *et al.* (Jacobs et al., 2004) postulated a mechanism for WGS on Ni/CeO_2, in which formate is formed over Ce sites. Formate was also identified in well-defined surfaces via High Resolution Electron Energy Loss Spectroscopy (HREELS) under CO_2 hydrogenation over Ni (110) (Wambach et al., 1991; Vesselli et al., 2008). In the past, the decomposition of formic acid and formate was studied using HREELS on Ni (110) (Madix et al., 1983) and on Ni (100) (Benziger and Madix, 1979) and Infrared Reflection Absorption Spectroscopy (IRAS) on Ni (110) (Yamakata et al., 1997) . In the formate school of thought, the most accepted surface reaction mechanism entails unimolecular dehydrogenation ($HCOO^* \rightarrow CO_2^*+H^* \rightarrow CO^*+O^*+H^*$) with formate decomposition as the RDS (Yamakata et al., 1997).

Despite several experimental data on the WGS reaction mechanism on Ni, few computational studies have been performed to understand this reaction. Most studies have focused either on the reforming of methane (Bengaard et al., 2002; Blaylock et al., 2009; Zhu et al., 2009), trends of the WGS reaction over transition metals (Huang et al., 2010; Jelic and Meyer, 2010; Schumacher et al., 2005), the effects of steps and poisons on the reactivity of CH_x species (Bengaard et al., 2002; Abild-Pedersen et al., 2005; Rostrup-Nielsen and Nørskov, 2006), CO methanation via direct C-O bond breaking mechanism (Bengaard et al., 2002; Watwe et al., 2000) and methanol synthesis (Remediakis et al., 2004). Formate is not commonly accounted for in DFT or microkinetic modeling. Very few DFT studies have addressed formate on Ni surfaces, *e.g.*, formate adsorption on Ni (111), (100) and (110) (Pang et al., 2010), formate decomposition on Ni (111) and (211) surfaces (Cao et al., 2009) as well as on Ni (110) (Vesselli et al., 2008).

Regarded to the nature of the active site on WGS reaction, Stamatakis *et al.* (Stamatakis et al., 2011) recently showed that although the WGS reaction on Pt surfaces is structure-insensitive under industrial conditions, both steps and terraces contribute to the overall rate. Additionally, steps are more active under low CO:H_2O ratios. Nørskov *et al.* (Nørskov et al., 2002) showed for several metals that steps are more active to break bonds of diatomic adsorbates, *e.g.*, CO. Specifically on nickel, the activity for steam reforming and methanation reactions has been attributed to the ability of surface steps and defects to decrease the activation energy of C-H bond breaking/forming reactions (Bengaard et al., 2002). However, the role of the surface structure on the C-O bond breaking reaction of WGS adsorbates, *i.e.*, COOH, HCOO, CO_2, CHO, and COH and how the structure affects the activity of WGS and coke formation on nickel catalyst are topics that remain unclear.

To address these questions, we perform of a systematic DFT study of the WGS reaction on Ni (111) and Ni (211) surfaces among 21 elementary-like steps. The chemistries of H_2O and H_2

$$H_2O^* + * \rightleftharpoons OH^* + H^*, \quad \text{(R1)}$$

$$OH^* + * \rightleftharpoons O^* + H^*, \quad \text{(R2)}$$

$$OH^* + OH^* \rightleftharpoons H_2O^* + O^*, \quad \text{(R3)}$$

$$H^* + H^* \rightleftharpoons H_2^* + *, \quad \text{(R4)}$$

are studied together with three different pathways for CO oxidation to CO_2, namely: (i) the direct path

$$CO^* + O^* \rightleftharpoons CO_2^{**}, \quad \text{(R5)}$$

(ii) the carboxyl path

$$CO^* + OH^* \rightleftharpoons COOH^* + *, \quad \text{(R6)}$$

$$COOH^* + 2^* \rightleftharpoons CO_2^{**} + H^*, \quad \text{(R7)}$$

$$COOH^* + O^* + * \rightleftharpoons CO_2^{**} + OH^*, \quad \text{(R8)}$$

$$COOH^* + OH^* + * \rightleftharpoons CO_2^{**} + H_2O^*, \quad \text{(R9)}$$

$$CO^* + H^* \rightleftharpoons COH^* + *, \quad \text{(R10)}$$

$$COOH^* + * \rightleftharpoons COH^* + O^*, \quad \text{(R11)}$$

and (iii) the formate path

$$CO^* + H^* \rightleftharpoons CHO^* + *, \quad \text{(R12)}$$

$$CHO^* + O^* \rightleftharpoons HCOO^{**}, \quad \text{(R13)}$$

$$HCOO^{**} + * \rightleftharpoons CO_2^{**} + H^*, \quad \text{(R14)}$$

$$HCOO^{**} + O^* \rightleftharpoons CO_2^{**} + OH^*. \quad \text{(R15)}$$

$$HCOO^{**} + OH^* \rightleftharpoons CO_2^{**} + H_2O^*. \quad \text{(R16)}$$

In addition, we considered reactions for C-O bond breaking to C and CH intermediates, which are potential precursors of coke and methanation reactions

$$CO^* + CO^* + * \rightleftharpoons C^* + CO_2^{**}, \quad \text{(R17)}$$

$$CO^* + * \rightleftharpoons C^* + O^*, \quad \text{(R18)}$$

$$COH^* + * \rightleftharpoons C^* + OH^*, \quad \text{(R19)}$$

$$CHO^* + * \rightleftharpoons CH^* + O^*, \quad \text{(R20)}$$

$$C^* + H^* \rightleftharpoons CH^* + *. \quad \text{(R21)}$$

To the best of our knowledge, this is the first time that all pathways of this important reaction are studied on Ni (211) surface via DFT. This allows also for the first time the proposition of Brønsted-Evans-Polanyi (BEP) correlations the dehydrogenation and C-O bond breaking reactions on Ni (111) and (211) surfaces. Finally, we postulate potential pathways for the WGS reaction.

This chapter is organized as follows. In the next section, we present details of the DFT calculations. In section 3, we present the binding energies and barriers for the intermediates and reactions, respectively, together with a discussion of the pathways of the WGS reaction on Ni (111) and Ni (211) surfaces. The main conclusions are summarized in section 5.

3.2. QUANTUM MECHANICAL CALCULATIONS

Density Functional Theory (DFT) calculations were performed with the software package SIESTA (Soler et al., 2001), which applies Troullier-Martins norm-conserving scalar relativistic pseudopotentials (Troullier and Martins, 1991). A double zeta plus polarization (DZP) basis set was utilized. The DZP basis offers already quite well converged results, comparable to those used in practice in most plane-wave calculations (Soler et al., 2001), in a good balance between high-quality results and computational cost. The localization radii of the basis functions were determined from an energy shift of 0.01 eV. The basis set superposition error (BSSE) has been tested in a previous publication applying the same DFT scheme (Chen and Vlachos, 2010b), which showed that the differences of the binding energies with and without BSSE correction is within the typical DFT error (< 20 kJ/mol (0.2 eV)). A standard DFT supercell approach, with the Perdew-Burke-Ernzerhof (PBE) form of the generalized gradient approximation (GGA) functional (Perdew et al., 1996), was implemented with a mesh cutoff of 200 Ry. According to the literature (Liu et al., 2003; Fang and Liu, 2010; Cheng et al., 2010) the energy cutoff of 200 Ry is accurate enough for the SIESTA calculations. All calculations were spin-polarized. Calculations were considered converged when all forces on the atoms were lower than a tolerance of 0.05 eV/Å. Self-consistency of the density matrix was achieved when the maximum difference between the output and the input on each element of the matrix in an iteration was lower than 10^{-4} (Soler et al., 2001).

For Ni (111), a 2x2 unit cell with four layers was used. The Brillouin zone was sampled by a 5x5x1 array of k-points in the Monkhorst-Pack grid. The bottom two layers of metal atoms were fixed at the bulk lattice positions, while the top two layers and the adsorbates were allowed to relax. For Ni (211), a 2x1 unit cell with 12 atomic layers was used. For this cell, the Brillouin zone was sampled by a 3x4x1 array of k-points in the Monkhorst-Pack grid, keeping the same density of k-points in the reciprocal space as applied for Ni (111) calculations. The bottom six layers were fixed while the top six layers and the adsorbates were allowed to relax. The computational method results in a self-consistent lattice constant of 3.61 Å for the Ni crystal which compares with the well accepted experimental value (3.52 Å). The use of small unit cells is

common and adequate in systems with small molecules (Bengaard et al., 2002; Chen and Vlachos, 2010b). The convergence of our calculations was tested in terms of the k-points. For example, the differences in the binding energy of CHO is less than 5 kJ/mol on both surfaces when the number of k-points is increased to 6x6x1 and 4x5x1 on Ni (111) and (211) surface, respectively.

The constrained optimization scheme was employed to locate transition states (Alavi et al., 1998; Zhang et al., 1999; Michaelides et al., 1999). Initially, the distance between atoms participating in the bond that forms or breaks was constrained at an estimated value, and the total energy of the system was minimized with respect to all the other degrees of freedom. Then, this procedure was repeated with a new distance until all forces on atoms vanish and the total energy is a maximum along the reaction coordinate but a minimum with respect to the remaining degrees of freedom. The accuracy of the constrained optimization scheme to the system was confirmed by performing a vibrational analysis on the important steps. Vibrational frequencies are computed using the harmonic oscillator approximation based on the diagonalization of the Hessian matrix. Table 3.1 shows the vibrational frequencies calculated for a selected group of reactions. The presence of a single imaginary frequency indicates that the DFT methods access the transition state correctly.

Table 3.1. Vibrational frequencies (υ_k) of the main elementary-like steps on Ni (111) and Ni (211) surfaces, showing the existence of one single imaginary frequency at the transition state.

Elementary Step	υ_k [cm^{-1}]
$CO^*+O^* \rightleftharpoons CO_2^{**}$ on Ni (111)	-438.2, 73.0, 170.6, 254.3, 327.3, 343.4, 388.8, 551.7, 1678.2
$CO^*+O^* \rightleftharpoons CO_2^{**}$ on Ni (211)	-439.6, 23.6, 171.4, 240.4, 292.4, 329.3, 380.9, 557.0, 671.0
$CO^*+OH^* \rightleftharpoons COOH^*+^*$ on Ni (111)	-1264.9, 87.5, 140.1, 206.9, 293.3, 330.1, 427.4, 602.4, 695.2, 921.6, 1202.9, 1606.4
$H_2O^*+^* \rightleftharpoons OH^*+H^*$ on Ni (111)	-748.0, 65.6, 219.4, 371.3, 411.1, 644.4, 723.5, 836.5, 3534.1
$OH^*+^* \rightleftharpoons O^*+H^*$ on Ni (111)	-1146.0, 240.0, 294.8, 421.6, 507.1, 1010.4

Binding energies are calculated as

$$E_{ads} = E_{A/surface} - E_A - E_{surface}\,, \quad (3)$$

where E_A and $E_{surface}$ are the total energies of the isolated adsorbates in vacuum and the clean surface, respectively. $E_{A/surface}$ is the lowest energy among the different sites tested, *e.g.*, atop, bridge, etc. For transition state calculations, $E_{A/surface}$ is the energy at the transition state, E_A is the summation of the total energies of the reactants in vacuum and E_{ads} is the energy at the transition state in relation to the gas-phase reactants. The activation energy is then calculated as the difference between the transition and initial state energies. The initial state energy is the summation of the binding energies of reactants on separate slabs. In the following, the binding energy preferences of all adsorbates and elementary steps are discussed in details.

3.3. RESULTS AND DISCUSSIONS

Table 3.2 presents the binding energies ($\Delta H_{ads,i}$) of all intermediates involved in the mechanism of the most stable configurations on Ni (111) and Ni (211) surfaces. To facilitate comparison, we also tabulate in Table 3.2 previously published results on Ni (111) and on other surfaces when available. In order to find the most stable structure of the intermediates, several binding sites were tested. On Ni (111), the atop, bridge, hcp and fcc binding sites were tested. On Ni (211), atop and bridge sites at the edge of the surface, hcp and fcc sites that are adjacent to the edge and the fourfold hollow and bridge sites at the step of the surface were tested.

Table 3.3 presents the activation energies (E_a) and the bond distance (d) at the transition state for each elementary step on Ni (111) and Ni (211) surfaces along with previously published data. The activation energy of the reverse elementary step is shown in parenthesis. The barriers reported here are the lowest among structures studied. All barriers for the bimolecular reaction are with reactants adsorbed in separate slabs. In general, the structures of the transition states on Ni (111) follows previously published structures when available (Blaylock et al., 2009; Zhu et al., 2009).

Table 3.2. Binding energies ($\Delta H_{ads,i}$) of the intermediates on the most stable sites on Ni (111) and Ni (211) surfaces. Literature results are for the same site preference on the Ni (111) surface, unless otherwise indicated.

Adsorbates	Our results [kJ/mol]		Previous results [kJ/mol]		
	Ni (111)[a]	Ni (211)	Ni (111)	Ni (211)	Other planes
C	-27.7 (h)	-31.2 (4f)	-578.9[1], -554.2[2]		
CH	-28.6 (f)	-29.4 (4f)	-569.3[1], -620.4[2]		
CHO	-10.4 (b)	-10.5 (4f)	-173.7 (h)[1], -218.1 (f)[2], -232.5[3]		-303.0[3] (100)
CO	-8.7 (h)	-8.7 (h1)	-144.7[1], -185.3[2], -175.6[7], -223.8[3]	-188.1(211)[7]	-218.1[3] (100)
COH	-18.5 (f)	-18.2 (h1)	-423.6 (h)[2]		
CO_2	-0.5 (t/t)	-1.3 (t/t)	2.09[1], -1.9[2]	-89.7(211)[8],	-30.9(110)[6]
COOH	-10.6 (b/t)	-10.6 (t/t)	-221.9[1], -218.1 (f)[2]		
H[c]	-11.6 (f)	-11.4 (h1)	-270.2[1], -271.1[2], -284.6[3]		-258.6(110)[6], -273.1(100)[3]
H_2O	-2.0 (t)	-3.0 (t1)	-1.9[1], -28.0[2], -1.0[7], -28.0[4]	-1.9(211)[7]	
HCOO	-12.6 (t/t)	-14.3 (t/t)	-81.0[5]	-296.2(211)[8],	-103.2(100)[5], -154.4(110)[5]
O[c]	-20.1 (f)	-20.1 (h1)	-434.2[1], -547.1[2]		
OH	-14.0 (f)	-14.5 (b1)	-241.2[1], -330.0[2], -301.0[4], -307.8[3]		-324.2(100)[3]

[a] The letter within parenthesis stands for the site preference: t for atop, b for bridge, h for hcp and f for fcc. The number 1 indicates the first position in relation to the edge of the (211) surface. 4f stands for 4-fold hollow site at the step of the (211) surface. [c] Binding energies are relative to atomic species in gas-phase. DFT methods: Ref. 1 (Blaylock et al., 2009) DACAPO code, GGA-RPBE, 2x2 three-layer slab, 6x6x1 k-points, energy cutoff of 340 eV. Ref. 2 (Zhu et al., 2009) VASP code, GGA-PBE, 3x3 four-layer slab, 3x3x1 k-points and an energy cutoff of 400 eV. Ref. 3 (Zhou et al., 2006) STATE code, GGA-PBE, 3x2 three-layer slab, 4x6x1 k-points and an energy cutoff of 25 Ry. Ref. 4 (Phatak et al., 2009) VASP code, GGA-PW91, 3x3 three-layer slab, 3x3x1 k-points and an energy cutoff of 400 eV. Ref. 5 (Pang et al., 2010) STATE code, GGA-PBE, 3x2 three-layer slab, 4x6x1 k-points and an energy cutoff of 25 Ry. Ref. 6 (Vesselli et al., 2008) ESPRESSO code, GGA-PBE, 3x2 slab, 8x8x8 k-points and an energy cutoff of 24 Ry. Ref. 7 (Bengaard et al., 2002) DACAPO code, GGA-RPBE, 2x2 five-layer slab for Ni (111) and 1x2 9-layer slab for Ni (211), energy cutoff of 25 Ry. Ref. 8 (Cao et al., 2009) VASP code, GGA-PW91, 1x2 9-layer slab, energy cutoff of 340 eV.

Table 3.3. Activation energy of the forward ($E_{a,f}$) and backward ($E_{a,b}$) (in parenthesis) elementary-like reactions of WGS on Ni (111) and (211) as well as the bond distance (d) at the transition state on each surface. Non-activated adsorption reactions are not included.

	Reaction	Our results				Previous results / E_a [kJ/mol]	
		Ni (111)		Ni (211)			
		$E_{a,f}$ ($E_{a,b}$) [kJ/mol]	d [Å]	$E_{a,f}$ ($E_{a,b}$) [kJ/mol]	d [Å]	Ni (111)	Other planes
R1	$H_2O^* + * \rightleftharpoons OH^* + H^*$	86.8 (111.0)	1.586	77.2 (85.9)	1.599	88.8[7], 90.7[2], 92.6[4], 88.8[1] (128.3[2])	37.6(211)[7]
R2	$OH^* + * \rightleftharpoons O^* + H^*$	97.5 (111.9)	1.374	112.9 (111.9)	1.691	95.5[7], 111.9[2], 99.4[4], 82.0[1] (130.3[2])	113.9(211)[7]
R3	$OH^* + OH^* \rightleftharpoons H_2O^* + O^*$	0 (0)	1.879	95.5 (86.8)	1.916		
R4	$H^* + H^* \rightleftharpoons H_2^* + *$	132.2 (7.7)	1.562	83.9 (0)	1.548	88.8[2] (5.8[2])	
R5	$CO^* + O^* \rightleftharpoons CO_2^{**}$	147.6 (55.0)	1.707	151.5 (79.1)	1.776	159.2[2], 148.6[1] (64.6[2])	
R6	$CO^* + OH^* \rightleftharpoons COOH^* + *$	117.7 (48.2)	1.741	138.0 (55.0)	1.600	159.2[2], 111.0[1](55.0[2])	
R7	$COOH^* + 2^* \rightleftharpoons CO_2^{**} + H^*$	84.9 (77.2)	1.446	59.8 (68.5)	1.454	82.0[2], 97.5[1] (109.0[2])	

Table 3.3. Continued.

	Reaction	Our results				Previous results / E_a [kJ/mol]	
		Ni (111)		Ni (211)		Ni (111)	Other planes
		$E_{a,f}$ ($E_{a,b}$) [kJ/mol]	d [Å]	$E_{a,f}$ ($E_{a,b}$) [kJ/mol]	d [Å]		
R8	COOH* +O* + * ⇌ CO_2** + OH*	125.4 (102.3)	1.172	7.7 (18.3)	1.226		
R9	COOH* +OH* + * ⇌ CO_2** + H_2O*	0 [a, b] (0)	-	c	-		
R10	CO* + H* ⇌ COH* + *	174.6 (82.0)	1.338	175.6 (80.1)	1.325	190.1[2], 139.9[9] (94.6[2], 85.9[1])	
R11	COOH* + * ⇌ COH* + O*	144.7 (136.0)	1.909	128.3 (115.8)	2.026		
R12	CO* + H* ⇌ CHO* + *	130.3 (19.3)	1.159	140.9 (35.7)	1.483	142.8[2], 143.8[9], 145.7[3] (19.3[2], 20.3[1], 17.4[3])	131.2(100)[3] (76.2(100)[3])
R13	CHO* + O* ⇌ HCOO**	71.4 (121.6)	2.009	56.9 (143.8)	1.957		
R14	HCOO** + * ⇌ CO_2** + H*	101.3 (68.5)	1.461	117.7 (63.7)	1.568		93.6(110)[6] (41.5(110)[6])
R15	HCOO** + O* ⇌ CO_2** + OH*	156.3 (117.7)	1.290	198.8 (145.7)	1.367		

Table 3.3. Continued.

	Reaction	Our results				Previous results / E_a [kJ/mol]	
		Ni (111)		Ni (211)		Ni (111)	Other planes
		$E_{a,f}$ ($E_{a,b}$) [kJ/mol]	d [Å]	$E_{a,f}$ ($E_{a,b}$) [kJ/mol]	d [Å]		
R16	HCOO** + OH* ⇌ CO_2** + H_2O*	174.6 [b] (117.7)	1.317	204.5 (141.8)	1.332		
R17	CO* + CO* + * ⇌ C* + CO_2**	339.6 (109.0)	1.968	[c]	1.879	3.38[1]	
R18	CO* + * ⇌ C* + O*	290.4 (153.4)	1.881	284.6 (227.7)	2.131	2.94[2],3.1[7] (1.59[2], 2.14[1])	2.08(211)[7]
R19	COH* + * ⇌ C* + OH*	199.7 (140.9)	2.295	99.4 (138.9)	1.998	2.01[2] (1.46[2], 1.31[1])	
R20	CHO* + * ⇌ CH* + O*	123.5 (138.0)	1.849	83.0 (111.9)	2.032	1.08[2] (1.53[2], 1.57[1])	
R21	C* + H* ⇌ CH* + *	87.8 (127.4)	1.767	91.7 (72.4)	1.709	0.81[2] (1.33[2], 1.40[1])	

Notes: [a] Obtained using an approximate calculation with a force tolerance of 0.15 eV/Å. [b] Calculation in a 3x3 slab. [c] These transition states were not located as explained in the text.

3.3.1. Structures and Energies of H_2O, H_2 and their Decomposition Intermediates (OH, O and H) on Ni (111) and (211) Surfaces

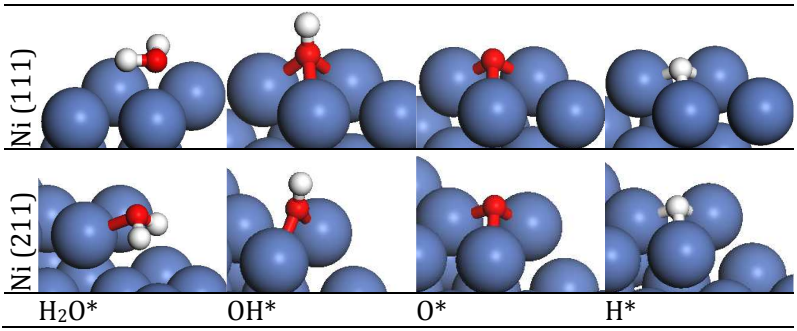

Figure 3.1. Rendering of the adsorption structures on the most stable configuration of H_2O*, OH*, O* and H* on Ni (111) and (211) surfaces. Nickel (blue), carbon (gray), oxygen (red) and hydrogen (white).

Figure 3.1 shows a rendering of the adsorption structures of H_2O, H_2 and their decomposition intermediates (OH, O and H) on Ni (111) and (211) surfaces. Our calculations show that H_2O binds weakly through its oxygen atom on top of the Ni atom on both (111) and (211) surfaces, being 24.1 kJ/mol more stable on Ni (211). Our result on Ni (111) (-45.3 kJ/mol) is in relative good agreement with others predicted using the PBE (-28.0 kJ/mol (Zhu et al., 2009)) and PW91 (-28.0 kJ/mol (Phatak et al., 2009)) functionals. However, it differs substantially from results predicted using the RPBE functional (-1.9 kJ/mol (Blaylock et al., 2009) and -1.0 kJ/mol (Bengaard et al., 2002)). The same difference is found between our result on Ni (211) (-69.5 kJ/mol) and that reported in the literature (-1.9 eV (Bengaard et al., 2002)). A possible explanation for such disagreement may arise from differences in the functionals. Experimentally, Schulze *et al.* (Schulze et al., 1995) reported a H_2O desorption energy of -52.1 kJ/mol on Ni (111), as deduced from thermal desorption spectroscopy (TDS), in good agreement with our predictions.

OH and O bind preferentially on 3-fold fcc hollow sites on both (111) and (211) surfaces. While OH is more stable on Ni (211)

by 12.5 kJ/mol, O has no surface preference. The fourfold coordinated site at the step of the (211) surface was also tested as a binding site; however, both OH and O were 57 kJ/mol and 29 kJ/mol, respectively, less stable than at the most stable configurations reported herein. Our results agree qualitatively with those of Bengaard *et al.* (Bengaard et al., 2002), where OH was found to be ~70 kJ/mol more stable on Ni (211) than on Ni (111) surface. On the other hand, the binding energies of OH and O are slightly higher than those reported before (Blaylock et al., 2009). The differences between our calculations and those of Blaylock *et al.* (Blaylock et al., 2009) arise from the PBE functional used here, which overpredicts the binding energy of atomic O compared to the RPBE functional (Hammer et al., 1999).

Atomic H has no preference between fcc and hcp sites on Ni (111) and is only 13.5 kJ/mol less stable on the bridge site than on fcc and hcp sites. The same behavior was observed on the Ni (211) surface. The binding energies reported here are consistent with previously published results presented in Table 3.2, showing that H is less sensitive to the DFT method.

3.3.2. Structures and Energies of Carbon Species (CO, CO_2, CHO, COH, COOH, HCOO, C and CH) on Ni (111) and (211)

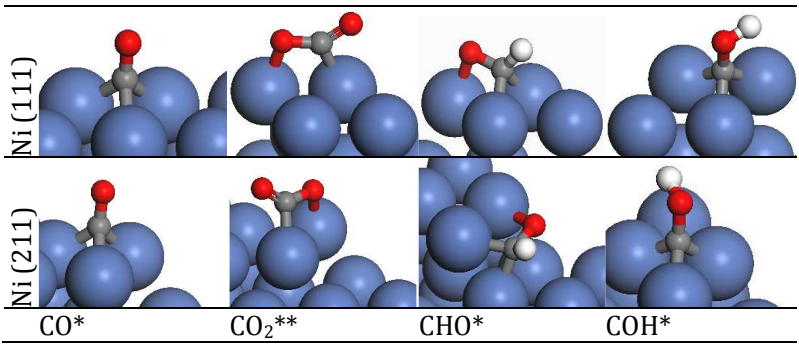

Figure 3.2. Rendering of the adsorption structures on the most stable configuration of CO*, CHO*, CO_2** and COH* on Ni (111) and (211) surfaces

Figure 3.2 shows a rendering of the adsorption structures of the carbon species CO, CO_2, CHO, COH on Ni (111) and (211)

surfaces. Both CO and CHO have no surface preference. CO binds by its C atom at the 3-fold hollow fcc and hcp sites on (111) and (211) surfaces with almost the same energy, whereas CHO binds via C on bridge sites on both surfaces. Interestingly, previous studies reported different site preferences for CHO (Blaylock et al., 2009; Zhu et al., 2009), which is also reflected on weaker binding energy as shown in Table 3.2. Experimentally, the heat of adsorption of CO on Ni, obtained via calorimetry, exhibits a small variation with surface, *e.g.*, -130.3 kJ/mol on Ni (111), -133.1 kJ/mol on Ni (110) and -122.5 kJ/mol on Ni (100) (Stuckless et al., 1993). Our heat of adsorption on Ni (111) is higher by 71.4 kJ/mol. This difference is thought to be mostly due to the inability of the PBE functional in predicting the CO binding energy (Hammer et al., 1999).

CO_2 is 18.3 kJ/mol more stable whereas COH is 6.8 kJ/mol less stable on Ni (211) than on Ni (111). The binding energy of COH on Ni (111) is in good agreement with previous results (Blaylock et al., 2009; Zhu et al., 2009). We also tested the fourfold hollow site for adsorption of COH, but COH is 227.7 kJ/mol less stable. The structure of the adsorbed CO_2 is atop/atop on Ni (111) and Ni (211) surfaces, differently from the "V" configuration reported on Ni (110) (Vesselli et al., 2008).

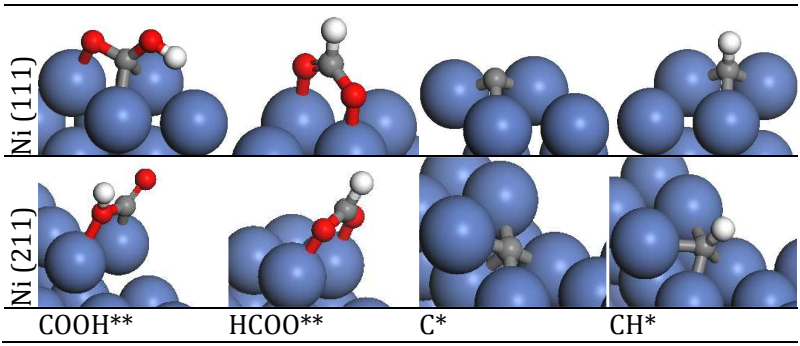

Figure 3.3. Rendering of the adsorption structures on the most stable configuration of COOH**, HCOO**, C* and CH* on Ni (111) and (211) surfaces.

Figure 3.3 shows a rendering of the adsorption structures of COOH, HCOO, C and CH on Ni (111) and (211) surfaces. On Ni (111), COOH is more stable as trans-COOH with the C atom in a bridge-like site and the oxygen of the carbonyl group stabilized in an atop-like

site. On the (211) surface, COOH is positioned with both carbonyl O and H atoms pointing up and away from the surface. Despite its different structures on different surfaces, the COOH binding energy is the same on both surfaces and slightly higher than literature's on Ni (111) (Blaylock et al., 2009; Zhu et al., 2009).

HCOO may take two stable configurations, bi- and mono-dentate. The bi-dentate configuration occupies two adjacent atop sites as showed in the Figure 3.3 while the mono-dentate HCOO prefers an hcp site on the Ni (111) surface. However, mono-dentate is 79.1 kJ/mol less stable than the bi-dentate configuration. The bi-dentate structure is also 43.4 kJ/mol more stable than the mono-dentate one on Cu (111) (Gokhale et al., 2008). The bi-dentate HCOO is 37.6 kJ/mol more stable at the edge of the Ni (211) surface compared to the Ni (111) surface. The most stable structure of the formate is in agreement with experimental observations that reported an inverse "Y" configuration on Ni (110) (Vesselli et al., 2008) and with the most stable structure predicted by DFT on Ni (211) (Cao et al., 2009). Much lower binding energies are reported on Ni (111), (100) and (110) surfaces (Pang et al., 2010) possibly due to differences in structure and binding site.

Finally, C and CH prefer the fourfold hollow site at the step of the (211) surface, by 81.0 kJ/mol and 17.4 kJ/mol, respectively, compared to the (111) surface. This is related to the tetravalence of carbon. These results are in good agreement with those reported by Bengaard *et al.* (Bengaard et al., 2002).

3.3.3. H_2O and OH Activation and H_2 Desorption on Ni (111) and (211) Surfaces

Figure 3.4 shows a rendering of the transition states of the H_2O and OH activations (R1, R2 and R3) on Ni (111) and (211) surfaces. Below, each of these elementary reactions will be explained in details. **$H_2O^*+^*\rightleftharpoons OH^*+H^*$** (R1) and **$OH^*+^*\rightleftharpoons O^*+H^*$** (R2): These two reactions have been studied on Ni (111) (Bengaard et al., 2002; Blaylock et al., 2009; Zhu et al., 2009; Phatak et al., 2009; Wang et al., 2007), but a few studies have focused on low coordinated surfaces (Bengaard et al., 2002). Even though both H_2O and OH are more stable on the Ni (211) surface, activation of these species shows different trends. The barrier for H abstraction from H_2O (R1) is 9.6 kJ/mol lower, whereas the barrier for OH activation

(R2) is 15.4 kJ/mol higher on Ni (211). Our results are in qualitatively agreement with those reported by Bengaard *et al.* (Bengaard et al., 2002), which showed that the barrier for R1 is 53.1 kJ/mol lower, whereas the barrier for R2 is 18.3 kJ/mol is higher on the (211) surface. The O-H bond distance at the transition state of R1 is the same on both surfaces, whereas for R2 is around 0.3 Å longer on Ni (211).

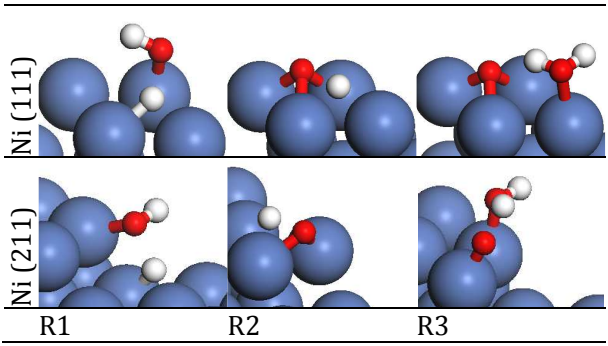

Figure 3.4. Rendering of the transition states of the H_2O and OH activations (R1, R2 and R3) on Ni (111) and (211) surfaces.

$OH^*+OH^* \rightleftharpoons H_2O^*+O^*$ (R3): As far as we know, the OH disproportionation reaction has not been included in DFT studies on Ni. Our calculations indicate that the structure of the transition state on both surfaces is "late" (a product-like). Considering reactants adsorbed on different slabs, the OH disproportionation reaction (R3) is barrierless and almost isenthalpic on Ni (111) and has a barrier of 95.5 kJ/mol on Ni (211). This reaction has a low barrier on other metals as well. For example, the DFT-predicted barrier, considering infinite separation of adsorbates, is 33.8 kJ/mol on Rh (111) and 56.0 kJ/mol on Rh (221) (van Grootel et al., 2009), 0 kJ/mol (Grabow et al., 2008) on Pt (111) and 57.9 kJ/mol on Cu (111) (Gokhale et al., 2008). **$H^*+H^* \rightleftharpoons H_2^*+^*$** (R4): H_2 adsorbs weakly on Ni (111) and Ni (211) surfaces. The H_2 dissociation on Ni (111) has a very low barrier and on Ni (211) is barrierless.

3.3.4. CO Oxidation to CO_2: Direct, Carboxyl and Formate Pathways

Figure 3.5 shows a rendering of the transition states of the CO oxidation by O* and OH* via direct and carboxyl pathways, respectively. Below, each of these elementary-like reactions will be discussed in details.

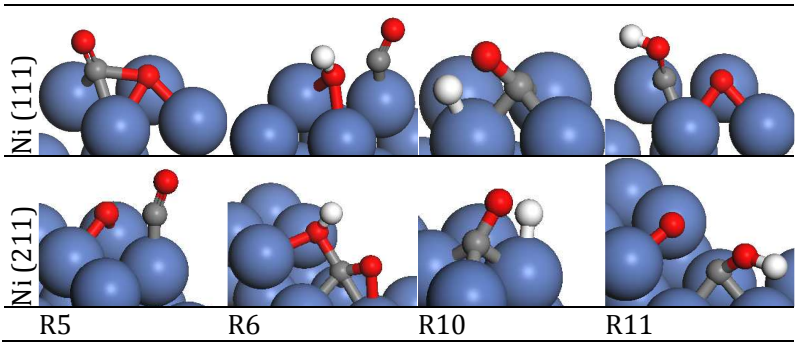

Figure 3.5. Rendering of the transition states of the CO oxidation by O* and OH* via direct (R5) and carboxyl pathways (R6, R10 and R11) on Ni (111) and (211) surfaces.

3.3.4.1. Direct CO Oxidation

$CO^*+O^* \rightleftharpoons CO_2^{**}$ (R5): The reported barrier on Ni (111) spans a large range (*e.g.*, 87.8 kJ/mol (Wang et al., 2007), 148.6 kJ/mol (Blaylock et al., 2009), 159.2 kJ/mol (Zhu et al., 2009). Our results (147.6 kJ/mol and 151.5 kJ/mol for (111) and (211) surfaces, respectively) indicate that the oxidation of CO is favored on Ni (111). Flat surface has low barrier for the direct decomposition of CO_2 (via reverse R5), which make this pathway highly favored for the reverse WGS.

3.3.4.2. CO Oxidation via Carboxyl Pathway

$CO^*+OH^* \rightleftharpoons COOH^*+^*$ (R6): This reaction has the lowest barrier among reactions that consume CO (R5, R6, R9 and R11) on the Ni (111) surface. In agreement with the effect of steps on R5, our results (117.7 kJ/mol and 138.0 kJ/mol for (111) and (211)

surfaces, respectively) indicate that the step increases the barrier in relation to the flat surface. This is due to the higher stability of OH at steps, leading to a more stable initial state. It is interesting that the barrier of the reverse reaction is almost the same on Ni (111) and (211) despite the difference in the structure of COOH and of transition states on the two surfaces. Previously reported barriers for R6 vary considerably (159.2 kJ/mol (Zhu et al., 2009), 111.0 kJ/mol (Blaylock et al., 2009)), probably due to different structures of COOH.

A different pathway for COOH formation was investigated via **CO*+H*⇌COH*+*** (R10) and **COOH*+*⇌COH*+O*** (R11). However, the results indicated that this pathway is not favored due to the high barriers when compared to other reaction competing for the same reactants. For example, the formation of COH is not favored in relation to its isomer CHO by 44.4 and 34.7 kJ/mol on Ni (111) and (211) surfaces, respectively. The O-H bond distance of the R9 and C-O bond distance of R11 at the transition state are nearly the same on both surfaces, indicating the structure-insensitivity of these steps.

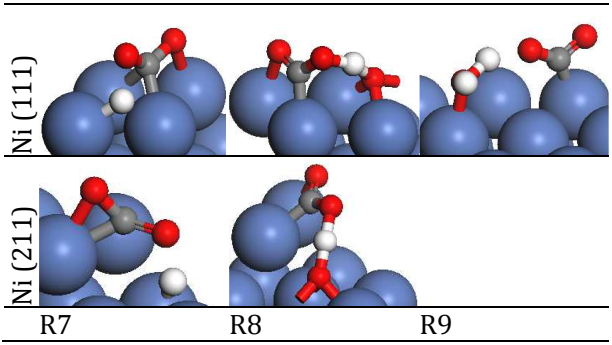

Figure 3.6. Rendering of the transition states of the COOH dehydrogenation reactions (R7, R8 and R20) on Ni (111) and (211) surfaces.

Figure 3.6 shows a rendering of the transition states of the COOH dehydrogenation reactions. Three different elementary steps for COOH dehydrogenation were studied. The results indicated that COOH is easily dehydrogenated to CO_2. The calculated barrier for **COOH*+2*⇌CO_2**+H*** (R7) on Ni (111) (84.9 kJ/mol) is in agreement with previously published results (82.0 kJ/mol (Zhu

et al., 2009), 97.5 kJ/mol (Blaylock et al., 2009)). Additionally, R7 is favored on Ni (211) by 25.1 kJ/mol. The O-H bond distance at the transition state of R7 remains almost the same on both surfaces. **$COOH^*+O^*+^*\rightleftharpoons CO_2^{**}+OH^*$** (R8): On Ni (111), oxygen changes considerably the transition state in relation to the direct dehydrogenation (R7), decreasing the O-H bond distance by 0.27 Å, while increases the barrier. On stepped surface, the dehydrogenation of a COOH on the edge of the surface is aided by one O placed on a hpc site close the the step in a expontaneous reaction. **$COOH^*+OH^*+^*\rightleftharpoons CO_2^{**}+H_2O^*$** (R9): Our calculations indicated that it is hard to locate the transition state of this reaction with a tight tolerance on both surfaces. Same problem was reported by Grabow et al. (Grabow et al., 2008). Considering an approximated calculation with a tolerance of 14.5 kJ/mol, this reaction is barrierless on flat surface.

The reverse WGS via carboxyl pathway is slightly favored on (211) surface due to the lower barriers for the reverse R7. Additionally, the thermal decomposition of COOH to COH + O is slightly exothermic and its barrier is around 1 eV higher than the decomposition to CO + OH (via the reverse of R6) on both (111) and (211) surfaces. This makes the formation of CO + OH from COOH more likely than the formation of COH + O on both surfaces. In comparison with the direct route for the reverse WGS, the results indicated that the direct decomposition (R5) is favored instead carboxyl pathway on Ni (111) surface by 22.2 kJ/mol, while carboxyl pathway is favored on Ni (211) surface by 54.0 kJ/mol. Thus, carboxyl pathway is favored for the CO_2 hydrogenation on stepped surfaces.

3.3.4.3. Formate/Formyl Pathway

The generation of formate was investigated via two different pathways, *i.e.*, via formyl intermediate (R12 and R13) and via CO_2 hydrogenation (R13). Figure 3.7 shows a rendering of both pathways as well as of the dehydrogenation reactions of the formate. The formyl generation via **$CO^*+H^*\rightleftharpoons CHO^*+^*$** (R12) has a barriers similar to the carboxyl formation via R6, and it is slightly favored on Ni (111) surface. However, it is strongly endothermic on both surfaces. The C-H bond distance at the transition state of the

R12 is strongly elongated on Ni (211), showing a changing to a "late" transition state. Oxidation of formyl to formate via **CHO*+O*⇌HCOO**** (R13) is favored on (211) surface by 14.5 kJ/mol and is highly exothermic. In fact, formyl is revealed to be unstable on Ni surfaces, with very low barriers to dehydrogenate via reverse R12 (19.3 kJ/mol and 35.7 kJ/mol on (111) and (211) surfaces, respectively) and to oxidize via R13 on (211) surface (56.9 kJ/mol). Additionally, HCOO is more stable by 37.6 kJ/mol on Ni (211) surface.

Similarly to COOH, three routes for HCOO dehydrogenation were studied. **HCOO**+*⇌CO_2**+H*** (R14): The HCOO dehydrogenation (R14) is favored on Ni (111) surface, consistent with the mechanism of formate generation on stepped surfaces. The C-H bond distance of the transition state of R14 is decreased by 0.4 Å on Ni (211). **HCOO**+O*+*⇌CO_2**+OH*** (R15) and **HCOO**+OH*+*⇌CO_2**+H_2O** (R16): In contrast with the assisted dehydrogenation of COOH, both oxygen and hydroxyl increase the barrier for HCOO dehydrogenation. High barrier for formyl generation and the thermodynamic sink behavior of formate makes this pathway less favored in relation to carboxyl and direct oxidation pathway for WGS reaction.

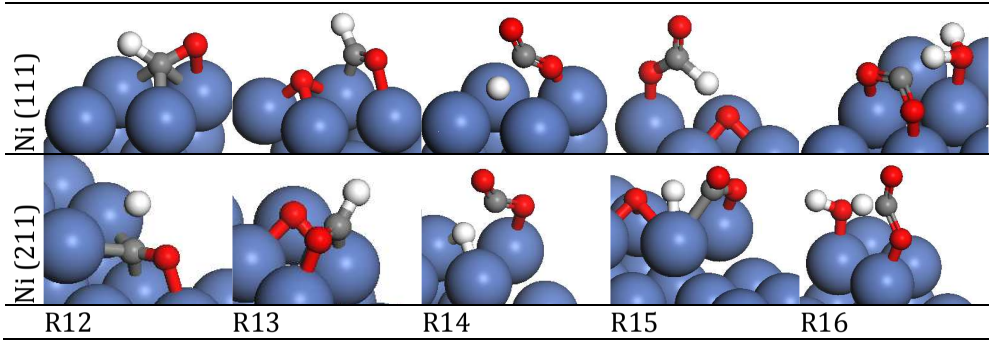

Figure 3.7. Rendering of the transition states of the formate pathway, showing ots formation (R11 and R12) and its dehydrogenation reactions (R13, R14 and R21).

3.3.4.4. Comparison of Pathways for the Water-Gas Shift Reaction and its Reverse on Ni (111) and Ni (211) Surfaces

In order to identify the main pathways for WGS and its reverse on Ni as well as the role of the surface structure, the data presented in Table 3.2 and Table 3.3 were organized in two groups: one on the main WGS reactions that form CO_2 and H_2 (Figure 3.8 and Figure 3.9) and another with reactions that promote C-O bond breaking leading to CH and C (Figure 3.11 and Figure 3.12). The potential pathways for the WGS reaction are discussed next.

Figure 3.8 shows the energy profile for the three pathways of CO oxidation to CO_2 on Ni (111) surface. The direct oxidation route (in black), oxidation via the carboxyl intermediate (in red) and oxidation via the formate intermediate (in blue) are indicated. In addition, the water chemistry is shown (in green). On Ni (111), the carboxyl pathway ($CO + H_2O \overset{R1}{\rightarrow} CO + OH + H \overset{R6}{\rightarrow} COOH + H \overset{R7}{\rightarrow} CO_2 + 2H$) is favored due to the lower barrier for R6 in relation to others that consume CO (R5, R10 and R12). In this pathway, the reaction $CO^*+OH^* \rightleftharpoons COOH^*+^*$ (R6) is the rate determining step. The importance of the carboxyl intermediate on the WGS reaction over Pt was underscored (Mhadeshwar and Vlachos, 2004) using a combination of the UBI-QEP method (Shustorovich and Sellers, 1998) and microkinetic analysis and later using DFT and microkinetic analysis on Pt (Stamatakis et al., 2011; Grabow et al., 2008) and Cu (Gokhale et al., 2008) catalysts.

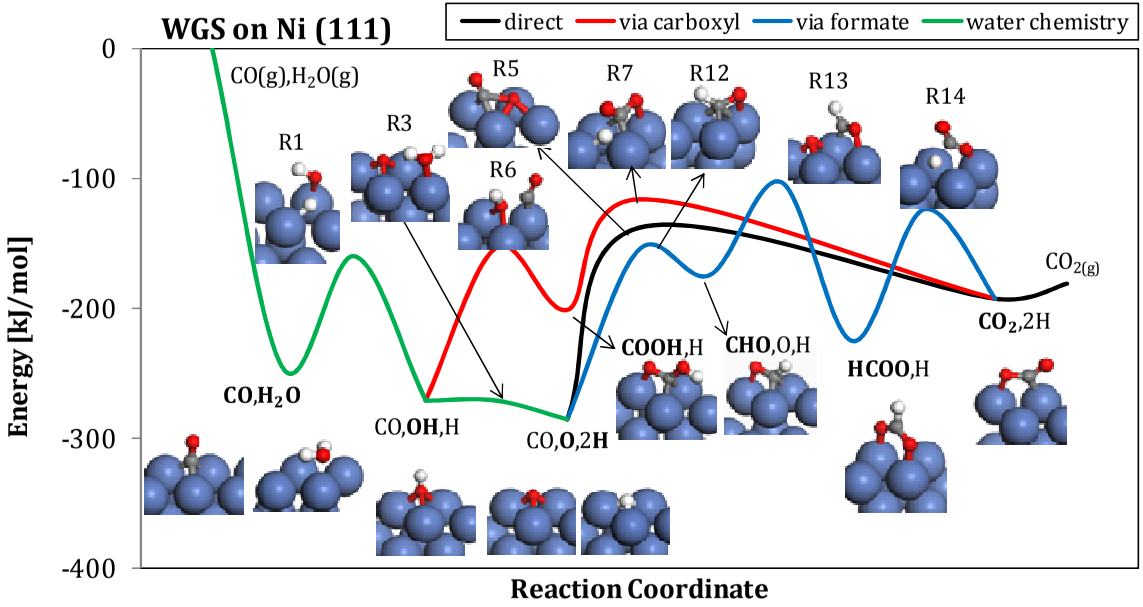

Figure 3.8. Energy profile for WGS reactions on Ni (111). Energies are written in relation to H_2O and CO in the gas-phase. Colors indicate different pathways: direct CO oxidation (black), via carboxyl intermediate (red), via formate intermediate (blue), and water chemistry (green).

Figure 3.9 shows a similar comparison among the pathway on Ni (211) surface. The results reveal two main differences. First, H_2O and CO_2 are more stable and are easily activated on Ni (211) compared to Ni (111) and second, reactions R6 and R12 have similar barriers, indicating that formate pathway may be favored on this surface depending on the reactants involved. The potential pathway to produce CO_2 also depends on the coverage of either O, which would favor $CO^*+O^* \rightleftharpoons CO_2^{**}$ (via the direct path), OH, which would favor $CO^*+OH^* \rightleftharpoons COOH^*+^*$ (via-carboxyl), or H, which would favor $CO^*+H^* \rightleftharpoons CHO^*+^*$ (via-formyl/formate). The OH and O coverage on metallic surface was studied by Phatak *et al.* (Phatak et al., 2009). The authors argue that OH dominates on Pt, Pd, Cu and Au, whereas both OH and O are dominant on Ni under low temperatures and high H_2 partial pressures. This corroborates the idea that the energetics may be a reasonable indicative of the potential pathway for the WGS reaction on Ni. The difference between the RDS on Ni (111) and (211) surface (1.22 eV and 1.43 eV for R6 on flat and on stepped surfaces, respectively) indicates that the Ni (111) is slightly more active for WGS reaction.

Formate behaves like a thermodynamic sink of the formyl/formate pathway with a decomposition barrier higher than 96.5 kJ/mol on both Ni (111) and (211) surfaces and it may be actively involved on Ni (211) surface for high H_2 partial pressures reactions. Thus, elucidating the pathways for formate generation is important. A possible pathway for formate generation is via formyl generation on Ni (111), diffusion of formyl to Ni (211) surface and then formation of HCOO. The barrier for surface diffusion on formyl on Ni (111) was estimated in 12.5 kJ/mol (Blaylock et al., 2009), consistent with the mechanism proposed here. Another pathway for formate generation is by CO_2 hydrogenation via reverse R14. In this pathway, the CO_2 is formed by other pathway is hydrogenated to HCOO. The barrier for CO_2 hydrogenation via reverse R14 is 8.7 kJ/mol higher that the carboxyl pathway (via reverse R7) on Ni (111). On Ni (211) surface, the barriers for these two competing elementary-like steps are the same, showing that this is a possible pathway on steeped surfaces. Taken together with the formyl mechanism, the results indicate that the Ni (211) surface is the favored surface for formation and stabilization of HCOO.

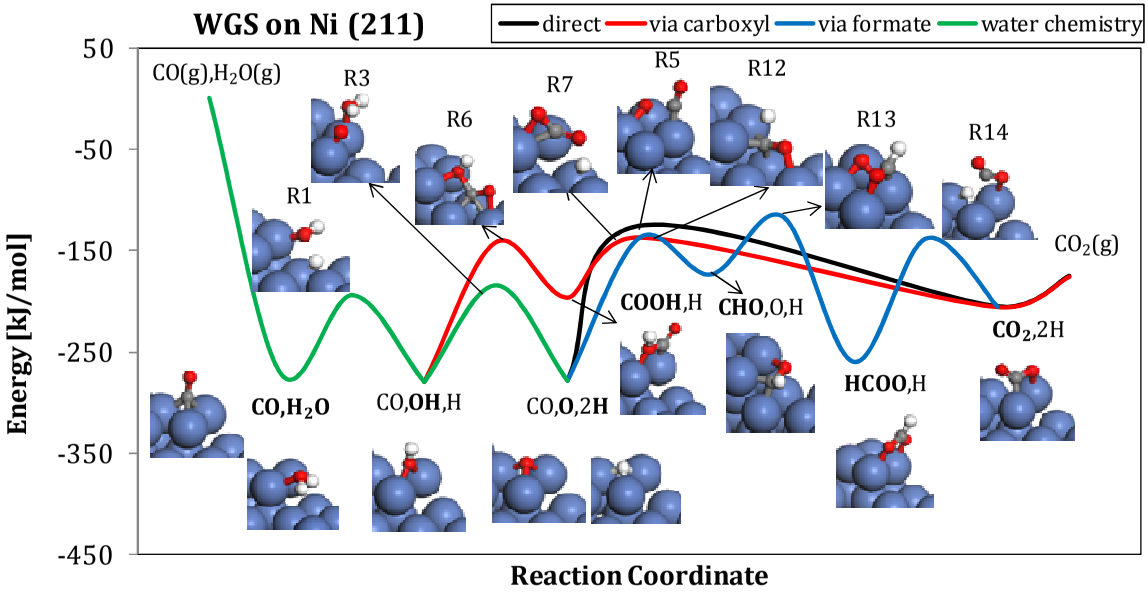

Figure 3.9. Energy profile for WGS reactions on Ni (211). Energies are written in relation to H_2O and CO in the gas-phase. Colors indicate different pathways: direct CO oxidation (black), via carboxyl intermediate (red), via formate intermediate (blue), and water chemistry (green).

For the reverse WGS reaction, the carboxyl route dominates the reaction pathway on Ni (211) while direct CO_2 decomposition (via reverse R5) dominates on Ni (111) surface. Even for high H_2 partial pressures, the formate pathway is not favored due to the high barrier of the reverse R13.

3.3.5. C-O Bond Cleavage Reactions on Ni (111) and Ni (211) Surfaces

In general, our results are in good agreement with previously reported results on Ni (111) as shown in Table 3.3. Bengaard *et al.* (Bengaard et al., 2002) showed that the direct CO decomposition (CO*+*=C*+O*) is favored on Ni (211). Our results support this conclusion also for additional C-O bond cleaving reactions on Ni, namely, CO*+CO*+*⇌C*+CO_2** (R17), COH*+*⇌C*+OH* (R19) and CHO*+*⇌CH*+O* (R20). We discuss individual reactions next. Figure 3.10 shows a rendering of the transition states of the C-O bond breaking reactions.

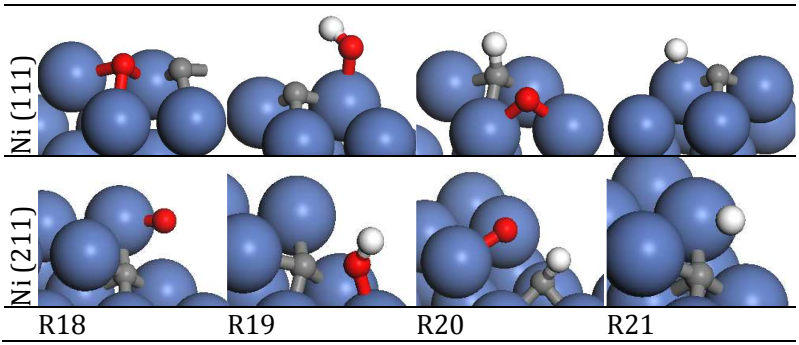

Figure 3.10. Rendering of the transition states of the C-O bond breaking reactions.

3.3.5.1. Decomposition of CO, CHO, COH Intermediates to CH and C

CO*+*⇌C*+O* (R18): The C-O bond distance at the transition state is strongly elongated on Ni (211). However, the calculated barrier of R18 is only 5.8 kJ/mol lower on Ni (211) than on Ni(111), in qualitative agreement with published results (Bengaard et al.,

2002). **CO*+CO*+*⇌CO_2**+C*** (R17): The CO disproportionation reaction that may take place at high CO coverage, typically found in WGS reaction. We were unable to find the transition of this step on Ni (211) surface since it was not possible to find a converged spin state for the first interaction of the density matrix convergence calculation in several configurations of the transition state. However, we succeeded in finding a transition state for this reaction on Ni (111), which indicated a very high barrier. Thus, it is unlikely that this reaction is actively involved in the CO decomposition. **CHO*+*⇌CH*+O** (R20) and **COH*+*⇌C*+OH*** (R19): Decomposition of CHO and its isomer COH is highly favored on Ni (211), (barriers lower by 40.5 kJ/mol and ~95 kJ/mol, respectively) compared to the Ni (111) surface. The distance at the transition state shows different trends; that of R20 is elongated and the transition state is "late"; that of R19 is decreased. Comparing these pathways for C-O bond cleavage, decomposition of formyl on Ni (211) surface is the most likely pathway for atomic C. This pathway is favored on high H_2 partial pressure reaction, *e.g.*, methanation reaction.

C*+H*⇌CH*+* (R21): Dehydrogenation of CH is strongly favored on Ni (211), with a barrier that is 48.2 kJ/mol lower than to Ni (111), although the C-H bond distance at the transition state remains almost the same on both surfaces. This is in agreement with previously reported results (Bengaard et al., 2002). In the reverse direction, the barrier of the hydrogenation of C is lower on Ni (111). This is due to the high stability of atomic C on the hollow site of stepped surfaces. Our results are in good agreement with previously reported results on (111) and (211) surfaces presented in the Table 3.3.

3.3.5.2. Potential Pathways for C-O Cleavage on Ni (111) and Ni (211) Surfaces

Figure 3.11 presents the energy profile for reactions leading to C-O bond breaking and the CH intermediate on Ni (111) surface. Starting from CO+OH+H on Ni (111) (Figure 3.11a), the pathway to CH through formyl ($CO + OH + H \xrightarrow{R12} CHO + OH \xrightarrow{R20} CH + O + OH$) is favored over the direct (R18) and carboxyl paths (R6 and R11). CHO may also produce formate in the presence of O, however, this

pathway is less favored due to formate being a thermodynamic sink. The role of formate in this reaction is more like a spectator. A similar conclusion was reported on Pt (Grabow et al., 2008; Shustorovich and Sellers, 1998) and Cu (Gokhale et al., 2008). The pathway via formyl intermediate is the most prevalent also in the C-O bond breaking reactions on Ni (211) (Figure 3.12). Overall, Ni (211) surface is more active for the C-O bond breaking reactions.

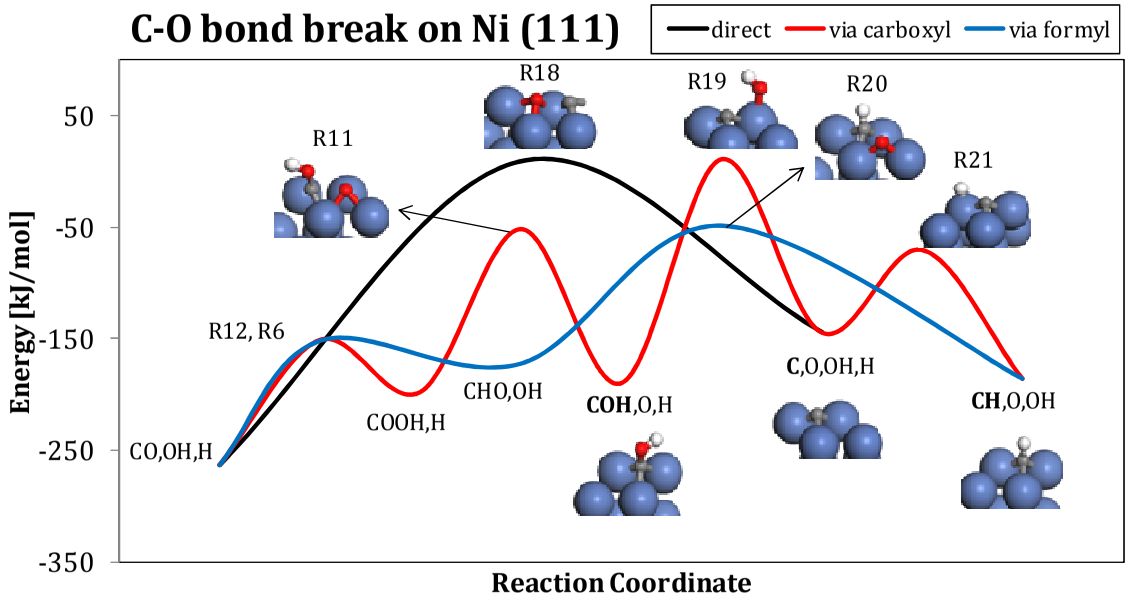

Figure 3.11. Energy profile for C-O bond breaking reactions on Ni (111). Energies are written in relation to H_2O and CO in the gas-phase. Colors indicate different pathways: direct C-O bond break (black), via carboxyl intermediate (red) and via formyl intermediate (blue).

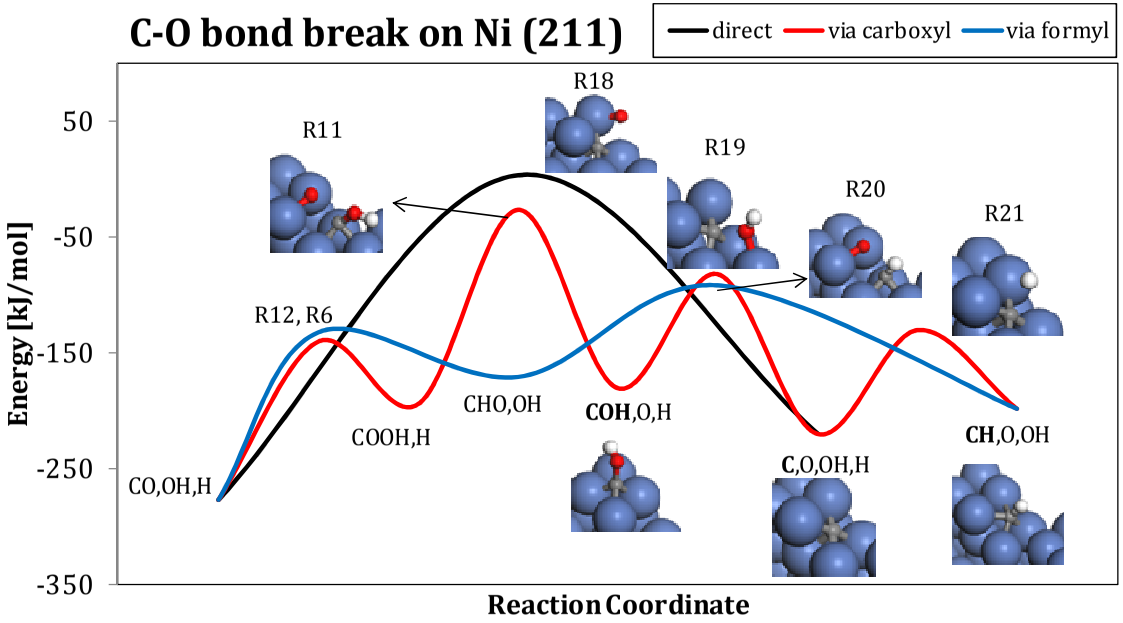

Figure 3.12. Energy profile for C-O bond breaking reactions on Ni (211). Energies are written in relation to H_2O and CO in the gas-phase. Colors indicate different pathways: direct C-O bond break (black), via carboxyl intermediate (red) and via formyl intermediate (blue).

3.3.6. Brønsted-Evans-Polanyi (BEP) Correlations for Dehydrogenation (O-H and C-H) and C-O bond Cleavage Reactions

BEP correlations have been reported among others for bond breaking of diatomic molecules, *e.g.*, CO, O_2, NO and N_2, on flat and stepped surfaces of several metals (Nørskov et al., 2002), for ethanol decomposition (Alcalá et al., 2003), CO oxidation on flat and stepped surfaces (Jiang et al., 2009) and ethylene and ethane chemistry on Pt (111) and Pt (211) surfaces (Chen and Vlachos, 2010b). Recently, BEP correlations have been reported for a WGS surface reaction mechanism consisting of 6 elementary steps (R1, R2, R4 to R7) over transition metals (Huang et al., 2010) and for 7 elementary steps (including R3) on flat bimetallic surfaces (Jelic and Meyer, 2010).As far as we know, no BEP correlations have been reported for a comprehensive set of WGS reactions.

Our calculations indicate that the barriers of reactions can be described with two BEPs, one comprising C-O bond breaking or forming reactions (Figure 3.13) and one for C-H, O-H and H-H bond breaking or forming reactions (Figure 3.14). Disproportionation reactions (R3, R8, R14 and R15) as well as R4 and R19 were not included in these BEPs since they essentially represent a different group. In general, the stepped surface decreases the the energy level of the transition state in relation to the reactants in gas-phase in comparison with the flat surface. This is directly reflected in the interception of the linear regression made for each surface in the Figure 3.13 and Figure 3.14. While this change in the energy is reflected in lower activation energies for C-O bond breaking of CO, COH and CHO, fact that corroborates the conclusions reported by Nørskov *et al.* (Nørskov et al., 2002) for diatomic adsorbates dissociation, the picture for oxygenated species (CO_2, HCOO and COOH) is different. In general, the barriers for C-O, C-H and O-H bond breaking reactions are higher on Ni (211) surface due to the high stability of these species on stepped surface. Although these two BEPs were predicted for only one metal, they are based on a heterogeneous group of reactions, including reactions involving oxygenates. Therefore, they certainly can be used to predict other activation energies, *e.g.*, hydrogenation of CO_2 on other metals.

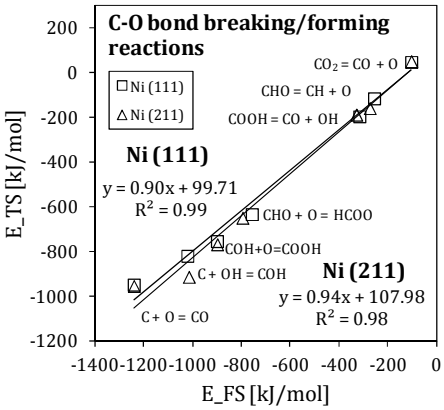

Figure 3.13. BEP correlation for C-O bond breaking/forming reactions on (a) Ni (111) surface and (b) Ni (211) surface. Reactions are written in the exothermic direction according to results on Ni (111). Energies are related to energy of reactants in vacuum.

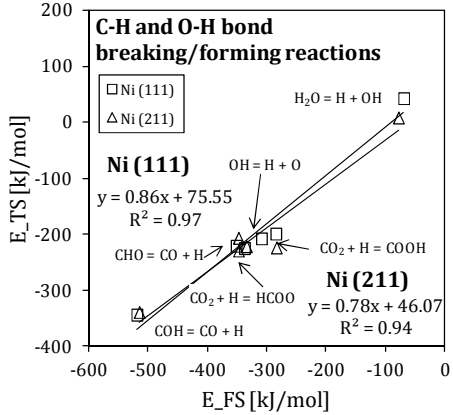

Figure 3.14. BEP correlation for C-H and O-H bond breaking/forming reactions on (a) Ni (111) surface and (b) Ni (211) surface. Reactions are written in the exothermic direction according to results on Ni (111).

3.4. CONCLUSIONS

We reported results of a systematic DFT study of the WGS reaction on Ni (111) and Ni (211) surfaces, consisting of 21 elementary-like steps and 12 surface species. Two Brønsted-Evans-Polanyi (BEP) relationships have been proposed for the dehydrogenation and C-O bond breaking reactions on Ni (111) and (211) surfaces. The analysis of energetics indicates that the carboxyl pathway is favored on both Ni (111) and (211) surfaces and the reaction CO*+OH*⇌COOH*+* is the rate determining step (RDS). However, on Ni (211), the pathway via formate may occur. Generation of formate on the surface is favored on stepped due to the high stability of this species and lower barrier for hydrogenation of CO_2. Ni (211) has lower barriers for H_2O activation (R1) and higher stability of H_2O, OH and CO_2, however, it has a RDS for WGS reaction with a slightly higher barrier than that on Ni (111). Conversion of CO toward CH and C intermediates, which may be precursors of coke and/or methane, is preferred via the formyl intermediate on stepped surfaces.

The two BEP proposed here showed that the structure dependency of the reactions is reflected in lower energy at transition state. While this change in the energy decreases activation energies for C-O bond breaking of CO, COH and CHO, fact that corroborates the conclusions reported by Nørskov *et al.* (Nørskov et al., 2002) for diatomic adsorbates dissociation, the picture for oxygenated species (CO_2, HCOO and COOH) is different. In general, the barriers for C-O, C-H and O-H bond breaking reactions are higher on Ni (211) surface due to the high stability of these species on stepped surface.

As a concluding remark, it is important to observe that steps and terraces play different roles on the WGS reaction. The results suggest that the flat surface is slightly more active for WGS reaction and it is much less active for C-O bond breaking. This offers evidence that flat surfaces would be less deactivated by coke formation, while keeping activity for the WGS reaction. The results presented here are useful in the synthesis of more stable catalysts.

CHAPTER 4. MICROKINETIC MODELING OF THE WATER-GAS SHIFT REACTION ON NICKEL

4.1. INTRODUCTION

A microkinetic model of the water gas shift reaction was developed over the energetics predicted on Ni (111) surface. The objective is to construct a model capable of predicting reaction rates of this important reaction as well as to build a strong support for the conclusions of the DFT analysis. The Ni (111) surface was chosen to represent the energetics due to the results of the DFT study that indicates that the flat surface is a good choice in terms of activity for WGS reaction. Below, the construction of the microkinetic model is briefly described. For details on the methods used, the reader is referred to the Chapter 2. Then, the results are analyzed and confronted with the results of the DFT calculations. Finally, conclusions are summarized.

4.2. DFT-DRIVEN CONSTRUCTION OF THE THERMODYNAMICALLY CONSISTENT SURFACE REACTION MECHANISM

Table 4.1 lists the elementary steps considered in the analysis. The mechanism consists of 19 elementary, reversible steps, involving 4 gas-phase species and 10 adsorbates. The main steps involve adsorption and desorption of reactants and products (R1-R4), chemistries of water (R5-R7) and the oxidation of CO via direct (R8), carboxyl (R9-R14) and formate (R15-R19) mechanisms. Adsorption/desorption steps of intermediates, *i.e.*, H, O, OH, COOH, HCOO, CHO, COH, have been omitted since they are usually only important at high temperatures when gas-phase chemistry occurs (Maestri et al., 2008). No methanation or coke formation reactions were included since the DFT study indicated that these reactions are not favored on the (111) surface.

Transition State Theory (TST) was used to calculate the pre-exponential factors of the forward reactions according to the Eq. (2.16) with $\omega_j = 0.5$ and $\Delta S_j^{DFT} = 0$. Activation energies are assumed as the DFT-predicted values on Ni (111) surface. Reaction constants of the backward reactions are calculated through

equilibrium constant via Eq. (2.8), guaranteeing the thermodynamic consistency.

Table 4.2 shows the surface thermochemistry of all adsorbates involved in the reactions. The enthalpy of each surface species (H_i^0) was carefully calculated to ensure thermodynamic consistency. Several approaches have been used to address thermodynamic consistency at the enthalpic (Grabow et al., 2008; Mhadeshwar et al., 2003; Salciccioli, Chen and Vlachos, 2011; Blaylock et al., 2009) as well as entropic level (Mhadeshwar et al., 2003; Salciccioli, Stamatakis, Caratzoulas and Vlachos, 2011) and good reviews can be found elsewhere (Salciccioli, Stamatakis, Caratzoulas and Vlachos, 2011; Catapan et al., to be published). Here, we use an approach similar to that published by Blaylock *et al*. (Blaylock et al., 2009) and Mhadeshwar and Vlachos (Mhadeshwar et al., 2003), which corrects the enthalpy of adsorption of key species based on experimental values, keeping the enthalpy of surface reactions as predicted from DFT calculations. Experimental values for heat of adsorption were used for CO (Stuckless et al., 1993), H_2O (Schulze et al., 1995) and O (Stuckless et al., 1997) as inputs. Surface enthalpy may be potentially affected by the coverage effects. Coverage effect were firstly predicted by the DFT then tuned to experimental data. The temperature dependency of the heat of adsorption is calculated based on the approach introduced by Mhadeshwar and Vlachos (Mhadeshwar et al., 2003) which takes into account the degrees of freedom lost upon adsorption based on a statistical thermodynamic treatment. These two effects are included in the surface enthalpy according to Eq. (2.27). The entropy of each surface species (S_i^0) is calculated based on method introduced by Santiago *et al.* (Santiago et al., 2000) according to the Eq. (2.16).

The microkinetic model is incorporated in a plug flow reactor model. The set of equations were solved within the framework of the Surface Kinetic Subroutine Library (Coltrin et al., 1991) driven by an in-house code written in FORTRAN90. Supporting concepts and techniques to develop and analyze the microkinetic model include the rate-determining step (RDS), the most abundant surface intermediate (MASI), the most important surface intermediate (MISI), partial equilibrium analysis (PE), global reaction orders and apparent activation energy. An overview of these tools and their computational implementation is given in the Chapter 2.

Table 4.1. Surface reaction mechanism for water gas shift reactions on Ni.

	Reaction	Sticking coefficient $S°_j$ [unitless] or pre-exponential $A_{f,j}$ [mol, cm, s]	Temperature exponent, β_j	Activation energy $Ea_{f,j}$ [kJ/mol]
Adsorption/desorption				
R1	$H_2O + * \rightleftharpoons H_2O*$	0.5	0	0
R2	$CO + * \rightleftharpoons CO*$	0.8	0	0
R3	$CO_2 + * \rightleftharpoons CO_2*$	0.5	0	0
R4	$H_2 + 2* \rightleftharpoons H* + H*$	0.1	0	3.8
Water chemistry				
R5	$H_2O* + * \rightleftharpoons OH* + H*$	2.2978×10^{21}	1.0	87.9
R6	$OH* + * \rightleftharpoons O* + H*$	8.4358×10^{20}	1.0	93.7
R7	$OH* + OH* \rightleftharpoons H_2O* + O*$	7.7469×10^{20}	1.0	0
Direct CO oxidation				
R8	$CO* + O* \rightleftharpoons CO_2**$	5.2995×10^{23}	1.0	145.6
Carboxyl mechanism				
R9	$CO* + OH* \rightleftharpoons COOH**$	3.4328×10^{22} (3.4328×10^{21})	1.0	113.0
R10	$COOH** + * \rightleftharpoons CO_2** + H*$	4.4257×10^{31}	1.0	103.3
R11	$COOH** + OH* \rightleftharpoons CO_2** + H_2O *$	4.0643×10^{31}	1.0	4.2 (0)
R12	$COOH** + O* \rightleftharpoons CO_2** + OH*$	1.1071×10^{32}	1.0	45.2
R13	$COH* + * \rightleftharpoons CO* + H*$	6.3335×10^{20}	1.0	82.0
R14	$COH* + O* \rightleftharpoons COOH**$	2.5773×10^{21}	1.0	138.9

Table 4.1. Continued.

	Reaction	Sticking coefficient S°_j [unitless] or pre-exponential $A_{f,j}$ [mol, cm, s]	Temperature exponent, β_j	Activation energy $Ea_{f,j}$ [kJ/mol]
Formate/formyl mechanism				
R15	CHO* + * ⇌ CO* + H*	6.6107×10^{20}	1.0	20.1
R16	CHO* + O* ⇌ HCOO**	3.2306×10^{21}	1.0	76.1
R17	HCOO** + * ⇌ CO_2** + H*	1.0844×10^{23}	1.0	123.4
R18	HCOO** + OH* ⇌ CO_2** + H_2O*	9.9587×10^{22}	1.0	166.9
R19	HCOO** + O* ⇌ CO_2** + OH*	2.7126×10^{23}	1.0	156.5

Notes: In the reaction description, the asterisk (*) denotes the number of surface sites occupied by the surface species. All reactions were written in order to keep the forward reaction rate controlling the net reaction rate based on the partial equilibrium analysis as explained in the text. The forward reaction rate constant is governed by the modified Arrhenius Eq. (2.16). Reaction rate constant of the surface reactions and adsorption reactions are governed by Eq. (2.3) and (2.7), respectively. Pre-exponential factor are written in concentration units. Site concentration is 2.943×10^{-9} mol/cm^2, considering four sites in a 2x2 slab. Values in parenthesis after pre-exponential factor of the reactions that were tuned to the experimental data are the original values. Activation energy of R11 is changed to assure positive backward activation energy.

Table 4.2. Surface thermochemistry of the WGS adsorbates on Ni (111) surface.

Species	H_i^0 [kJ/mol]	Coverage dependency, α_{ik} [kJ/mol]	Temperature Dependency, δ_i	S_i^0 [J/mol.K]	H_{gas}^0 [kJ/mol]
H_2O	-293.8	$63\theta_{CO} + 36\theta_H$	2.5	41.8	-241.8
OH	-262.3	$63\theta_{CO} + 42\theta_H$	2	37.6	37.3
O	-221.7	$146\theta_{CO} + 64\theta_H$	1.5	16.8	249.1
H	-53.9	$19\theta_{CO} + 4\theta_H$	1.5	5.6	211.8
CO	-240.5	$152\theta_{CO} + 19\theta_H$	2	44.9	-110.5
COH	-203.1		2	70.5	218.1
COOH	-434.5	$63\theta_{CO} + 42\theta_H$	3	90.7	-181.3
CHO	-185.0		2.5	69.8	42.3
HCOO	-458.8		3	93.7	-129.7
CO_2	-370.6		1.5	153.6	-393.4

Notes: Inputs are the experimental heat of adsorption for species CO (Stuckless et al., 1993), H_2O (Schulze et al., 1995) and O (Stuckless et al., 1997). Surface enthalpies are calculated according to Eq. (2.27). The values are valid at 298 K. Values for H_{gas}^0 were taken from the Burcat's database (Goos et al., 2011).

4.3. STRUCTURING THE MECHANISM IN A THERMODYNAMIC CONSISTENT SYSTEM-DRIVEN WAY

It was mentioned previously that the enthalpy of adsorption is coverage- and temperature-dependent. Thus, the enthalpy of reaction is also coverage and temperature dependent. One implication of this dependence is that it is not possible to preserve the DFT-predicted forward and backward activation energies while keeping thermodynamic consistency. The following procedure is proposed here to address this issue.

First, all reactions are written in the exothermic direction, keeping the forward activation energies as predicted by DFT. The backward activation energy is then calculated to ensure thermodynamic consistency using Eq. (2.8), taking into account temperature and coverage effects. A preliminary analysis of the screening mechanism is then performed by running the microkinetic modeling under typical reaction conditions, with inlet mole fractions of 0.31 and 0.24 for H_2O and CO, respectively, balanced with He. In this preliminary calculation, only the DFT-predicted effect of CO coverage on the enthalpy of formation of CO was included since it is well known that CO blocks catalytic sites. Then, all reactions with PE ratio lower than 0.5 were re-written in the backward direction to keep $PE_j > 0.5$, which assures that the forward reaction rate controls the net reaction rate. Remaining reactions were kept in the exothermic direction. The same analysis was made with a feed with high H_2 partial pressure. Partial equilibrium analysis of these two systems after the inversion of the sensitive reactions is shown in the Figure 4.1. Also, H coverage dominates the surface in the high H_2 partial pressure. Coverage effects of H were appropriately included in the model. This approach is said to be system dependent since the PE analysis may change with other reactants, *e.g.*, in the analysis of the reverse water gas shift reaction. However, what must be kept in mind is that this approach has the strong advantage of keeping the confidence between barriers in the mechanism and DFT-predicted activation energies, which is desirable in analyzing reaction mechanisms.

Based on the sensitivity analysis, the mechanism was tuned to the experimental data. In this procedure, the coverage effects were

allowed to relax, while the activation energies and pre-exponentials were fixed.

Table 4.3 shows a comparison among the lateral interaction parameters calculated via DFT and tuned to the experimental data. The reason for this is that coverage parameters carry uncertainties related to the calculation procedure. Periodic calculations performed in a 2x2 supercell represent an approximation of a real system, which may allow adsorbates to be organized in clusters, such as H_2O (Hodgson and Haq, 2009), as well as being adsorbed following other structures. Changes in the interaction parameters of CO and H with both OH and COOH and CO with H_2O were needed. Beyond fitting the lateral interaction parameter, the pre-exponential of the R9 was increased in one order of magnitude and activation energy of R11 is changed to assure positive backward activation energy.

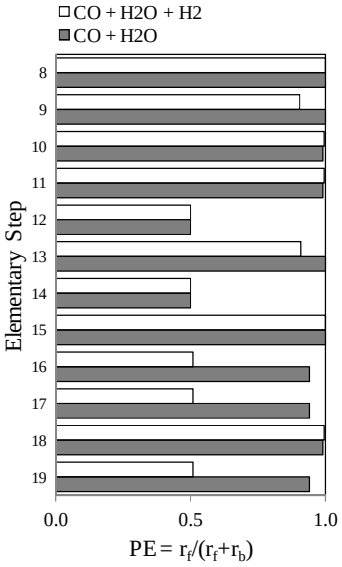

Figure 4.1. Partial equilibrium of each step of the surface reaction mechanism calculated at the end of the reactor of two systems, CO + H_2O and CO + H_2O + H_2. The partial equilibrium analysis takes into account the forward ($\dot{r}_f$) and backward ($\dot{r}_b$) reaction rates.

Table 4.3. DFT-predicted and model tuned coverage effect on the important adsorbates.

Species	$\alpha_{i,CO}$ [kJ/mol]		$\alpha_{i,H}$ [kJ/mol]	
	DFT	tuned	DFT	Tuned
H_2O	-45	63	36	36
OH	146	63	79	42
O	146	146	64	64
H	19	19	4	4
CO	152	152	19	19
COOH	116	63	86	42

Notes: Calculations of the DFT-predicted coverage effect is explained in details in the Chapter 2. The column with the "tuned" values stands for the effect that better represent the experimental data.

4.4. COMPARISON OF THE MODEL PREDICTION TO MEASUREMENTS

Figure 4.2 shows the CO conversion on Ni catalysts predicted by the microkinetic modeling as a function of temperature. The predicted results are in good agreement with the experimental results on Ni/Al_2O_3 (Wheeler et al., 2004) in the low conversion kinetic regime (T < 450°C). The results around 500°C were not tuned since the reaction is probably controlled by mass transfer in this region. At higher temperatures, the reaction is in thermodynamic equilibrium. Neglecting the fact that there is uncertainty in the active catalyst surface area, which can shift the conversion curve along the temperature axis, the ability of the model to match the slope of the conversion vs. temperature data is a good indication that the model is capturing the kinetics appropriately.

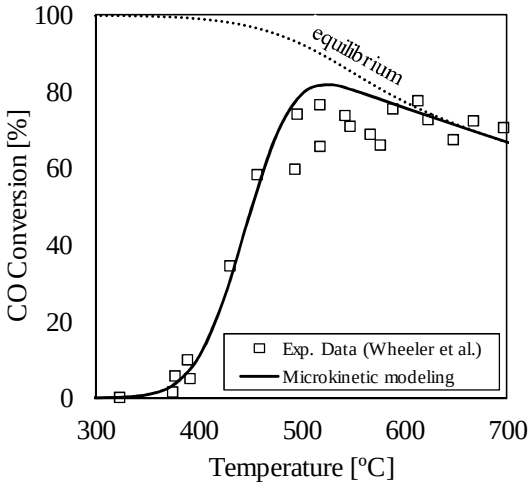

Figure 4.2. Predicted CO conversion using the microkinetic model based on the energetics on Ni (111) surface. Measurements are under atmospheric pressure over Ni/Al_2O_3 from Wheeler *et al*. (Wheeler et al., 2004). Inlet mole fractions are 0.46, 0.11 and 0.23 for H_2O, CO and H_2, respectively, balanced by He. Simulations are performed in a plug flow reactor model under the SURFACE CHEMKIN framework, volume of 2.2 cm^3, length of 1 cm and specific metallic area of 3 x 10^4 cm^{-1}.

Other indications of the accuracy of the microkinetic model are the kinetic parameters such as global reaction orders and the apparent activation energy. On Al_2O_3-supported catalysts, Grenoble et al. (Grenoble et al., 1981), reported an order of approximately zero with respect to CO and half order for H_2O for most of the transition metals. Exceptions are Au and Fe with zero order for H_2O and 0.6-0.7 order for CO. Table 4.4 shows the kinetic parameters predicted by the microkinetic modeling compared to experimental data on Ni/Al_2O_3 (Grenoble et al., 1981). Very good agreement is obtained. The effect of co-feeding H_2 and CO_2 on the WGS kinetics was also studied. The simulations show that H_2 blocks sites with reverse first order kinetics on the WGS activity. On the other hand, the reaction order with respect to CO_2 is zero. Adsorbed atomic H competes for sites with other adsorbates, decreasing the WGS activity. Reverse first-order H_2 kinetics and reverse half order CO_2

kinetics were reported for Pd/CeO_2 (Hilaire et al., 2004) and for Cu-based catalysts (Koryabkina et al., 2003).

Table 4.4. Kinetic parameters predicted at 250°C by the microkinetic model of WGS on Ni against experimental data on Ni/Al_2O_3.

Parameter	Predicted	Exp. Data [1]	Exp. Data [2]
M	-0.14	-0.14	
N	0.54	0.62	
P	0		
Q	-0.42		
Ea_{app} [kJ/mol]	94.3	78.2	111
Reaction rate at 300°C [mol/g-atom.s]	0.7	0.1	

Notes: Parameters are according to $\dot{r} = A_{app}\exp\left(\frac{-E_{a,app}}{RT}\right)[CO]^m[H_2O]^n[CO_2]^p[H_2]^q$. Inlet mole fractions are 0.31 and 0.24 for H_2O and CO, respectively, balanced in He. Parameters from reference 1 (Grenoble et al., 1981) were predicted at 250°C otherwise indicated. Parameters from reference 2 (Boisen et al., 2010) were predicted at 270°C.

4.5. REACTION ANALYSIS IN WATER-GAS SHIFT REACTION

The reaction path analysis is shown in the Figure 4.4. At low temperature regime, CO is consumed by R9 ($CO^* + OH^* \rightleftharpoons COOH^{**}$) via carboxyl mechanism. R18 is responsible for COOH dehydrogenation. As temperature increases, the reaction goes via direct mechanism through R8 ($CO^* + O^* \rightleftharpoons CO_2^{**}$). This is related to the fact that O coverage dominates OH at high temperature as shown in the Figure 4.3. The analysis of the rate determining step is the Figure 4.5 indicates that the reaction R9 controls the rate at low temperature regime. As temperature increases, R18 ($COOH^{**}+OH^* \rightleftharpoons CO_2^{**}+H_2O^*$) becomes relevant. This result corroborates the findings of the DFT study on Ni (111) surface.

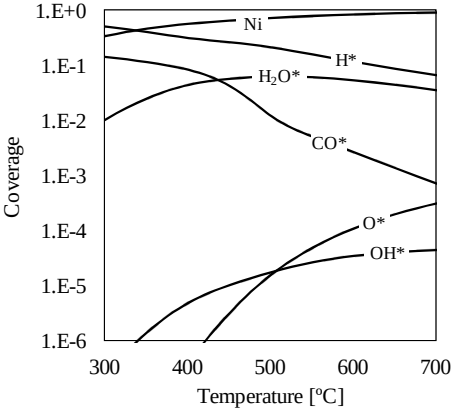

Figure 4.3. Coverage of the adsorbates on Ni at the end of the reactor predicted by the microkinetic modeling as a function of the reaction temperature. Same reaction condition as used in Figure 4.2. Coverage of CO_2, COOH and HCOO were lower than 1 x 10^{-6} and are not shown for clarity.

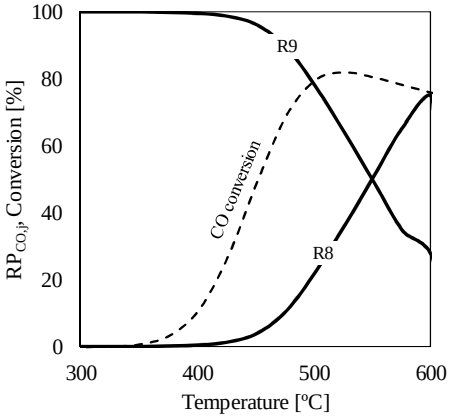

Figure 4.4. Reaction path analysis on the overall consumption rate of the CO. R8 and R9 dominate the consumption in all temperature range. Other CO consumption reactions contribute with less than 1%. CO conversion is also shown.

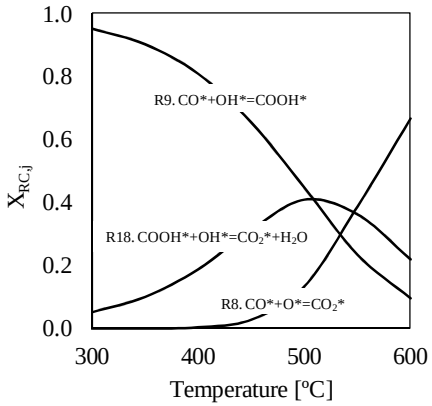

Figure 4.5. Sensitivity analysis of the surface reaction mechanism, indicating the important reactions as a function of temperature. $X_{RC,j}$ is Campbell's degree of rate control (Campbell, 1994). Same reaction condition as used in Figure 4.2, but with different residence times in order to limit the conversion to a maximum of 2% for all temperatures.

4.6. CONCLUSIONS

A microkinetic model of the water gas shift reaction was developed over the energetics predicted on Ni (111) surface. A method for thermodynamic consistency of the DFT-predicted energetics was developed. This method assure that activation energies of the important reactions are represented by the DFT-predicted values while guarantees thermodynamic consistency. The model predictions compares well with experimental results on Ni/Al_2O_3 reported in the literature, reproducing CO conversion, apparent activation energies and reaction orders for CO and H_2O. The analysis of the main reaction pathways revealed that carboxyl pathway is favored and that the elementary step CO*+OH*⇌COOH** is the rate determining step of the reaction. These specific results corroborate the analysis made via DFT, indicating the energetics predicted on the Ni (111) surface is capable of representing rates at the macroscale.

CHAPTER 5. A COMBINED DFT AND SEMI EMPIRICAL STUDY OF THE ENERGETICS OF THE ETHANOL AND THEIR INTERMEDIATES ON NI (111) SURFACE

5.1. INTRODUCTION

The decomposition of ethanol has been studied experimentally since the 80's. For example, Gates *et al.* (Gates et al., 1986) studied the ethanol decomposition on Ni (111) using temperature programmed desorption (TPD) and kinetic of isotopic labeled reactants. They concluded that the main pathway follows successive dehydrogenation steps such as: $CH_3CH_2OH \rightarrow CH_3CH_2O \rightarrow CH_3CHO \rightarrow CH_3CO \rightarrow CH_3$+CO or $CH_2CO \rightarrow CH_2$+CO (the excess of atomic H were omitted). More recently, a similar pathway was proposed for ethanol decomposition on Pt (111) based on fast X-ray photoelectron spectroscopy (XPS) under ultra high vacuum conditions (Lee et al., 2004) and on Pd surfaces based on a review of a series of spectroscopy studies (Mavrikakis and Barteau, 1998). A different pathway was proposed for ethanol decomposition on Rh surfaces to comprise evidences of formation of oxametallacycle species (Sheng et al., 2002; Silva et al., 2008). The accepted mechanism for ethanol decomposition on Rh follows: $CH_3CH_2OH \rightarrow CH_3CH_2O \rightarrow CH_2CH_2O \rightarrow CH_2$+$CH_2O \rightarrow CH_2$+CO.

Despite the existence of accepted reaction mechanisms of ethanol decomposition on transition metals, the picture under steam reforming or partial oxidation conditions may be different. Several groups have reported the presence of acetate and formate species on a variety of supported-transition metals (Yee et al., 1999; Yee et al., 2000; Deng et al., 1995; de Lima et al., 2008; Busca et al., 2009). For example, on CeO_2-supported catalyst Pd/CeO_2 and Pt/CeO_2, carbonate and acetate species were identified via Fourier Transform Infrared spectroscopy (FTIR) after ethanol adsorption (Yee et al., 1999; Yee et al., 2000). Lima *et al.* (de Lima et al., 2008) also reported acetate on $Pt/CeZrO_2$ catalyst under ethanol steam reforming and partial oxidation conditions using Diffuse Reflectance Infrared Fourier Transform Spectroscopy (DRIFTS).

In general, the acetate formation on CeO_2-based catalyst is attributed to the redox properties of this support (de Lima et al., 2008), suggesting that the support is active in this reaction.

However, in the past, acetate species were also reported on well known pre oxidized metallic surfaces under ultra high vacuum conditions (Sim et al., 1996; Houtman et al., 1994; Davis and Barteau, 1988; Tingcheng, 2003). In particular, acetate was identified via Reflection Absorption Infrared spectroscopy (RAIR) on pre oxidized Ag (111) (Sim et al., 1996) and Ni (111) (Tingcheng, 2003) surfaces under acetaldehyde adsorption and via High Resolution Electron Energy Loss Spectroscopy (HREELS) on pre oxidized Rh (111) (Houtman et al., 1994) and on Pd (111) (Davis and Barteau, 1988) surfaces under adsorption of ethanol and acetaldehyde. Using RAMAN spectroscopy, Deng *et al.* (Deng et al., 1995) reported the presence of both ethoxy and acetate over a clean and pre-oxidized Ag surfaces under an ethanol and oxygen flow at 873 K. This suggests that parallel pathways may occur when there is oxygen or hydroxyl on the surface. Presence of acetate species were also identified via in situ FTIR spectroscopy under steam reforming condition over Ni/YSZ catalyst (Busca et al., 2009). In their results, all bands characteristics of C2 species vanish above 673 K, suggesting a C-C bond breaking, in good agreement with results reported by (Yee et al., 2000).

The majority of theoretical works addressing reactions with ethanol on metallic surfaces focus on noble metal catalysts (Kapur et al., 2010; Li et al., 2010; Wang et al., 2010; Pallassana and Neurock, 2002), in particular Pt surfaces (Gursahani et al., 2001; Alcalá et al., 2005; Alcalá et al., 2003), bimetallic catalyst (Pallassana and Neurock, 2002; Alcalá et al., 2005; Skoplyak et al., 2008) and trends among transition metal (Pallassana and Neurock, 2002; Ferrin et al., 2009). For example, in the early years of the past decade, the hydrogenolysis of acetic acid to ethanol on Pd (111), Re (0001) and PdRe alloys (Pallassana and Neurock, 2002), the trends across the periodic table of the oxametalacycle adsorption (Mavrikakis and Barteau, 1998), C-C and C-O bond cleavage on Pt (111) (Alcalá et al., 2003), acid acetic and ethanol decomposition on Pt (111) (Gursahani et al., 2001) and on PtSn-based catalyst (Alcalá et al., 2005) were studied. More recently, the ethanol decomposition on Pd (111) (Li et al., 2010), on Rh (111) and (211) surfaces (Kapur et al., 2010) and the ethanol oxidation on Pd surfaces (Wang et al., 2010) were studied. Decomposition of ethanol on transition metals was also studied using a combination of the BEP and scaling

relations (Ferrin et al., 2009) and periodic DFT calculations (Wang, Lee and Lin, 2009).

Under steam reforming conditions, the presence of water in the feed generates OH and O over the metallic surfaces (Phatak et al., 2009; Blaylock et al., 2009). The elementary steps and the reaction pathways may be different from those of pure decomposition and few works have taken this into account (Wang et al., 2010; Gursahani et al., 2001). For example, hydroxyl radical may react with ethanol intermediates for form acetic acid intermediates, which may be further decomposed on the surface. The work of Wang et al. (Wang et al., 2010) applies a periodic DFT calculation using GGA-PBE level of theory to describe the ethanol decomposition and oxidation on Pd (111), (110) and (100) surfaces. They conclude that the first step of the ethanol dehydrogenation is structure sensitive and that the Pd (100) surface is the more active. The presence of the surface OH aids the dehydrogenation of ethanol intermediates and oxidizes CH_2CO species. In contrast to the mechanisms proposed by Gates *et al.* (Gates et al., 1986) for Ni, the mechanism proposed for Pd surface starts by a C^{α}-H bond breaking. The sequence with the lowest barriers follows: $CH_3CH_2OH \rightarrow CH_3CHOH \rightarrow CH_2CHOH \xrightarrow{+OH} CH_2CHO \xrightarrow{+OH} CH_2CO \xrightarrow{+OH} CH_2COOH \rightarrow CH_2COO \rightarrow CH_2 + CO_2$.

Nonetheless, few studies have included Ni surfaces, mostly in the analysis of trends among metals, despite the fact that Ni is the most used reforming catalyst due to the low cost and good activity. Given this background, we identified a lack of a theoretical work focused on energetics of intermediates of ethanol on Ni surfaces under reforming and oxidation conditions. Here, we present a combined DFT and semi empirical study of the energetics of C_2H_5OH, C_2H_6, C_2H_5OOH, $HCOOH$, CH_4, CH_3OH and their intermediates on Ni (111) surface. Binding energies are calculated via DFT. Since the number of elementary steps scale with the size of reactants and the number of different components in the feed, a full DFT analysis of all possible pathways is time demanding. As an alternative and efficient approach, semi empirical methods were used to analyze this mechanism. Here, activation energies of a selected group of reactions are calculated via periodic DFT. Then, a series of BEP correlations are proposed for the reaction of ethanol on Ni based on these results. Activation energies of the remaining

elementary-like steps are calculated based on the proposed BEP correlations. A reaction path analysis of the decomposition and steam reforming of ethanol on Ni is performed.

5.2. QUANTUM MECHANICAL CALCULATIONS

The binding energies presented in this chapter were calculated following a similar DFT scheme presented in details in chapter 3. The force tolerance between atoms were set to 0.15 eV/Å. Here, a relaxed tolerance is used in comparison with the tolerance applied in the chapter 3 since our ultimate goal is to construct an approximated database for the microkinetic model. Energies in vacuum of the acetic acid, formic acid and their intermediates were calculated applying a similar DFT-scheme used for surface species, with spin polarization and a force tolerance of 0.05 eV/Å. Energies in vacuum for all remaining species were taken from an in-house database (Chen and Vlachos, 2010a) and are consistent with energies used in the present work. The supplementary material of this chapter shows the energies of these species in the most stable configuration in vacuum.

DFT-predicted activation energies are calculated following the same procedure described in details in chapter 3. To calculate the BEP-predicted activation energies, the following procedure is applied. BEP correlations used here correlate energies at the transition state with energies at the final state. These energies are written in relation to the reactants in gas-phase with the reaction in the exothermic direction. It is straightforward to show that the activation energies can be calculated using the following thermodynamic relations,

$$E_{a,b} = E_{TS} - E_{FS}\,, \tag{5.1}$$

$$E_{a,f} = E_{a,b} + \Delta H \tag{5.2}$$

considering exothermic surface reactions.

5.3. ELEMENTARY STEPS

The elementary-like steps included in the present analysis contain C2, C1 chemistries as well as the WGS chemistry presented in chapter 3. For C1 chemistry, the elementary-like steps include

methane and methanol dehydrogenation reactions as well as C-O bond breaking reactions that couple methanol and methane chemistries. For C2 chemistries, dehydrogenation reactions, including C-H and O-H bond breaking, involving ethanol, acetaldehyde, ethane and acetic acid and their intermediates are included. The reason why we considered reactions involving ethane intermediates is due to well known ability of Ni for C-O bond breaking. In the case of acetic acid intermediates and reactions, a series of spectroscopy studies have identified oxygenated species, *e.g.*, acetate (CH_3COO), on Ni catalysis under steam reforming conditions (Yee et al., 1999; Yee et al., 2000; Deng et al., 1995; de Lima et al., 2008; Busca et al., 2009). C-O bond breaking reactions couple the chemistries of ethanol with acetic acid and ethane chemistries, *e.g.*, reactions like $CH_3COO^{**} \rightleftharpoons CH_3CO^{*} + O^{*}$ couple ethanol and acetic acid chemistries, reactions like $CH_3CH_2O^{*} + {*} \rightleftharpoons CH_3CH_2{*} + O^{*}$ couple ethanol and ethane chemistries. The coupling among C2 and C1 chemistries is via C-C bond breaking reactions. In addition to these steps, we also included reactions with intermediates of formic acid.

5.4. RESULTS

5.4.1. Structures and Binding Energies of Ethanol Intermediates on Ni (111)

Here we report the binding energies on Ni (111) surface of all adsorbates that may be involved in the steam reforming of ethanol. Table 5.1 shows the binding of all surface species. Columns 1 to 4 show ethanol, acetaldehyde and their intermediates. Columns 5 to 6 show ethane and their intermediates. Columns 7 to 8 show acetic acid, formic acid and their intermediates. Finally, columns 9 to 10 show species and intermediates usually found in steam reforming of methane.

The binding sites configurations atop, bridge, fcc and hcp were tested for each adsorbate. In general, for intermediates that bind through a carbon atom, the binding site depends on the degree of dehydrogenation of the carbon. As an example, CH_3CH_2 tend to bind in an atop site, CH_3CH to a bridge site while CH_3C to a fcc site. In these cases, the carbon of the methyl radical does not bind to the surface. Intermediates of ethanol in general follow this rule, since

they are usually attached to the surface by a carbon atom. However, this is not a general rule since the presence of a second binding carbon atom may displace the adsorbate to a more stable configuration. For intermediates of the ethoxy species, the oxygen usually binds to the surface in an atop-like site. The intermediates of acetic acid may present two different behaviors. Species with a complete methyl group, *i.e.*, CH_3COOH and CH_3COO, tend to bind by their oxygen atoms on atop sites in an inverse "Y" configuration. Similar behavior was predicted on the adsorption of formate in Chapter 3. However, for more dehydrogenated intermediates, the species tend to bend over the surface.

A different way to visualize the binding trends is to organize the species into smaller groups as shown in Table 5.1. For the group of species that binds over one atom, either C or O, the binding energy may be predicted using the group additivity technique (Salciccioli et al., 2010) by calculating the binding energy of a representative group, *e.g.*, methane and water groups. For example, binding energy of the ethane group may be predicted considering the binding energy of the methane group since CH_3C is equivalent to CH, CH_3CH is equivalent to CH_2, etc, with the methyl group replacing one hydrogen atom. Since methyl group does not bind to the surface, the binding energy is governed by the C-Ni bond energy. Same thought is applied to calculate the binding energy of the ethanol/ethoxy and methanol/methoxy by replacing one hydrogen atom from the water group by a CH_3CH_2 or CH_3 radical. Group additivity technique must be applied to calculate binding energies of groups that binds by two atoms or that have an OH group. Although this behavior may not be applied to all adsorbates listed in the Table 5.1, it decreases the number of calculations required, which is useful in an analysis of a new system.

Table 5.1. DFT-predicted binding energies ($\Delta H_{ads,i}$) of the intermediates involved in the steam reforming of ethanol on the most preferable sites on Ni (111). Results reported in chapter 3 are also presented here for completeness.

Species	$\Delta H_{ads,i}$ [kJ/mol]	Species	$\Delta H_{ads,i}$ [kJ/mol]	Species	$\Delta H_{ads,i}$ [kJ/mol]	Species	$\Delta H_{ads,i}$ [kJ/mol]	Species	$\Delta H_{ads,i}$ [kJ/mol]
C_2H_5OH (ethanol)		CH_3CH_2O (ethoxy)		C_2H_6 (ethane)		CH_3COOH (acetic acid)		CH_3OH (methanol)	
CH_3CH_2OH	-46.3	CH_3CH_2O [a]	-177.5	CH_3CH_3	-12.5	CH_3COOH	-11.6	CH_3OH	-32.8
CH_2CH_2OH [a]	-168.8	CH_2CH_2O	-98.4	CH_3CH_2 [a]	-150.5	CH_2COOH	-181.4	CH_2OH	-167.9
$CHCH_2OH$ [a]	-364.7	$CHCH_2O$ [a]	-491.1	CH_3CH [a]	-359.9	CHCOOH	-339.6	CHOH	-294.3
CCH_2OH	-533.6	CCH_2O	-309.7	CH_3C [a]	-550.0	CCOOH	-501.7	COH	-426.5
CH_2CHOH (ethenol)		CH_3CHO (acetaldehyde)		C_2H_4 (ethene)		CH_3COO (acetate)		CH_3O (methoxy)	
CH_3CHOH	-90.7	CH_3CHO	-61.8	CH_2CH_2	-90.7	CH_3COO	-272.1	CH_3O	-248.0
CH_2CHOH	-52.1	CH_2CHO	-211.3	CH_2CH [a]	-286.6	CH_2COO	-314.5	CH_2O	-77.2
CHCHOH [a]	-286.6	CHCHO [a]	-404.3	CH_2C	-412.0	CHCOO	-224.8	CHO	-240.2
CCHOH [a]	-460.2	CCHO [a]	-498.8	C_2H_2 (ethyne)		CCOO	-586.6	CO	-201.7
CHCOH (ethynol)		CH_3CO (ethanoyl, acetyl)		CHCH [a]	-193.0	HCOOH (formic acid)		CH_4 (methane)	
CH_3COH [a]	-352.2	CH_3CO [a]	-241.2	CHC [a]	-481.5	H_2COOH	-214.2	CH_4	-9.6
CH_2COH	-268.2	CH_2CO	-122.5	CC	-657.1	HCOOH	-39.6	CH_3	-197.8
CHCOH	-304.9	CHCO [a]	-325.2			COOH	-245.1	CH_2	-384.0
CCOH	-509.4	CCO	-447.7			$HC(OH)_2$	-156.3	CH	-660.0
						$C(OH)_2$	-214.2	C	-637.8
						H_2COO	-338.7	H_2O (water)	
						HCOO	-291.4	H_2O	-45.3
						CO_2	-11.6	OH	-322.3
								O	-464.1
								H	-267.3

[a] Binding energies of these intermediates were taken from the work of Sutton and Vlachos (Sutton and Vlachos, 2010).

5.4.2. Derivation of the BEP Correlations

In the present analysis, elementary-like steps involving the intermediates shown in Table 5.1 includes 67 C-H bond breaking, 49 C-O bond breaking, 42 C-C bond breaking and 27 O-H bond breaking, in a total of 185 elementary-like surface reactions. A full DFT analysis of this system would require a tremendous amount of computational work, which makes the analysis time prohibitive. Thus, semi-empirical methods to calculate barriers are required. Here, activation energies of a selected group of elementary steps are calculated via periodic DFT on Ni (111) surface. Then, a series of BEP correlations are proposed based on these calculations and those presented in chapter 3 for Ni (111) surface. Activation energies of the remaining steps are calculated based on these BEP correlations. Validation of these BEP correlations is made by comparing them with other correlations proposed in the literature.

Table 5.2 presents the information regarded to the transition states used to calculate the BEP correlations. Most part of these values were calculated in this work, including the transition states predicted for the water-gas shift reactions presented in Chapter 3. Some values for C-O and C-C bond breaking reaction were taken from the work of Sutton and Vlachos (Sutton and Vlachos, 2010) and were calculated using the same DFT scheme.

Table 5.2. Elementary-like steps used to compose the BEP correlations.

Elementary step	Group	E_{FS} [kJ/mol]	E_{TS} [kJ/mol]	Ea [kJ/mol]	**ΔH** [kJ/mol]	Reference
C-H bond breaking of oxygenates						
CHO* + * = CO* + H*	C1	-351.2	-220.0	20.3	-111.0	This work
CO_2* + H* = HCOO* + *	WGS	-308.8	-208.4	68.5	-32.8	This work
CH_2CH_2OH* + H* = CH_3CH_2OH* + *	C2	-482.4	-371.5	64.6	-45.3	This work
CH_3CHOH* + H* = CH_3CH_2OH* + *	C2	-444.8	-310.7	47.3	-86.8	(Sutton and Vlachos, 2010).
CH_2CH_2O* + H* = CH_3CH_2O* + 2*	C2	-436.1	-332.9	32.8	-69.5	This work
CH_3CHO* + H* = CH_3CH_2O* + *	C2	-334.8	-248.9	80.1	-5.8	This work
CH_3CHO* + 2* = CH_2CHO* + H*	C2	-81.0	20.3	82.0	-19.3	This work
CH_3CHO* + * = CH_3CO* + H*	C2	-126.4	-48.2	13.5	-64.6	This work
O-H bond breaking						
H_2O* + * = H* + OH*	WGS	-68.5	42.5	86.8	-24.1	This work
OH* + * = H* + O*	WGS	-337.7	-224.8	97.5	-14.5	This work
CO_2* + H* = COOH* + 2*	WGS	-284.6	-199.7	77.2	-8.7	This work
COH* + * = CO* + H*	C1	-519.1	-344.5	82.0	-92.6	This work
CH_3CH_2OH* + * = CH_3CH_2O* + H*	C2	-74.3	32.8	83.9	-22.2	This work
CH_3COH* + * = CH_3CO* + H*	C2	-438.0	-307.8	44.4	-84.9	This work
CH_3COOH* + * = CH_3COO* + H*	C2	-119.6	-10.6	1.9	-106.1	This work
C-H bond breaking of hydrocarbons						
C* + H* = CH* + *	C1	-945.6	-817.2	87.8	-40.5	This work
CH_2* + * = CH* + H*	C1	-416.8	-356.0	28.0	-32.8	This work
CH_2* + H* = CH_3* + *	C1	-658.0	-586.6	64.6	-5.8	This work
CH_4 + 2* = CH_3* + H*	C1	-19.3	61.8	71.4	-9.6	This work
CH_2C* + H* = CH_3C* + *	C2	-713.0	-607.9	71.4	-33.8	This work
CH_2CH* + 2* = CHCH* + H*	C2	-333.8	-248.9	40.5	-44.4	This work
CHC* + H* = CHCH* + *	C2	-800.8	-697.6	52.1	-52.1	This work

Table 5.2. Continued.

Elementary step	Group	E_{FS} [kJ/mol]	E_{TS} [kJ/mol]	Ea [kJ/mol]	ΔH [kJ/mol]	Reference
C-O bond breaking						
$CO_2^* = CO^* + O^*$	WGS	-102.3	45.3	55.0	-92.6	This work
$COOH^* + * = CO^* + OH^*$	WGS	-314.5	-196.8	48.2	-69.5	This work
$COH^* + O^* = COOH^* + *$	WGS	-898.3	-753.6	136.0	-8.7	This work
$CHO^* + O^* = HCOO^*$	WGS	-755.5	-633.9	71.4	-51.1	This work
$C^* + O^* = CO^* + *$	WGS	-1238.9	-948.5	153.4	-137.0	This work
$C^* + OH^* = COH^* + *$	C1	-1019.9	-820.1	140.9	-59.8	This work
$CHO^* + * = CH^* + O^*$	C1	-254.7	-116.7	123.5	-13.5	This work
$CHOH^* + * = CH^* + OH^*$	C1	-355.1	-224.8	67.5	-62.7	This work
$CH_3CH_2^* + OH^* = CH_3CH_2OH^* + *$	C2	-484.4	-309.7	166.9	-6.8	(Sutton and Vlachos, 2010).
$CH_3CHOH^* + * = CH_3CH^* + OH^*$	C2	-173.7	-58.9	31.8	-82.0	(Sutton and Vlachos, 2010).
$CH_3COH^* + * = CH_3C^* + OH^*$	C2	-433.2	-298.1	55.0	-80.1	(Sutton and Vlachos, 2010).
$CHCHOH^* + * = CHCH^* + OH^*$	C2	-340.6	-211.3	75.3	-54.0	(Sutton and Vlachos, 2010).
$CHC^* + OH^* = CCHOH^* + *$	C2	-829.8	-667.7	137.0	-25.1	(Sutton and Vlachos, 2010).
$CH_3CH_2^* + O^* = CH_3CH_2O^* + *$	C2	-632.9	-518.1	100.3	-14.5	(Sutton and Vlachos, 2010).
$CH_3CH^* + O^* = CH_3CHO^* + *$	C2	-829.8	-708.2	114.8	-5.8	(Sutton and Vlachos, 2010).
$CH_3CO^* + * = CH_3C^* + O^*$	C2	-285.6	-137.0	138.0	-10.6	(Sutton and Vlachos, 2010).
$CHCHO^* + * = CHCH^* + O^*$	C2	-416.8	-254.7	149.6	-12.5	(Sutton and Vlachos, 2010).
$CHC^* + O^* = CCHO^* + *$	C2	-974.5	-814.3	132.2	-28.9	(Sutton and Vlachos, 2010).
C-C bond breaking reactions						
$CH_3^* + C^* = CH_3C^* + *$	C2	-934.0	-595.3	240.2	-98.4	This work
$CH_2CH^* + * = CH_2^* + CH^*$	C2	-302.0	-286.6	2.9	-12.5	This work
$CH_3CHOH^* + * = CH_3^* + CHOH^*$	C2	-132.2	-28.9	61.8	-41.5	(Sutton and Vlachos, 2010).
$CH^* + CH_2OH^* = CHCH_2OH^* + *$	C2	-837.5	-736.2	93.6	-7.7	(Sutton and Vlachos, 2010).
$CHCOH^* = CH^* + COH^*$	C2	-323.2	-221.0	83.9	-18.3	(Sutton and Vlachos, 2010).
$CH_3^* + CH_2O^* = CH_3CH_2O^* + *$	C2	-336.7	-94.6	183.3	-58.9	(Sutton and Vlachos, 2010).
$CH_3CHO^* + * = CH_3^* + CHO^*$	C2	-64.6	65.6	128.3	-1.9	(Sutton and Vlachos, 2010).
$CHCH_2O^* = CH^* + CH_2O^*$	C2	-520.1	-375.3	115.8	-28.9	(Sutton and Vlachos, 2010).

5.4.2.1. Dehydrogenation Reactions: C-H and O-H Bond Breaking/Forming Reactions

BEP correlations for dehydrogenation reactions are shown in Figure 5.1 and Figure 5.2. Dehydrogenation reactions may be divided into two classes depending on the reactant involved. The first BEP comprises transition states of O-H bond breaking and C-H bond breaking of oxygenates. Figure 5.1 shows the BEP for this class, composed by reactions involving WGS, C1 and C2 intermediates. A small difference is observed in the BEP when compared with the BEP for WGS proposed in chapter 3 due to the scattered of the former. This BEP agrees quantitatively with the correlation proposed by Gu and Li (Gu and Li, 2010) for dehydrogenation of methanol intermediates on Pd (111) and Cu (111) surfaces, within the uncertainties of the DFT calculations. They predicted a slope of 0.96 for Pd (111) and 1.03 for Cu (111) and interceptions of 89.7 kJ/mol for Pd (111) and 83.9 kJ/mol for Cu (111).

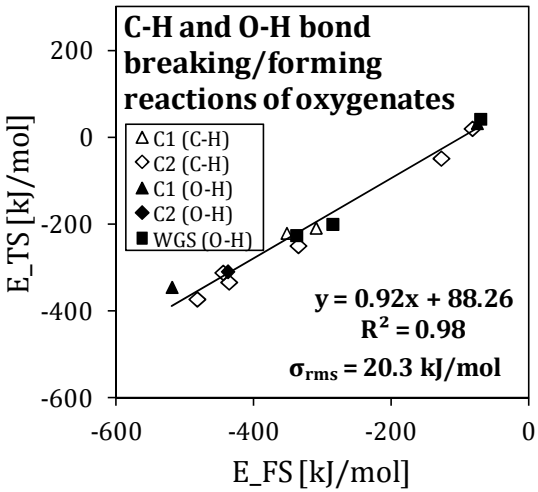

Figure 5.1. BEP correlation for C-H and O-H bond breaking/forming reactions of oxygenates and water-gas shift intermediates.

Dehydrogenation of hydrocarbons (methane, ethane and their intermediates) falls on a different BEP. Adding three transition states calculated for dehydrogenation of ethane intermediates to the BEP predicted in chapter 3, only a small change of 3.9 kJ/mol in the interception is observed. Figure 5.2 shows the BEP for this class of reaction. As a comparison, a BEP for similar elementary-like steps on Pt (111) and (211) surface based on the values published by Chen and Vlachos (Chen and Vlachos, 2010b) gives a slope of 0.84 and an interception of 48.2 kJ/mol. Although the interceptions are similar for Pt and Ni, 48.2 kJ/mol and 66.3±15.4 kJ/mol, respectively, it is thought that geometric effects may be responsible for decreasing the energy at the rendition states for steps involving C2 intermediates.

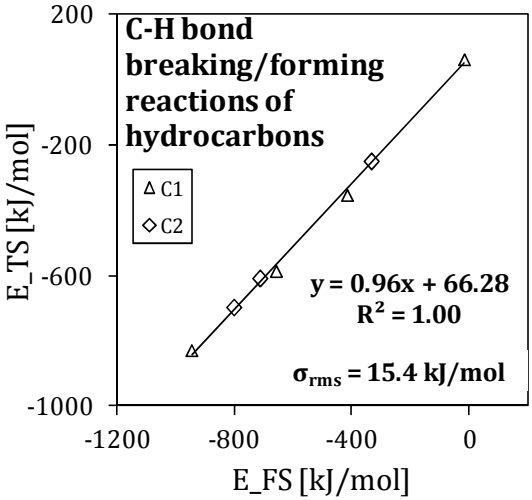

Figure 5.2. BEP correlation for C-H bond breaking/forming reactions of hydrocarbons.

5.4.2.2. C-O and C-C Bond Breaking/Forming Reactions

BEP correlations for C-O and C-C bond breaking reactions are shown in Figure 5.3 and Figure 5.4. Several values predicted fort C-O bond breaking of C1 and C2 intermediates were added to the BEP predicted in chapter 3. Only a small difference is observed between

these BEP, which is within the DFT uncertainties. A best fit for C-O bond breaking BEP gives an interception of 107.0±32.8 kJ/mol and slope of 0.92. This high standard deviation is explained by the heterogeneity of the steps involved.

As observed for dehydrogenation reactions, the C-C bond breaking reactions also fall on two different BEPs, according to the nature of the reactants. Figure 5.4 shows the BEP correlations for C-C bond breaking reaction of oxygenates, which gives an interception of 119.7±20.3 kJ/mol and slope of 1.01. In contrast to these two BEPs for C2 oxygenates, a combined correlation for C-O and C-C bond breaking of ethanol intermediates proposed by Ferrin *et al*. (Ferrin et al., 2009) gives a slope of 0.97 and interception of 139.9±30.9 kJ/mol. Besides the standard deviation of the BEPs, differences in the interceptions may be related to the difference in the DFT scheme used in our work and the work of Ferrin *et al*.. The second class of the BEP for C-C bond breaking is for ethane and its intermediates. Here, the BEP proposed by Chen and Vlachos (Chen and Vlachos, 2010b) on Pt (111) and (211) surfaces were used, which gives an interception of 181.4±28.9 kJ/mol and a slope of 0.99.

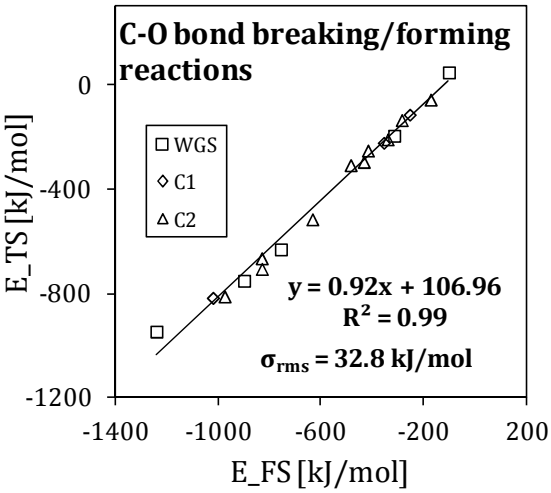

Figure 5.3. BEP correlation for C-O bond breaking/forming reactions.

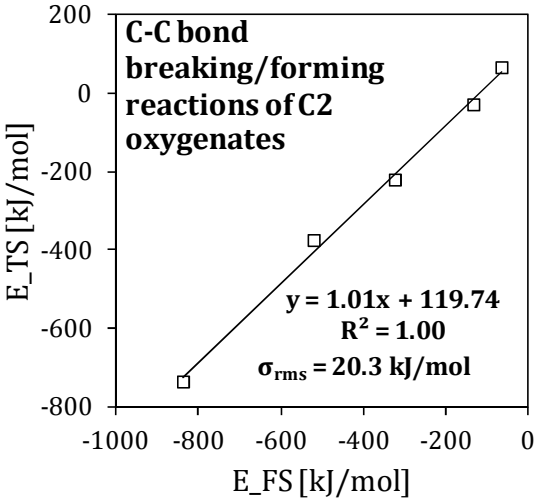

Figure 5.4. BEP correlation for C-C bond breaking/forming reactions of oxygenates.

Table 5.3 shows the slope and interception of the BEP correlations proposed in this work.

Table 5.3. Groups of elementary steps and the BEP correlations, $E_{TS} = A + B * E_{FS}$.

Bond break	Species	A [kJ/mol]	B	Reference
C-H	Hydrocarbons	63.3±15.4	0.96	This work
C-H, O-H	Oxygenates	88.3±20.3	0.92	This work
C-C	Hydrocarbons	181.4±28.9	0.99	(Chen and Vlachos, 2010b)
C-C	Oxygenates	119.7±20.3	1.01	This work
C-O	Oxygenates	107.0±32.8	0.92	This work

5.4.3. Analysis of the Main Reaction Pathways Based on the Energetics

In the last section, a series of BEP correlations were proposed and a validation of these BEPs was presented based on previously published results found in the literature. Another way to verify the validity of the BEP correlations is to identify the main pathways of the ethanol reactions and compare with experimental findings

reported in the literature. We start by analyzing the thermal decomposition, which can be compared with experimental data from references (Gates et al., 1986; Busca et al., 2009). Then, we analyze the role of OH on the reaction pathway and propose a surface reaction mechanism for steam reforming of ethanol on Ni.

5.4.3.1. Thermal Decomposition of Ethanol on Ni

Table 5.4 shows BEP-predicted activation energies for the reaction pathway of ethanol decomposition on Ni. Available DFT-predicted activation energies calculated in this work are shown in parenthesis. The gray cells stand for the most probable pathway. The species in the first line are those involved in the decomposition pathway. Starting from the C_2H_5OH on the surface, the analysis of the energetics clearly shows that the formation of ethoxy species via O-H bond breaking is more likely than other C-H, C-O or C-C bond breaking. In the next step, the BEP correlations predicted similar barriers for C^{β}-H bond breaking, C^{α}-H bond breaking and C-C bond breaking of the ethoxy species. However, the DFT predicted activation energies shows that C^{α}-H is favored, generating CH_3CHO on the surface. Following the pathway, acetaldehyde is easily dehydrogenated to CH_3CO species. This step is also confirmed by the DFT values. The results also indicate that while desorption of acetaldehyde has a barrier of 61.8 kJ/mol, its formation via ethoxy species has a barrier 24.1 kJ/mol higher, considering the DFT results. This suggests that the CH_3CHO formation in gas-phase is controlled by the surface reaction instead of desorption. The surface reaction control of acetaldehyde production from ethanol is reported by Gates *et al.* (Gates et al., 1986) based on TPD experiments.

The next step occurs with the C-C bond breaking of CH_3CO. Hydrogenation of this species is also possible, favoring the desorption of CH_3CHO. This step is followed by the formation of CH_4 from CH_3 + H, with a barrier higher than the CH_3 formation from CH_3CO, which shows that the CH_4 desorption is surface reaction controlled instead of desorption controlled, in agreement with experimental findings reported by Gates *et al.* (Gates et al., 1986). When one looks at the other acetaldehyde intermediates, it is clear that C-C bond breaking is always favored instead of

dehydrogenation or C-O bond breaking reactions, showing that these species are responsible for coupling C1 and C2 chemistries. In summary, our data indicates that the sequence of elementary steps $CH_3CH_2OH \rightarrow CH_3CH_2O + H \rightarrow CH_3CHO + 2H \rightarrow CH_3CO + 3H \rightarrow CH_3 + CO + 3H \rightarrow CH_4 + CO + 2H$ are the most probable pathway for ethanol decomposition on Ni (111) surface. Our predictions are supported by the experimental findings of Gates *et al.* (Gates et al., 1986).

Table 5.4. BEP-predicted activation for the most probable reaction pathway of ethanol decomposition on Ni. Gray cells refer to the most probable reactions for each species. Values in parenthesis stand for the DFT-predicted activation energies. Values in italic refer to the backward activation energies.

	Activation energies [kJ/mol]			
Bond break	Species			
	CH_3CH_2OH	CH_3CH_2O	CH_3CHO	CH_3CO
O-H	71.4 (83.9) -	- *93.6*	- *104.2*	- *125.4*
C^{α}-H	125.4 (134.1) -	116.7 (85.9) -	33.8 (13.5) *111.0 (80.1)*	 *98.4 (78.2)*
C-C	115.8 -	116.7 -	116.7 (128.3) -	68.5 -
C^{β}-H	129.3 (110.0) -	125.4 (102.3) -	75.3 (82.0) -	125.4 -
C-O	143.8 (173.7) -	155.3 (114.8) -	169.8 (120.6) -	118.7 (138.0) -
Desorption	46.3	-	61.8	-

5.4.3.2. Role of OH on the Reaction Framework

Similar to the analysis presented in Table 5.4, Table 5.5 shows the barriers for reactions that may occur with ethanol intermediates in the presence of oxygen or hydroxyl on the surface. The lines with "add O" and "add OH" stand for reactions that lead to acetic acid and their intermediates, *e.g.*, $CH_3CO + OH \rightarrow CH_3COOH$. We see that CH_3CO is more likely to be oxidized by OH generating acetic acid than CH_2CO or CHCO that have very low barriers for C-C bond breaking reactions.

Table 5.5. BEP-predicted activation energies for the oxidation of ethanol intermediates on Ni. The lines with "Add O" and "Add OH" stand for reactions that lead to acetic acid and their intermediates, *e.g.*, $CH_3CO + OH \rightarrow CH_3COOH$.

	Activation energies [kJ/mol]			
Bond break	Species			
	CH_3CO	CH_2CO	CHCO	CCO
C-C	68.5	21.2	20.3	40.5
Add O	122.5	131.2	128.3	153.4
Add OH	111.9	111.9	135.1	141.8

Table 5.6 shows the barriers for acetic acid decomposition. Acetic acid is spontaneously dehydrogenated to acetate, which is a thermodynamic sink of this reaction pathway. This suggests a concentration of such species on the surface, in agreement with spectroscopic findings (Yee et al., 1999; Yee et al., 2000; Deng et al., 1995; de Lima et al., 2008; Busca et al., 2009). Due to the high barriers for dehydrogenation and C-C bond breaking of acetic acid intermediates, one can conclude that this pathway does not contribute to the overall rate in the steam reforming of ethanol.

Table 5.6. BEP-predicted activation energies for the most probable reaction pathway of acetic acid decomposition on Ni. Values in bold refer to the most probable reactions for each species.

	Activation energies [kJ/mol]				
Bond break	Species				
	CH_3COOH	CH_3COO	CH_2COO	CHCOO	CCOO
O-H	0	- 98.4	- 115.8	- 125.4	- 130.3
C-H	65.6 -	146.7 -	130.3 *41.5*	99.4 *122.5*	- *108.1*
C-C	91.7 -	117.7 -	106.1 -	65.6 -	111.0 -
C-O	63.7 -	166.9 -	124.5 -	79.1 -	131.2 -

5.5. CONCLUSIONS

Here, we present a combined DFT and semi empirical study of the energetics of the C_2H_5OH, C_2H_6, CH_3COOH, HCOOH, CH_4, CH_3OH and their intermediates on Ni (111) surface. Binding energies were calculated via DFT. Activation energies of a selected group of reactions are calculated via periodic DFT. Then, a series of BEP correlations are proposed for the reaction of ethanol on Ni. Activation energies of the remaining elementary-like steps are predicted based on the proposed BEP correlations. A reaction path analysis of the decomposition and steam reforming of ethanol on Ni shows that the main pathway for ethanol decomposition are in good agreement with experimental findings reported in the literature. Our results suggest that the sequence $CH_3CH_2OH \rightarrow CH_3CH_2O + H \rightarrow CH_3CHO + 2H \rightarrow CH_3CO + 3H \rightarrow CH_3 + CO + 3H \rightarrow CH_4 + CO + 2H$ is responsible for the overall reaction rate on both ethanol decomposition and steam reforming. Acetate species behaves like a spectator of this reaction. The CH_3CO species is the responsible for linking C1 and C2 chemistries since it has the C-C bond broken. This shows that the results reported here form a consistent and accurate database to develop a surface reaction mechanism for reactions involving ethanol.

CHAPTER 6. MICROKINETIC MODELING OF THE STEAM REFORMING OF ETHANOL ON NICKEL

6.1. INTRODUCTION AND OVERVIEW OF THE EXPERIMENTAL KINETIC DATA

While the past spectroscopy studies reviewed before offer insights on the surface chemistry of ethanol reforming on nickel catalyst, the kinetics if this reaction is not conclusively studied. Experimental works related to the kinetics of the steam reforming of ethanol are scarce. Kinetic studies proposed a variety of kinetic expressions to represent this reaction (Mas, Baronetti, Amadeo and Laborde, 2008; Mas, Bergamini, Baronetti, Amadeo and Laborde, 2008; Akpan et al., 2007; Vaidya and Rodrigues, 2006b). For example, in the work of Mas *et al.* (Mas, Bergamini, Baronetti, Amadeo and Laborde, 2008), the effect of the reactants, including co-feeding of methane, on the conversion in the steam reforming of ethanol on Ni/Al_2O_3 at 823 K to 923 K is analyzed and two models based on the Langmuir-Hinshelwood approach are proposed. The work of Akpan *et al.* (Akpan et al., 2007) applies Langmuir-Hinshwood and Eley-Rideal approaches to describe the kinetics of ethanol on Ni-based catalyst at 673 K to 863 K. Vaidya and Rodrigues (Vaidya and Rodrigues, 2006b) studied the steam reforming of ethanol on $Ru/\gamma\text{-}Al_2O_3$. They derive a kinetic expression assuming that the decomposition of a complex formed by the reaction of adsorbed ethanol and water is the RDS. They concluded that the reaction is first order to ethanol.

Significant differences are observed in the reported activation energies. For the reactions of ethanol with 3 mols of water, the apparent activation energies span from 59.7 kJ/mol (Akpan et al., 2007) to 144 kJ/mol (Mas, Bergamini, Baronetti, Amadeo and Laborde, 2008). Vaidya and Rodrigues (Vaidya and Rodrigues, 2006b) reported activation energy of 96 kJ/mol for steam reforming of ethanol on $Ru/\gamma\text{-}Al_2O_3$. Sun *et al.* (Sun et al., 2005) and Akande *et al.* (Akande et al., 2006) reported activation energies smaller that 16 kJ/mol. Although the range of activation energies observed in the previous mentioned works may be large, it is thought that the former values were measured in the presence of mass diffusion limitations (Mas, Bergamini, Baronetti, Amadeo and Laborde, 2008).

The discrepancies in the activation energies may be related to the method of analysis of the experimental data, which are not collected under the differential condition. Instead, the parameters estimation is mostly based on fitting kinetic expression to experimental data using computational techniques in a large range of temperatures and conversions. Differences in the apparent kinetic parameters may also be related to structure sensitivity of this reaction. Since the data reported were collected at different temperatures, using Ni-based catalysts on different supports and made from different precursors, metallic surface structure may vary significantly, which may affect activity (Honkala et al., 2005; Beebe et al., 1987) and possible selectivity (Vang et al., 2006).

Difficulties in the applicability of the global kinetic expressions developed arise from the fact that they are based on a priori assumptions of the RDS, which may be only valid under the specific experimental conditions analyzed. Using microkinetic modeling techniques, the present study offers a deeper level of understanding on the ethanol steam reforming reaction. A full detailed surface reaction mechanism is developed over the energetics predicted in chapter 5. The objective is to construct a model capable of predicting reaction rates as well as analyze the main pathways of this reaction. The analysis of the main pathway is important in the microkinetic modeling since a thermodynamic consistent kinetic expression may be derived from the results (see, *e.g.*, the work of Salciccioli *et al*. (Salciccioli, Chen and Vlachos, 2011)). Here, the data reported by Mas *et al.* (Mas, Bergamini, Baronetti, Amadeo and Laborde, 2008) on steam reforming of ethanol on Ni/Al_2O_3 catalyst was chosen as a case study to the applicability of the surface mechanism. We understand that for the first time, a full analysis of the ethanol steam reforming mechanism on nickel catalyst is performed in a comprehensive and thermodynamic consistent way.

This chapter is organized as follow. First, the construction of the microkinetic model is briefly described. For details on the methodology, the reader is referred to chapter 2. Then, the results are analyzed and confronted with the results of the DFT and with the experimental data reported in the literature. Finally, conclusions are summarized.

6.2. ELEMENTARY STEPS, THERMOCHEMISTRY AND THERMODYNAMIC CONSISTENCY OF THE ENERGETICS

Table 6.1 lists the surface reaction mechanism considered in our analysis. It consists in the C2 and C1 chemistries, including reactions involving acetic acid and formic acids, together with the water-gas shift reaction analyzed in chapter 4. A total of 205 elementary steps were considered. For the screening mechanism, the BEP predicted activation energies were used to represent the reaction kinetics. Activation energies tuned to the experimental data were used in the WGS mechanism.

Table 6.2 shows the surface thermochemistry of all adsorbates involved in the surface reactions. The enthalpy of each surface species (H_i^0) was carefully calculated to ensure thermodynamic consistency according to the same procedure used in the WGS thermochemistry presented in the Chapter 4. Inputs are the heat of adsorption of CO (Stuckless et al., 1993), H_2O (Schulze et al., 1995) and O (Stuckless et al., 1997). It is worth to remember that this method for thermodynamic consistency correct all the heat of adsorption based in accurate gas-phase database while keeping the energetics on the surfaces, *i.e.*, the heat of all surface reactions, at the DFT level. We choose to keep the same inputs used in the WGS intermediates so the thermodynamic database grows in a thermodynamic consistent way. As it will be shown below, H_2O and CO are important adsorbates. In addition, the adsorptions of H_2O and CO on Ni surfaces are well studied in the literature (Stuckless et al., 1993; Schulze et al., 1995; Stuckless et al., 1997; Hodgson and Haq, 2009), while studies of ethanol adsorption are still scarce.

Table 6.1. Surface reaction mechanism for ethanol steam reforming and water gas shift reactions on Ni.

	Reaction	Sticking coefficient $S°_j$ [unitless] or pre-exponential $A_{f,j}$ [mol, cm, s]	Temperature exponent, β_j	Activation energy $Ea_{f,j}$ [kJ/mol]
Water gas shift mechanism				
Adsorption/desorption				
R1	$H_2O + * \rightleftharpoons H_2O*$	0.5	0	0
R2	$CO + * \rightleftharpoons CO*$	0.8	0	0
R3	$CO_2 + 2* \rightleftharpoons CO_2**$	0.5	0	0
R4	$H_2 + 2* \rightleftharpoons H* + H*$	0.1	0	3.8
Water chemistry				
R5	$H_2O* + * \rightleftharpoons OH* + H*$	9.1804×10^{21} (2.2978×10^{21})	1.0	$71.1+4\theta_H+31\theta_{CHCH}+25\theta_{CCOOH}+29\theta_{CH3C}$ (87.9)
R6	$OH* + * \rightleftharpoons O* + H*$	8.4358×10^{20}	1.0	106.2 (93.7)
R7	$OH* + OH* \rightleftharpoons H_2O* + O*$	7.7469×10^{21} (7.7469×10^{20})	1.0	0 (0)
Direct CO oxidation				
R8	$CO* + O* \rightleftharpoons CO_2**$	5.2995×10^{24} (5.2995×10^{23})	1.0	107.1 (145.6)
Carboxyl mechanism				
R9	$CO* + OH* \rightleftharpoons COOH* + *$	3.4328×10^{22} (3.4328×10^{21})	1.0	113.0
R10	$COOH* + 2* \rightleftharpoons CO_2** + H*$	4.4257×10^{31}	1.0	103.3
R11	$COOH* + OH* + * \rightleftharpoons CO_2** + H_2O*$	4.0643×10^{31}	1.0	4.2
R12	$COOH* + O* + * \rightleftharpoons CO_2** + OH*$	1.1071×10^{32}	1.0	45.2
R13	$COH* + * \rightleftharpoons CO* + H*$	6.3335×10^{20}	1.0	82.0
R14	$COH* + O* \rightleftharpoons COOH* + *$	2.5773×10^{21}	1.0	138.9

Table 6.1. Continued.

	Reaction	Sticking coefficient S°_j [unitless] or pre-exponential $A_{f,j}$ [mol, cm, s]	Temperature exponent, β_j	Activation energy $Ea_{f,j}$ [kJ/mol]
Formate/formyl mechanism				
R15	CHO* + * ⇌ CO* + H*	6.6107×10^{20}	1.0	20.1
R16	CHO* + O* ⇌ HCOO**	3.2306×10^{21}	1.0	76.1
R17	HCOO** + * ⇌ CO_2** + H*	1.0844×10^{23}	1.0	123.4
R18	HCOO** + OH* ⇌ CO_2** + H_2O*	9.9587×10^{22}	1.0	166.9
R19	HCOO** + O* ⇌ CO_2** + OH*	2.7126×10^{23}	1.0	156.5
Methanation and methane steam reforming reactions				
Adsorption/desorption				
R20	CH_4 + 2* ⇌ CH_3* + H*	0.1	0	71.1 (57.1)
R21	CH_2O + * ⇌ CH_2O*	0.5	0	0
R22	CH_3OH + * ⇌ CH_3OH*	0.5	0	0
R23	O_2 + 2* ⇌ 2O*	0.5	0	0
Carbon-oxygen bond cleavage to atomic C and CH				
R24	C* + CO_2** ⇌ CO* + CO* + *	1.5992×10^{19}	1.0	113.0
R25	C* + O* ⇌ CO* + *	4.0164×10^{21}	1.0	153.6
R26	C* + OH* ⇌ COH* + *	5.3496×10^{21}	1.0	138.9
R27	CH* + O* ⇌ CHO* + *	7.5678×10^{22} (2.5678×10^{21})	1.0	107.1 (125.0)
C1 hydrogenation/dehydrogenation reactions				
R28	C* + H* ⇌ CH* + *	5.9225×10^{21}	1.0	74.5
R29	CH_2* + * ⇌ CH* + H*	1.3222×10^{21}	1.0	31.0
R30	CH_3* + * = CH_2* + H*	3.1762×10^{21}	1.0	92.9

Table 6.1. Continued.

	Reaction	Sticking coefficient $S°_j$ [unitless] or pre-exponential $A_{f,j}$ [mol, cm, s]	Temperature exponent, β_j	Activation energy $Ea_{f,j}$ [kJ/mol]
Methanol synthesis/decomposition reactions				
R31	$CHOH^* + * \rightleftharpoons CH^* + OH^*$	1.9934×10^{22}	1.0	71.1
R32	$CHOH^* + * \rightleftharpoons CHO^* + H^*$	1.7251×10^{22}	1.0	52.7
R33	$CHOH^* + * \rightleftharpoons COH^* + H^*$	1.8006×10^{22}	1.0	36.0
R34	$CH_2O^* + * \rightleftharpoons CHO^* + H^*$	4.1419×10^{21}	1.0	43.1
R35	$CH_2OH^* + * \rightleftharpoons CHOH^* + H^*$	1.6989×10^{20}	1.0	85.8
R36	$CH_2OH^* + * \rightleftharpoons CH_2O^* + H^*$	7.0761×10^{20}	1.0	78.7
R37	$CH_3OH^* + * \rightleftharpoons CH_2OH^* + H^*$	3.6880×10^{21}	1.0	90.0
R38	$CH_2O^* + H^* \rightleftharpoons CH_3O^* + *$	3.5768×10^{21}	1.0	70.3
R39	$CH_3OH^* + * \rightleftharpoons CH_3O^* + H^*$	2.0963×10^{21}	1.0	57.3
R40	$CH_2O^* + * \rightleftharpoons CH_2^* + O^*$	2.4889×10^{21}	1.0	78.7
R41	$CH_2OH^* + * \rightleftharpoons CH_2^* + OH^*$	2.0877×10^{21}	1.0	76.1
R42	$CH_3O^* + * \rightleftharpoons CH_3^* + O^*$	9.7552×10^{20}	1.0	95.8
R43	$CH_3OH^* + * \rightleftharpoons CH_3^* + OH^*$	2.4242×10^{21}	1.0	59.4
Ethane hydrogenolysis reactions				
Adsorption/desorption				
R44	$CHCH + 2* \rightleftharpoons CHCH^{**}$	0.50	0.0	0.0
R45	$CH_2CH_2 + 2* \rightleftharpoons CH_2CH_2^{**}$	0.50	0.0	0.0
R46	$CH_3CH_3 + 2* \rightleftharpoons CH_3CH_3^{**}$	0.50	0.0	0.0
Carbon-carbon bond cleavage reactions				
R47	$CH_3^* + CH_3^* \rightleftharpoons CH_3CH_3^{**}$	1.6138×10^{23}	1.0	179.1
R48	$CH_3^* + CH_2^* \rightleftharpoons CH_3CH_2^* + *$	1.0640×10^{21}	1.0	180.3
R49	$CH_3CH^* + * \rightleftharpoons CH_3^* + CH^*$	8.6709×10^{21}	1.0	163.2

Table 6.1. Continued.

	Reaction	Sticking coefficient $S°_j$ [unitless] or pre-exponential $A_{f,j}$ [mol, cm, s]	Temperature exponent, β_j	Activation energy $Ea_{f,j}$ [kJ/mol]
R50	$CH_3C^* + * \rightleftharpoons CH_3^* + C^*$	9.4903×10^{20}	1.0	191.2
R51	$CH_2^* + CH_2^* \rightleftharpoons CH_2CH_2^{**}$	2.6227×10^{20}	1.0	158.2
R52	$CH_2CH^* + * \rightleftharpoons CH_2^* + CH^*$	4.0093×10^{21}	1.0	172.4
R53	$CH_2^* + C^* \rightleftharpoons CH_2C^* + *$	2.1742×10^{21}	1.0	121.8
R54	$CHC^{**} \rightleftharpoons CH^* + C^*$	5.0117×10^{12}	1.0	174.1
R55	$CHCH^{**} \rightleftharpoons CH^* + CH^*$	4.1009×10^{13}	1.0	183.3
R56	$C^* + C^* \rightleftharpoons CC^{**}$	2.9024×10^{21}	1.0	184.5
C2 hydrogenation/dehydrogenation reactions				
R57	$CH_3CH_2^* + H^* \rightleftharpoons CH_3CH_3^{**}$	2.1264×10^{23}	1.0	78.7
R58	$CH_3CH_2^* + * \rightleftharpoons CH_3CH^* + H^*$	7.8294×10^{21} (7.8294×10^{20})	1.0	44.4 (69.5)
R59	$CH_3CH_2^* + 2^* \rightleftharpoons CH_2CH_2^{**} + H^*$	2.6607×10^{28} (2.6607×10^{29})	1.0	54.8
R60	$CH_3CH^* + * \rightleftharpoons CH_3C^* + H^*$	6.8691×10^{21}	1.0	3.3
R61	$CH_3CH^* + * \rightleftharpoons CH_2CH^* + H^*$	6.8691×10^{20} (6.8691×10^{21})	1.0	77.4
R62	$CH_3C^* + * \rightleftharpoons CH_2C^* + H^*$	1.4718×10^{20} (1.4718×10^{21})	1.0	138.1 (95.4)
R63	$CH_2CH_2^{**} \rightleftharpoons CH_2CH^* + H^*$	8.0213×10^{12} (2.0213×10^{13})	1.0	123.0 (89.5)
R64	$CH_2C^* + H^* \rightleftharpoons CH_2CH^* + *$	3.0252×10^{21}	1.0	79.9
R65	$CH_2CH^* + 2^* \rightleftharpoons CHCH^{**} + H^*$	1.5860×10^{29}	1.0	35.6
R66	$CHC^{**} + H^* \rightleftharpoons CH_2C^* + 2^*$	2.2827×10^{21}	1.0	47.3
R67	$CC^{**} + H^* \rightleftharpoons CHC^{**} + *$	5.3349×10^{21}	1.0	87.4
R68	$CHC^{**} + H^* \rightleftharpoons CHCH^{**} + *$	7.2378×10^{20}	1.0	46.4
Ethanol decomposition reactions - Adsorption/desorption				
R69	$CH_3CH_2OH + * \rightleftharpoons CH_3CH_2OH^*$	0.50	0.0	0.0
R70	$CH_3CHO + * \rightleftharpoons CH_3CHO^*$	0.50	0.0	0.0

Table 6.1. Continued.

	Reaction	Sticking coefficient $S°_j$ [unitless] or pre-exponential $A_{f,j}$ [mol, cm, s]	Temperature exponent, β_j	Activation energy $Ea_{f,j}$ [kJ/mol]
Hydrogenation/dehydrogenation reactions				
R71	$CH_3CH_2OH^* + * \rightleftharpoons CH_2CH_2OH^* + H^*$	7.9356×10^{20} (7.9356×10^{21})	1.0	126.4
R72	$CH_3CH_2OH^* + * \rightleftharpoons CH_3CHOH^* + H^*$	4.8451×10^{20} (4.8451×10^{21})	1.0	123.4
R73	$CH_3CHOH^* + 2^* \rightleftharpoons CH_2CHOH^{**} + H^*$	4.3756×10^{29}	1.0	54.0
R74	$CH_3CHOH^* + * \rightleftharpoons CH_3COH^* + H^*$	1.2660×10^{21}	1.0	19.2
R75	$CH_2COH^{**} + H^* \rightleftharpoons CH_3COH^* + 2^*$	2.2908×10^{21}	1.0	124.3
R76	$CH_2CH_2OH^* + * \rightleftharpoons CHCH_2OH^* + H^*$	7.8613×10^{20}	1.0	84.5
R77	$CH_2CH_2OH^* + 2^* \rightleftharpoons CH_2CHOH^{**} + H^*$	2.6715×10^{29}	1.0	97.9
R78	$CHCHOH^* + H^* \rightleftharpoons CH_2CHOH^* + *$	2.1793×10^{21}	1.0	95.0
R79	$CH_2COH^* + H^* \rightleftharpoons CH_2CHOH^* + *$	2.3298×10^{21}	1.0	95.0
R80	$CH_2COH^* + * \rightleftharpoons CHCOH^* + H^*$	1.1539×10^{21}	1.0	58.2
R81	$CCH_2OH^* + H^* \rightleftharpoons CHCH_2OH^* + *$	2.1793×10^{21}	1.0	120.9
R82	$CHCHOH^{**} + H^* \rightleftharpoons CHCH_2OH^* + 2^*$	2.1793×10^{21}	1.0	118.4
R83	$CHCHOH^* + * \rightleftharpoons CCHOH^* + H^*$	1.0793×10^{21}	1.0	85.8
R84	$CHCHOH^* + * \rightleftharpoons CHCOH^* + H^*$	1.0793×10^{21}	1.0	59.8
R85	$CCOH^* + H^* \rightleftharpoons CHCOH^* + *$	1.9332×10^{21}	1.0	126.8
R86	$CCHOH^{**} + H^* \rightleftharpoons CCH_2OH^* + 2^*$	4.1254×10^{21}	1.0	142.7
R87	$CCHOH^* + * \rightleftharpoons CCOH^* + H^*$	2.3033×10^{21}	1.0	121.8
R88	$CH_3CH_2O^* + 2^* \rightleftharpoons CH_2CH_2O^{**} + H^*$	1.3975×10^{28} (1.3975×10^{29})	1.0	138.1 (122.6)
R89	$CH_3CH_2O^* + * \rightleftharpoons CH_3CHO^* + H^*$	3.3711×10^{20} (1.3711×10^{21})	1.0	$133.9+12\theta_H+63\theta_{CHCH}+50\theta_{CHCH}$ (114.6)
R90	$CH_3CHO^* + 2^* \rightleftharpoons CH_2CHO^{**} + H^*$	1.0334×10^{30}	1.0	75.7
R91	$CH_3CHO^* + * \rightleftharpoons CH_3CO^* + H^*$	3.6609×10^{21}	1.0	33.9

Table 6.1. Continued.

	Reaction	Sticking coefficient $S°_j$ [unitless] or pre-exponential $A_{f,j}$ [mol, cm, s]	Temperature exponent, β_j	Activation energy $Ea_{f,j}$ [kJ/mol]
R92	$CH_3CO^* + 2^* \rightleftharpoons CH_2CO^{**} + H^*$	4.0835×10^{29}	1.0	123.4
R93	$CHCH_2O^* + H^* \rightleftharpoons CH_2CH_2O^* + *$	3.6482×10^{20}	1.0	96.7
R94	$CH_2CHO^* + H^* \rightleftharpoons CH_2CH_2O^* + *$	4.3918×10^{20}	1.0	102.5
R95	$CH_2CHO^* + * \rightleftharpoons CHCHO^* + H^*$	1.4465×10^{21}	1.0	95.4
R96	$CH_2CHO^* + * \rightleftharpoons CH_2CO^* + H^*$	1.4465×10^{21}	1.0	119.7
R97	$CH_2CO^* + * \rightleftharpoons CHCO^* + H^*$	2.2503×10^{21}	1.0	41.8
R98	$CHCH_2O^* + * \rightleftharpoons CCH_2O^* + H^*$	4.5144×10^{23}	1.0	115.1
R99	$CHCH_2O^* + * \rightleftharpoons CHCHO^* + H^*$	1.2016×10^{21}	1.0	48.1
R100	$CCHO^* + H^* \rightleftharpoons CHCHO^* + *$	1.9787×10^{21}	1.0	138.9
R101	$CHCHO^* + * \rightleftharpoons CHCO^* + H^*$	2.2503×10^{21}	1.0	106.7
R102	$CHCO^{**} \rightleftharpoons CCO^* + H^*$	4.2550×10^{12}	1.0	146.4
R103	$CCH_2O^* + * \rightleftharpoons CCHO^* + H^*$	5.9897×10^{18}	1.0	56.1
R104	$CCHO^{**} \rightleftharpoons CCO^* + H^*$	4.2550×10^{12}	1.0	121.8
Oxygen-hydrogen bond cleavage reactions				
R105	$CH_3CH_2OH^* + * \rightleftharpoons CH_3CH_2O^* + H^*$	2.4140×10^{21}	1.0	71.5
R106	$CH_3CHOH^* + * \rightleftharpoons CH_3CHO^* + H^*$	6.8310×10^{20}	1.0	0.4
R107	$CH_3CO^* + H^* \rightleftharpoons CH_3COH^* + *$	2.2542×10^{21}	1.0	123.0
R108	$CH_2CH_2OH^* + 2^* \rightleftharpoons CH_2CH_2O^{**} + H^*$	4.2513×10^{28}	1.0	117.2
R109	$CH_2CHO^* + H^* \rightleftharpoons CH_2CHOH^* + *$	2.7599×10^{21}	1.0	98.3
R110	$CH_2COH^* + * \rightleftharpoons CH_2CO^* + H^*$	1.2211×10^{21}	1.0	75.3
R111	$CHCH_2O^{**} + H^* \rightleftharpoons CHCH_2OH^* + 2^*$	2.2926×10^{21}	1.0	136.8
R112	$CHCHOH^* + * \rightleftharpoons CHCHO^* + H^*$	1.1422×10^{21}	1.0	59.0
R113	$CHCOH^* + * \rightleftharpoons CHCO^* + H^*$	2.3815×10^{21}	1.0	97.9

Table 6.1. Continued.

	Reaction	Sticking coefficient $S°_j$ [unitless] or pre-exponential $A_{f,j}$ [mol, cm, s]	Temperature exponent, β_j	Activation energy $Ea_{f,j}$ [kJ/mol]
R114	$CCH_2O^{**} + H^* \rightleftharpoons CCH_2OH^* + 2^*$	1.0376×10^{19}	1.0	90.8
R115	$CCHOH^* + ^* \rightleftharpoons CCHO^* + H^*$	2.3815×10^{21}	1.0	107.9
R116	$CCOH^{**} \rightleftharpoons CCO^* + H^*$	4.3994×10^{12}	1.0	108.8
Carbon-oxygen bond cleavage reactions				
R117	$CH_3CH_2OH^* + ^* \rightleftharpoons CH_3CH_2^* + OH^*$	3.1879×10^{21}	1.0	143.9
R118	$CH_3CHOH^* + ^* \rightleftharpoons CH_3CH^* + OH^*$	5.1515×10^{20}	1.0	37.7
R119	$CH_3COH^* + ^* \rightleftharpoons CH_3C^* + OH^*$	2.7951×10^{21}	1.0	59.8
R120	$CH_2CH_2OH^* + 2^* \rightleftharpoons CH_2CH_2^{**} + OH^*$	1.0689×10^{29}	1.0	67.4
R121	$CH_2CHOH^* \rightleftharpoons CH_2CH^* + OH^*$	8.0871×10^{12}	1.0	72.8
R122	$CH_2COH^{**} \rightleftharpoons CH_2C^* + OH^*$	6.2281×10^{12}	1.0	77.8
R123	$CHCH_2OH^* + ^* \rightleftharpoons CH_2CH^* + OH^*$	2.7483×10^{21}	1.0	110.0
R124	$CHCHOH^* + ^* \rightleftharpoons CHCH^* + OH^*$	6.2774×10^{20}	1.0	78.7
Carbon-oxygen bond cleavage reactions				
R125	$CHC^* + OH^* \rightleftharpoons CHCOH^* + ^*$	1.2444×10^{21}	1.0	118.8
R126	$CCH_2OH^* + ^* \rightleftharpoons CH_2C^* + OH^*$	1.9798×10^{21}	1.0	126.8
R127	$CHC^* + OH^* \rightleftharpoons CCHOH^* + ^*$	1.2444×10^{21}	1.0	144.8
R128	$CC^* + OH^* \rightleftharpoons CCOH^* + ^*$	3.4343×10^{21}	1.0	139.3
R129	$CH_3CH_2O^* + ^* \rightleftharpoons CH_3CH_2^* + O^*$	1.1140×10^{21}	1.0	155.2
R130	$CH_3CHO^* + ^* \rightleftharpoons CH_3CH^* + O^*$	6.3617×10^{20}	1.0	170.3
R131	$CH_3CO^* + ^* \rightleftharpoons CH_3C^* + O^*$	1.1937×10^{22} (1.1937×10^{21})	1.0	118.4
R132	$CH_2CH_2^* + O^* \rightleftharpoons CH_2CH_2O^* + ^*$	2.0994×10^{21}	1.0	120.1
R133	$CH_2CH^* + O^* \rightleftharpoons CH_2CHO^{**}$	3.0986×10^{21}	1.0	144.8
R134	$CH_2CO^{**} \rightleftharpoons CH_2C^* + O^*$	4.3025×10^{12}	1.0	87.4

Table 6.1. Continued.

	Reaction	Sticking coefficient $S°_j$ [unitless] or pre-exponential $A_{f,j}$ [mol, cm, s]	Temperature exponent, β_j	Activation energy $Ea_{f,j}$ [kJ/mol]
R135	$CHCH_2O^{**} \rightleftharpoons CH_2CH^* + O^*$	3.5125×10^{12}	1.0	94.6
R136	$CHCHO^* + 2^* \rightleftharpoons CHCH^{**} + O^*$	4.6361×10^{20}	1.0	125.9
R137	$CHC^* + O^* \rightleftharpoons CHCO^* + ^*$	3.5132×10^{21}	1.0	128.9
R138	$CCH_2O^{**} \rightleftharpoons CH_2C^* + O^*$	1.1452×10^{10}	1.0	52.3
R139	$CHC^* + O^* \rightleftharpoons CCHO^* + ^*$	3.5132×10^{21}	1.0	152.7
R140	$CC^{**} + O^* \rightleftharpoons CCO^* + 2^*$	6.0865×10^{21}	1.0	143.9
Carbon-carbon bond cleavage reactions				
R141	$CH_3CH_2OH^* + ^* \rightleftharpoons CH_3^* + CH_2OH^*$	1.3903×10^{21} (6.3903×10^{21})	1.0	116.3
R142	$CH_3CHOH^* + ^* \rightleftharpoons CH_3^* + CHOH^*$	2.2407×10^{20}	1.0	77.0
R143	$CH_3COH^* + ^* \rightleftharpoons CH_3^* + COH^*$	7.1869×10^{20} (3.1869×10^{21})	1.0	114.2 (75.7)
R144	$CH_2^* + CH_2OH^* \rightleftharpoons CH_2CH_2OH^* + ^*$	1.7409×10^{21}	1.0	92.5
R145	$CH_2^* + CHOH^* \rightleftharpoons CH_2CHOH^{**}$	8.0554×10^{21}	1.0	105.0
R146	$CH_2COH^{**} \rightleftharpoons CH_2^* + COH^*$	1.5324×10^{13}	1.0	75.7
R147	$CH^* + CH_2OH^* \rightleftharpoons CHCH_2OH^* + ^*$	8.4365×10^{20}	1.0	104.6
R148	$CH^* + CHOH^* \rightleftharpoons CHCHOH^*$	1.0146×10^{22}	1.0	103.8
R149	$CHCOH^{**} \rightleftharpoons CH^* + COH^*$	2.1544×10^{13}	1.0	98.3
R150	$C^* + CH_2OH^* \rightleftharpoons CCH_2OH^* + ^*$	2.2927×10^{21}	1.0	15.9
R151	$C^* + CHOH^* \rightleftharpoons CCHOH^{**}$	1.4566×10^{22}	1.0	36.0
R152	$CCOH^{**} \rightleftharpoons C^* + COH^*$	7.0322×10^{12}	1.0	112.1
R153	$CH_3CH_2O^* + ^* \rightleftharpoons CH_3^* + CH_2O^*$	1.8732×10^{20} (1.8732×10^{21})	1.0	155.2 (27.9)
R154	$CH_3CHO^* + ^* \rightleftharpoons CH_3^* + CHO^*$	5.6588×10^{21}	1.0	116.7
R155	$CH_3CO^* + ^* \rightleftharpoons CH_3^* + CO^*$	1.0218×10^{21}	1.0	106.7 (68.2)
R156	$CH_2CH_2O^{**} = CH_2^* + CH_2O^*$	4.2572×10^{15} (4.2572×10^{13})	1.0	235.1 (114.2)

Table 6.1. Continued.

	Reaction	Sticking coefficient $S°_j$ [unitless] or pre-exponential $A_{f,j}$ [mol, cm, s]	Temperature exponent, β_j	Activation energy $Ea_{f,j}$ [kJ/mol]
Carbon-carbon bond cleavage reactions				
R157	$CH_2^* + CHO^* \rightleftharpoons CH_2CHO^{**}$	7.5337×10^{20}	1.0	91.6
R158	$CH_2CO^{**} \rightleftharpoons CH_2^* + CO^*$	7.9481×10^{11} (7.9481×10^{12})	1.0	59.4 (20.9)
R159	$CHCH_2O^{**} \rightleftharpoons CH^* + CH_2O^*$	5.6583×10^{12}	1.0	86.2
R160	$CH^* + CHO^* \rightleftharpoons CHCHO^{**}$	6.7180×10^{20}	1.0	111.7
R161	$CHCO^{**} \rightleftharpoons CH^* + CO^*$	5.7296×10^{11} (5.7296×10^{12})	1.0	108.8 (20.1)
R162	$C^* + CH_2O^* \rightleftharpoons CCH_2O^{**}$	1.3904×10^{24}	1.0	89.5
R163	$C^* + CHO^* \rightleftharpoons CCHO^{**}$	2.0108×10^{21}	1.0	82.4
R164	$CCO^* + * \rightleftharpoons C^* + CO^*$	1.0124×10^{21}	1.0	40.6
Acetic and formic acids decomposition reactions				
Adsorption/desorption				
R165	$CH_3COOH + 2^* \rightleftharpoons CH_3COOH^*$	0.50	0.0	0.0
R166	$HCOOH + * \rightleftharpoons HCOOH^*$	0.50	0.0	0.0
Carbon-oxygen bond cleavage reactions				
R167	$H_2COO^{**} \rightleftharpoons CH_2O^* + O^*$	2.9342×10^{12}	1.0	74.9
R168	$CH_2O^* + OH^* \rightleftharpoons H_2COOH^{**}$	8.0575×10^{20}	1.0	140.2
R169	$HCOOH^* + * \rightleftharpoons CHO^* + OH^*$	7.6410×10^{21}	1.0	92.5
R170	$C(OH)_2^* + * \rightleftharpoons COH^* + OH^*$	2.0564×10^{19}	1.0	66.1
R171	$HC(OH)_2^* + * \rightleftharpoons CHOH^* + OH^*$	3.3860×10^{18}	1.0	77.0
R172	$CCOO^* + * \rightleftharpoons CCO^* + O^*$	7.2518×10^{21}	1.0	131.8
R173	$CCO^* + OH^* \rightleftharpoons CCOOH^* + *$	3.9052×10^{21}	1.0	141.8
R174	$CH_2CO^{**} + O^* \rightleftharpoons CH_2COO^{**} + *$	5.0436×10^{21}	1.0	131.4
R175	$CH_2CO^{**} + OH^* \rightleftharpoons CH_2COOH^{**} + *$	1.1712×10^{21}	1.0	112.1

Table 6.1. Continued.

	Reaction	Sticking coefficient $S°_j$ [unitless] or pre-exponential $A_{f,j}$ [mol, cm, s]	Temperature exponent, β_j	Activation energy $Ea_{f,j}$ [kJ/mol]
R176	$CH_3CO^* + O^* \rightleftharpoons CH_3COO^{**}$	1.6683×10^{21}	1.0	123.0
R177	$CH_3CO^* + OH^* \rightleftharpoons CH_3COOH^{**}$	1.9318×10^{23}	1.0	111.3
R178	$CHCO^{**} + O^* \rightleftharpoons CHCOO^{**} + *$	6.6940×10^{21}	1.0	127.6
R179	$CHCO^{**} + OH^* \rightleftharpoons CHCOOH^* + 2*$	6.4253×10^{29}	1.0	135.1
Carbon-hydrogen bond cleavage reactions				
R180	$H_2COOH^{**} \rightleftharpoons HCOOH^* + H^*$	8.8146×10^{12}	1.0	68.6
R181	$H_2COO^* + * \rightleftharpoons HCOO^* + H^*$	2.9965×10^{21}	1.0	0.0
R182	$HCOOH^* + * \rightleftharpoons COOH^* + H^*$	3.8942×10^{21}	1.0	36.0
R183	$HC(OH)_2^* + * \rightleftharpoons C(OH)_2^* + H^*$	2.9648×10^{21}	1.0	44.8
R184	$CHCOO^{**} \rightleftharpoons CCOO^* + H^*$	3.9029×10^{11}	1.0	98.3
R185	$CHCOOH^* + * \rightleftharpoons CCOOH^* + H^*$	2.9867×10^{21}	1.0	82.0
R186	$CHCOO^{**} + H^* \rightleftharpoons CH_2COO^{**} + *$	1.4908×10^{21}	1.0	119.7
R187	$CHCOOH^* + H^* \rightleftharpoons CH_2COOH^{**}$	1.2257×10^{21}	1.0	111.7
R188	$CH_2COO^{**} + H^* \rightleftharpoons CH_3COO^{**} + *$	1.2257×10^{21}	1.0	37.7
R189	$CH_3COOH^{**} + * \rightleftharpoons CH_2COOH^{**} + H^*$	7.2853×10^{18}	1.0	66.1
Oxygen-hydrogen bond cleavage reactions				
R190	$H_2COO^{**} + H^* \rightleftharpoons H_2COOH^{**} + *$	9.5242×10^{20}	1.0	94.6
R191	$HCOOH^* + 2* \rightleftharpoons HCOO^{**} + H^*$	1.5893×10^{30}	1.0	13.4
R192	$C(OH)_2^* + * \rightleftharpoons COOH^* + H^*$	1.0041×10^{19}	1.0	26.8
R193	$HC(OH)_2^* + * \rightleftharpoons HCOOH^* + H^*$	7.6446×10^{18}	1.0	21.8
R194	$CCOOH^* + * \rightleftharpoons CCOO^* + H^*$	1.3263×10^{19} (1.3263×10^{20})	1.0	179.1 (158.2)
R195	$CHCOO^{**} + H^* \rightleftharpoons CHCOOH^* + 2*$	1.4908×10^{21}	1.0	122.6
R196	$CH_2COOH^{**} + * \rightleftharpoons CH_2COO^{**} + H^*$	3.6326×10^{21}	1.0	136.0

Table 6.1. Continued.

	Reaction	Sticking coefficient $S°_j$ [unitless] or pre-exponential $A_{f,j}$ [mol, cm, s]	Temperature exponent, β_j	Activation energy $Ea_{f,j}$ [kJ/mol]
R197	$CH_3COOH^{**} + * \rightleftharpoons CH_3COO^{**} + H^*$	7.2853×10^{18}	1.0	0.0
Carbon-carbon bond cleavage reactions				
R198	$CCOO^* + 2^* \rightleftharpoons C^* + CO_2^*$	2.9694×10^{32}	1.0	111.3
R199	$C^* + COOH^* \rightleftharpoons CCOOH^* + *$	5.0036×10^{21}	1.0	91.2
R200	$CHCOO^{**} + * \rightleftharpoons CH^* + CO_2^{**}$	1.5415×10^{23}	1.0	65.3
R201	$CH^* + COOH^* \rightleftharpoons CHCOOH^* + *$	1.2595×10^{21}	1.0	116.3
R202	$CH_2COO^{**} + * \rightleftharpoons CH_2^* + CO_2^{**}$	2.8381×10^{23}	1.0	105.9
R203	$CH_2^* + COOH^* \rightleftharpoons CH_2COOH^{**}$	5.6246×10^{20}	1.0	110.5
R204	$CH_3^* + CO_2^{**} \rightleftharpoons CH_3COO^{**} + *$	1.3718×10^{19}	1.0	29.7
R205	$CH_3COOH^{**} \rightleftharpoons CH_3^* + COOH^*$	5.3432×10^{10}	1.0	92.0

Notes: In the reaction description, the asterisk (*) denotes the number of surface sites occupied by the surface species. All reactions were firstly written in the exothermic direction. Then, based on the reaction path analysis, sensitivity analysis and partial equilibrium analysis, some reactions were inverted according to the procedure explained in the text. The forward reaction rate constant is governed by the modified Arrhenius equation Eq. (2.3) for surface reactions and by Eq. (2.7) for adsorption. Pre-exponential factors are written in concentration units. Values in parenthesis after pre-exponential factors and activation energies of the reactions that were tuned to the experimental data are the original values predicted by Eq. (2.16), DFT or BEP correlations.

Table 6.2. Surface thermochemistry of the adsorbates on Ni (111) surface.

Species	H_i^0 [kJ/mol]	Coverage dependency, $\alpha_{i,j}$ [kJ/mol]	Temperature Dependency, δ_i	S_i^0 [J/mol.K]	H_{gas}^0 [kJ/mol]
water-gas shift intermediates					
H_2O*	-293.8	$63\theta_{CO}+36\theta_{H}+71\theta_{CHCH}+63\theta_{CCOOH}+52\theta_{CH2CH2O}+118\theta_{CH}+106\theta_{CH3C}+68\theta_{CH3CH2O}$	2.5	41.8	-241.8
OH*	-262.3	$63\theta_{CO}+42\theta_{H}+51\theta_{CHCH}+133\theta_{CCOOH}$	2	37.6	37.3
O*	-221.7	$150\theta_{CO}+63\theta_{H}+60\theta_{CHCH}+42\theta_{CCOOH}+185\theta_{O}$	1.5	16.8	249.1
H*	-53.9	$19\theta_{CO}+4\theta_{H}+21\theta_{CHCH}+21\theta_{CCOOH}$	1.5	5.6	211.8
CO*	-240.5	$152\theta_{CO}+19\theta_{H}+88\theta_{CHCH}+42\theta_{CCOOH}$	2	44.9	-110.5
COH*	-203.1		2	70.5	218.1
COOH*	-434.5	$63\theta_{CO}+42\theta_{CO}$	3	90.7	-181.3
CHO*	-185.0		2.5	69.8	42.3
HCOO**	-458.8		3	93.7	-129.7
CO_2**	-370.6		1.5	153.6	-393.4
Ethanol intermediates					
CH_3CH_2OH*	-335.7	$17\theta_{H}+36\theta_{CHCH}+42\theta_{CCOOH}$	2.5	118.3	-235.0
CH_2CH_2OH*	-234.7		2.5	134.7	-25.8
$CHCH_2OH$*	-197.7		2.5	112.8	
CCH_2OH*	-191.4		2.5	106.7	
CH_3CHOH*	-195.3		2.5	126.5	-54.0
CH_2CHOH**	-184.6		3	112.8	-29.8
CHCHOH**	-159.2		3	106.7	
CCHOH**	-131.2		3	90.0	
CH_3COH*	-221.3	$17\theta_{H}+54\theta_{CHCH}+136\theta_{CCOOH}$	2.5	112.5	
CH_2COH**	-160.6		3	105.6	
CHCOH**	-159.2		3	90.0	22.3
CCOH**	-80.3		2.5	85.8	

Table 6.2. Continued.

Species	H_i^0 [kJ/mol]	Coverage dependency, $\alpha_{i,j}$ [kJ/mol]	Temperature Dependency, δ_i	S_i^0 [J/mol.K]	H_{gas}^0 [kJ/mol]
CH_3CH_2O*	-307.7	$63\theta_H+92\theta_{CHCH}+63\theta_{CCOOH}$	2.5	115.0	-13.6
CH_2CH_2O**	-183.9	$17\theta_H+75\theta_{CHCH}+106\theta_{CCOOH}+58\theta_{CH2CH2O}$	3	82.2	164.5
$CHCH_2O$**	-135.0		3	105.8	
CCH_2O**	-94.1		3	189.4	
acetaldehyde intermediates					
CH_3CHO*	-246.7	$17\theta_H+71\theta_{CHCH}+42\theta_{CCOOH}$	2.5	102.2	-166.2
CH_2CHO**	-211.7		3	102.7	3.0
CHCHO**	-165.0		3	90.9	
CCHO**	-98.8		3	86.4	
CH_3CO*	-255.7	$17\theta_H+49\theta_{CHCH}+127\theta_{CCOOH}$	2.5	105.8	-10.3
CH_2CO**	-147.5	$17\theta_H+40\theta_{CHCH}+42\theta_{CCOOH}$	3	90.9	-48.6
CHCO**	-124.4	$17\theta_H+52\theta_{CHCH}+84\theta_{CCOOH}$	2.5	86.4	178.2
CCO*	-51.2	$17\theta_H+59\theta_{CHCH}+148\theta_{CCOOH}$	2	74.6	385.7
Ethane intermediates					
CH_3CH_3**	-131.9		3	169.7	-83.9
CH_3CH_2*	-69.9		2.5	87.5	80.7
CH_3CH*	-17.7		2.5	65.5	
CH_3C*	-42.8	$17\theta_H+65\theta_{CHCH}+161\theta_{CCOOH}$	2.5	79.5	
CH_2CH_2**	-34.4		3	65.5	52.6
CH_2CH*	34.1		2.5	79.5	296.6
CH_2C*	44.6	$17\theta_H+57\theta_{CHCH}+144\theta_{CCOOH}$	2.5	68.0	414.5
CHCH**	45.3	$33\theta_H+59\theta_{CHCH}+21\theta_{CCOOH}$	2.5	48.9	289.1
CHC**	153.0		2.5	61.1	568.1
CC**	224.1		2.5	40.1	826.8

Table 6.2. Continued.

Species	H_i^0 [kJ/mol]	Coverage dependency, $\alpha_{i,j}$ [kJ/mol]	Temperature Dependency, δ_i	S_i^0 [J/mol.K]	H_{gas}^0 [kJ/mol]
acetic and formic acid intermediates					
CH_3COOH^{**}	-469.9		2	218.5	-432.3
CH_2COOH^{**}	-439.7		3	118.7	
$CHCOOH^*$	-357.5		2.5	122.2	
$CCOOH^*$	-338.1	$42\theta_H+62\theta_{CHCH}+42\theta_{CCOOH}$	2.5	122.4	
CH_3COO^{**}	-521.0		3	118.7	-192.8
CH_2COO^{**}	-360.8		3	122.2	
$CHCOO^{**}$	-297.0	$63\theta_H+46\theta_{CHCH}+121\theta_{CCOOH}$	3	122.4	
$CCOO^*$	-249.8		2.5	70.9	
H_2COOH^{**}	-445.7		3	85.8	
$HCOOH^*$	-429.7		2.5	86.0	-378.6
$HC(OH)_2^*$	-399.6		2	185.0	
$C(OH)_2^*$	-404.9		2	185.1	
H_2COO^{**}	-344.7		3	93.4	
methanol intermediates					
CH_3OH^*	-269.6		2.5	84.2	-201.0
CH_2OH^*	-214.9		2.5	87.9	-17.2
$CHOH^*$	-176.7		2.5	40.4	123.0
CH_3O^*	-250.6		2.5	78.5	21.1
CH_2O^*	-184.6		2.5	64.1	-108.7
methane intermediates					
CH_3^*	-62.8	$90\theta_H+44\theta_{CHCH}+118\theta_{CCOOH}$	2.5	48.8	146.7
CH_2^*	-1.3		2.5	50.1	391.1
CH^*	21.4	$145\theta_H+72\theta_{CHCH}$	2	40.1	596.1
C^*	117.2		1.5	17.4	716.5

Notes: Inputs are the experimental heat of adsorption for species CO (Stuckless et al., 1993), H_2O (Schulze et al., 1995) and O (Stuckless et al., 1997). Heat of adsorption are calculated according to procedure presented in section 2.5 (Mhadeshwar et al., 2003; Blaylock et al., 2009; Catapan et al., to be published). The values are valid at 298 K. Temperature dependence is related to the heat of adsorption and is approximated as $\left(\Delta H_{ads,i}(T_0) - \Delta H_{ads,i}(T)\right)/R\Delta T$, derived from statistical thermodynamic as explained in details in (Mhadeshwar et al., 2003). Entropy on surface is calculated according to Eq. (2.28. Values for H^0_{gas} were taken from the Burcat's database (Goos et al., 2011).

Table 6.3 shows a comparison between the DFT-predicted and experimental corrected heats of adsorption of closed shell adsorbates. Differences are in general lower than 40 kJ/mol (0.4 eV) which is accepted for energy correction in microkinetic models (Salciccioli, Chen and Vlachos, 2011). Only heats of adsorption of CO and CH_3CH_2OH have higher discrepancies. Difference in CO is enhanced by the use of PBE functional in the DFT calculation and on CH_3CH_2OH is thought to be due to the use of a 2x2 unit cell. The origin and the implications of such differences are discussed in details in section 2.5. Surface enthalpy is considered to be affected by the coverage effects. The coverage dependency column stands for the values tuned to represent experimental data. Hierarquical assessment of the coverage parameters will be explained later in this text. The temperature dependency of the heat of adsorption is calculated based on the approach introduced by Mhadeshwar and Vlachos (Mhadeshwar et al., 2003) which takes into account the degrees of freedom lost upon adsorption by a statistical thermodynamic treatment. The entropy of each surface species (S_i^0) is calculated based on method introduced by Santiago *et al.* (Santiago et al., 2000).

Table 6.3. Heat of adsorption of the main species on Ni (111) surface. The column "corrected" stands for the thermodynamic corrected data as explained in the text. Inputs are the values for H_2O, O and CO.

Species	DFT-predicted [kJ/mol]	Corrected [kJ/mol]
H_2O	-45.0	-52.0
O	-464.1	-470.8
H	-265.7	-265.7
CO	-201.9	-130.0
CO_2	-9.0	22.9
CH_3CH_2OH	-51.5	-100.8
CH_3CHO	-61.9	-80.5
CH_3CH_3	-12.4	-48.0
CH_2CH_2	-91.0	-86.9
CHCH	-253.7	-243.8
CH_3COOH	-12.7	-37.6
HCOOH	-39.9	-51.1
CH_3OH	-32.6	-68.6
CH_4	-9.7	-34.3

This semi-empirical methodology for surface thermochemistry estimation has two advantages. First, it offers a great reduction in the time demanded to compute the thermochemistry in comparison with methods based on full statistical thermodynamic treatments, *e.g.*, in the work of Blaylock *et al.* (Blaylock et al., 2009), and second, the surface thermochemistry is based on the gas-phase properties, which are calculated using high level *ab initio* methods. However, a problem that arises from this methodology is that gas-phase properties are not available for all species usually used in surface mechanisms. For example, the last column of the Table 6.2 shows the gas-phase enthalpy for those species that have thermodynamic properties available in the Burcat's database. For the remaining species, the thermodynamic properties are assumed as that of a species with similar molecular weight. Although the species may have very different enthalpy of reference at 298 K, this will not influence the surface enthalpy since it is based on the DFT-predicted heat of the surface reactions instead of heat of adsorption.

6.3. STRUCTURING THE MECHANISM IN A SYSTEM-DRIVEN WAY AND HIERARCHICAL ASSESSMENT OF THE KINETIC PARAMETERS

The methodology used for assessing the kinetic parameters is hierarquical and it is composed of three main parts. In the first part, the reactions were written in such direction that the forward reaction rate controls the net rate, similarly to the method applied in the WGS mechanism. Secondly, the important coverage effects were included in the model. These two steps were repeated until the mechanism reproduced the macroscopic trends observed in the experimental data. Finally, the kinetic parameters were tuned to a better representation of the experimental data. Below, each of these steps is explained in details.

In order to structure the mechanism, first, all reactions are written in the exothermic direction, according to the thermochemistry at 298 K. Then, with the aid of the reaction path analysis (RPA) and partial equilibrium analysis (PE), the reactions are written in the direction that they are favored. This is a simple task for small mechanisms such as the WGS mechanism reported in chapter 4. However, it is not trivial to find the direction of each individual reaction in large mechanisms as the one analyzed here.

Thus, this procedure was applied only for reactions that potentially compose the main flux based on the DFT results reported in chapter 5. For example, based on the results of chapter 5, the reaction involving CH_3CH_2OH, CH_3CH_2O, CH_3CHO, CH_3CO, CH_2CO and CHCO were written in a direct way, *e.g.*, $CH_3CO \rightleftharpoons CH_3 + CO$ and $CH_3CO + O \rightleftharpoons CH_3COO$. Additionally, the direction of the important reactions was checked by keeping the partial equilibrium ratio (PE) higher than 0.5. Reaction path analysis (RPA) was used to find the important reactions.

After structuring the mechanism, the choice of which lateral interaction parameter must be used in the microkinetic model is based on sensitivity analysis of the surface intermediates (MISI) and on the most abundant surface intermediates (MASI) in a procedure similar to that applied in chapter 4. The calculation of all possible interaction parameters *a priori* is a very time demanding task and hierarquical procedures were developed to address this issue (Salciccioli, Stamatakis, Caratzoulas and Vlachos, 2011). One methodology successfully used in the development of the microkinetic models is to include an order of magnitude of the parameters and fit them to the experimental data (Salciccioli, Chen and Vlachos, 2011). Here, the estimate of the parameters was made based on DFT calculations for WGS pair interaction adsorbates predicted in chapter 4. This was done by plotting the binding energy of the two adsorbates at the same slab against the sum of the individual binding energies of the adsorbates on different slabs, as shown in Figure 6.1. Linear correlation is observed. Applying this linear regression to other pair interaction adsorbates, one can estimate the combined binding energy of two adsorbates based in the individual binding energies. Then, the lateral interaction parameter is estimated according to the procedure described in the section 2.4. The lateral interaction parameters shown in Table 6.2 are those tuned to the experimental data.

Finally, when all important parameters are included in the model, the sensitivity analysis indicates which one must be tuned to better representation of the experimental data. In this step of the methodology, the activation energy, the pre-exponential and the lateral interaction parameters were allowed to relax within the error usually found in microkinetic models. In terms of activations energies predicted by DFT, there are several errors that may contribute to the deviation, *e.g.*, use of PBE functional (estimated

around 40 kJ/mol (0.4 eV) (Paier et al., 2005), use of GGA scheme (~ 20 kJ/mol (0.2 eV) (Studt et al., 2008)), lateral interaction due to the use of a 2x2 slab (~20 kJ/mol (0.2 eV) (Chen and Vlachos, 2010b)). Other contributions are in general smaller than 10 kJ/mol (0.1 eV) (BSSE, convergence in terms of k-points, use of DZP basis set) as reported in the chapter 3. The standard deviations of the BEPs used here are in general smaller than the highest DFT error. Regarding to the pre-exponentials, it is worth to remember that they are calculated by Eq. (2.16), which is an approximation of the pre-exponential calculated via Transition State Theory and carry uncertainties in the estimation of the entropy of surface species. An analysis revealed that an error of 40 J/mol.K in the entropy of the surface reaction, produce a deviation of one order of magnitude in the pre-exponential. Thus, for the purposes of parameter adjustment, the activation energies and the pre-exponential were allowed to relax within an error of 0.4 eV and one order of magnitude, respectively. The errors in the lateral interaction parameters are discussed later in this text. The forward kinetic parameters of the sensitive reactions (5, 6, 8, 20, 27, 58, 59, 61, 62, 63, 71, 72, 88, 89, 131, 141, 143, 153, 155, 156, 158, 161 and 193) were adjusted within the aforementioned errors.

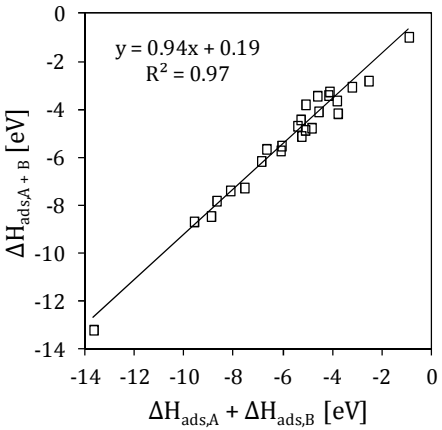

Figure 6.1. Binding energy of the two adsorbates at the same slab ($\Delta H_{ads,A+B}$) against the sum of the individual binding energies of the adsorbates on different slabs ($\Delta H_{ads,A} + \Delta H_{ads,B}$).

6.4. RESULTS

6.4.1. Comparison of the Model Prediction to Experimental Data

Figure 6.2 to Figure 6.5 show the comparison between the model predictions and previously published results by Mas *et al.* (Mas, Baronetti, Amadeo and Laborde, 2008).

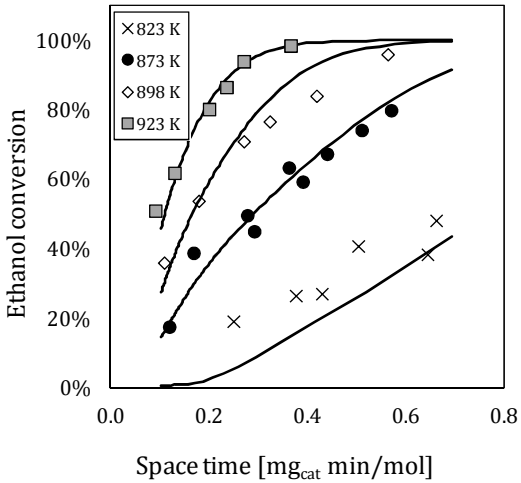

Figure 6.2. Comparison of the microkinetic model to published data of steam reforming of ethanol (Mas *et al.* (Mas, Baronetti, Amadeo and Laborde, 2008)). Measurements are under atmospheric pressure over Ni/Al_2O_3, inlet mole fractions are 0.016, 0.09 for C_2H_5OH and H_2O, respectively, balanced in Ar. Experimental conditions were tested by the author (Mas, Baronetti, Amadeo and Laborde, 2008) to verify negligible contributions of homogeneous phase reactions and absence of external and internal diffusion limitations.

The simulation inputs represent the experimental conditions. The catalyst loading was kept fixed during the simulation while the volumetric flow rate was varied in order to reproduce the range of space time analyzed in the experiment, *i.e.*, 1.2. to 6.8 mg min mol^{-1}. Simulations are performed in a plug flow reactor model under the SURFACE CHEMKIN framework with specific metallic area of 350

cm^{-1}. For example, an active area of 280 cm^{-1} was estimated based on: 1) the catalyst used by Mas *et al.* (Mas, Baronetti, Amadeo and Laborde, 2008) was made from a Ni(II)-Al(III) double hydroxide as a precursor. The stoichiometric composition of this material gives a Ni content of 70% (Titulaer et al., 1994); 2) the mean Ni particle diameter of 5 nm reported based on XRD analysis and Scherrer equation; 3) dispersion is considered as $1/d_{particle}$; 4) area of a binding site is 5.67 x 10^{-20} m^2 assuming four sites per a 2x2 slab of a Ni (111) and 5) assuming a loading of 0.044 mg.

Figure 6.2 shows that the model is capable of recovering qualitatively and quantitatively the conversions reported in all temperature and space time ranges analyzed. The model is capable of recovering the reaction order in relation to ethanol (Figure 6.3), water (Figure 6.4) and methane (Figure 6.5). Although the orders to ethanol and methane were compared only on one temperature (898 K), Figure 6.4 shows that the model recovered trends at different temperatures for different water mole fractions.

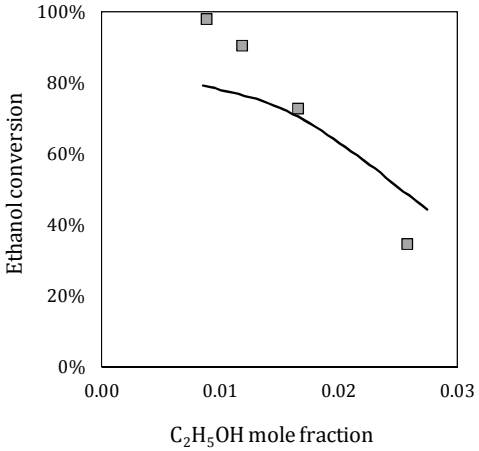

Figure 6.3. Comparison of the microkinetic model to published data of steam reforming of ethanol (Mas, Baronetti, Amadeo and Laborde, 2008) at 898 K. Same simulated reactor as in Figure 6.2.

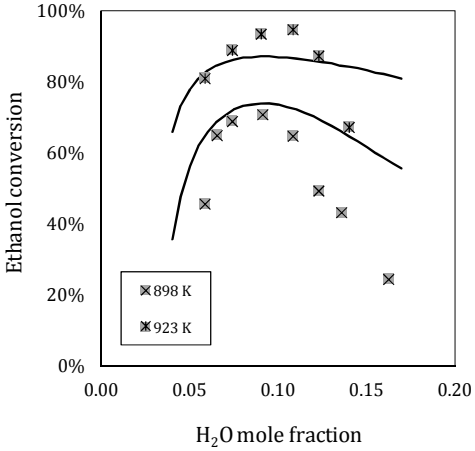

Figure 6.4. Comparison of the microkinetic model to published data of steam reforming of ethanol (Mas, Baronetti, Amadeo and Laborde, 2008) showing conversion achieves a maximum for the water/ethanol ratio of 5. Same simulated reactor as in Figure 6.2.

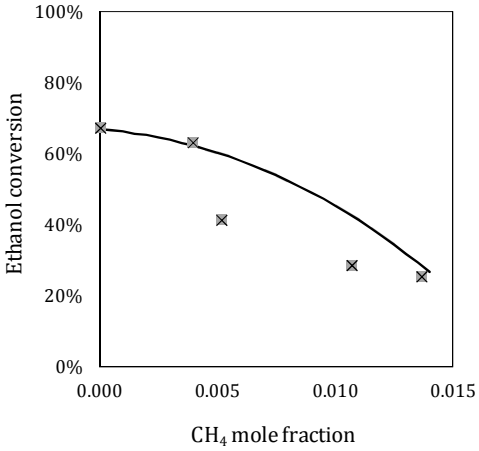

Figure 6.5. Comparison of the microkinetic model to published data of steam reforming of ethanol (Mas, Baronetti, Amadeo and Laborde, 2008) at 898 K showing ethanol conversion decreasing as methane mole fraction increases. Same simulated reactor as in Figure 6.2.

Figure 6.8 to Figure 6.8 shows the model prediction of the yield of H_2, CO and CO_2, respectively. Besides the fact that ethanol steam reforming is a complex system, with multiple potential by-products, the model is capable of predicting qualitatively the yield of these species. The model predicts a maximum mole fraction of 5 x 10^{-3} of CH_4 and less than 1 x 10^{-4} of C2 species. The values reported by Mas *et al.* (Mas, Baronetti, Amadeo and Laborde, 2008) are 3.2 x 10^{-4} of CH_4 and traces of C2 species.

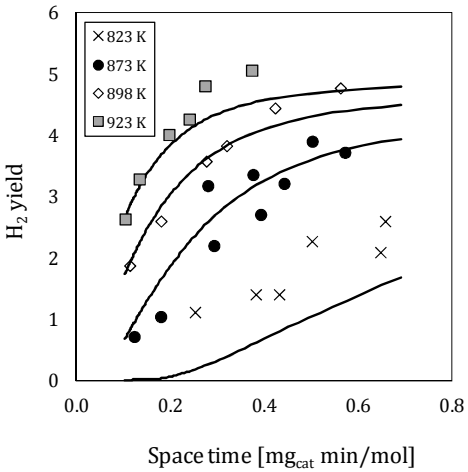

Figure 6.6. Yield H_2 calculated from the steam reforming of ethanol over Ni. Same simulated reactor as in Figure 6.2. Yield is defined as the molar flow rate of the species of interest over the total molar flow rate of ethanol.

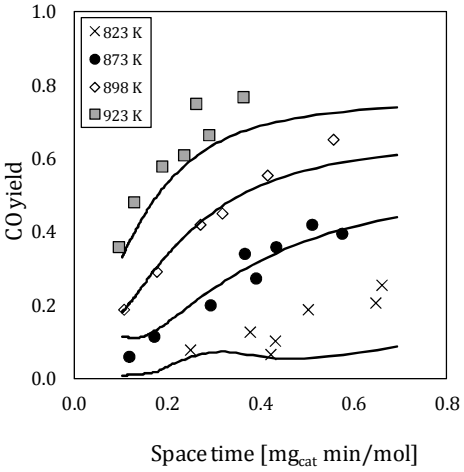

Figure 6.7. Yield of CO calculated from the steam reforming of ethanol over Ni. Same simulated reactor as in Figure 6.2.

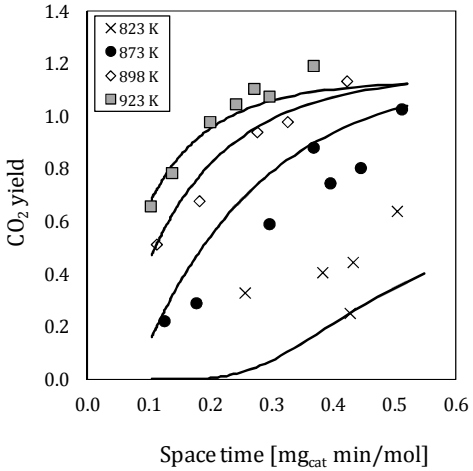

Figure 6.8. Yield of CO_2 calculated from the steam reforming of ethanol over Ni. Same simulated reactor as in Figure 6.2.

In the present model, the kinetics is dependent on the coverage of mainly CHCH and CCOOH species. The presence of these two groups is governed by the ratio water/ethanol in the feed. For example, Figure 6.9 shows the change in the surface population with

changes on the ethanol/water molar ratio for the same reaction conditions reported in Figure 6.4. Figure 6.4 shows that ethanol conversion achieves a maximum for an ethanol/water ratio close to 5 (H_2O mole fraction ~0.09). At the same ratio, Figure 6.9 shows that the surface is mostly free of these two surface species. Only H is populating the surface, however, the DFT calculations shows that atomic H interacts too weak with other surface species. This behavior denotes that the site occupation has two different regimes. In the low water concentration regime, the CHCH species populate the surface. As the concentration increases, CCOOH species populate the surface, decreasing the ethanol conversion.

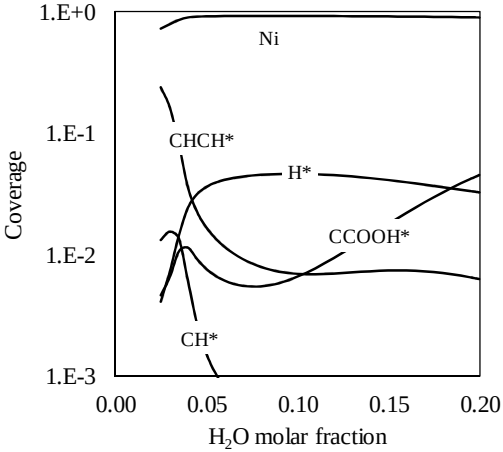

Figure 6.9. Coverage of the main species for the conditions presented in Figure 6.4.

The kinetics of the reaction is coverage dependent in the range of conditions analyzed. Figure 6.10 and Figure 6.11 shows the coverage of the main species along the reactor length. The formation of CHCH and CCOOH on the surface occurs on different residence times. At the conditions analyzed in the Figure 6.10, CHCH is formed in the first tenth of the reactor (see Figure 6.11 for details). As the residence time increases, CHCH is consumed and the formation of CCOOH, H and a small portion of CH occur. CHCH, CCOOH and CH are consumed along the reactor length. Although this behavior is general for the temperatures between 878 K and 923 K, the coverage of these species at the end of the reactor

decreases substantially as temperature increases as visualized in the Figure 6.12.

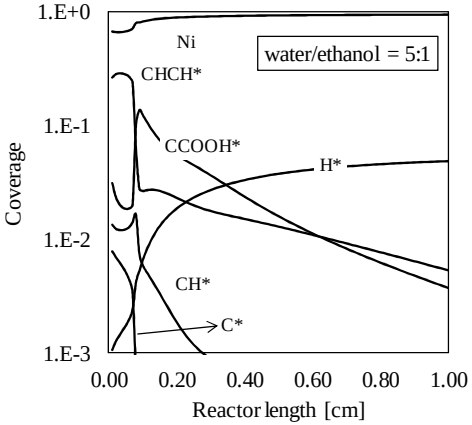

Figure 6.10. Coverage of the main species along the reactor length of 1 cm. Reaction conditions: space time = 0.27 mg_{cat} min / mol, temperature = 898 K and water/ethanol molar ratio = 5.4:1.

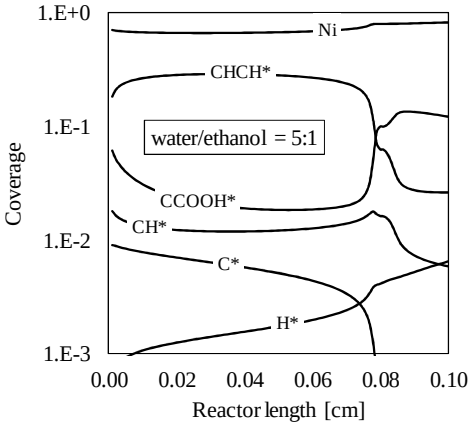

Figure 6.11. Coverage of the main species along the reactor length of 0.1 cm. Reaction conditions: space time = 0.27 mg_{cat} min / mol, temperature = 898 K and water/ethanol molar ratio = 5.4:1.

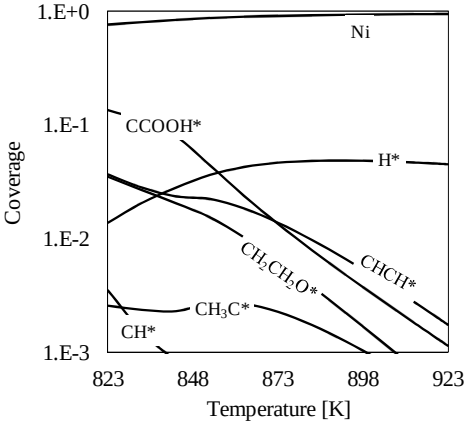

Figure 6.12. Coverage of the main species at the end of the reactor as a function of the temperature. Reaction conditions: space time = 0.27 mg_{cat} min / mol and water/ethanol molar ratio = 5.4:1.

The presence of the carboxylate group (CCOO) under adsorption of ethanol is reported by several groups (Yee et al., 1999; Deng et al., 1995; de Lima et al., 2008; Busca et al., 2009; Sim et al., 1996; Houtman et al., 1994; Davis and Barteau, 1988; Tingcheng, 2003). The carboxylate group is usually attributed to acetate species (CH_3COO). The more dehydrogenated form of the acetate group adsorbs in a "Y" configuration, instead of an inverse "Y" configuration usually reported for the acetate species. Nonetheless, for a validation of the presence of such species on the surface, it is needed to design an experiment operating in similar conditions than those used as the inputs in the microkinetic analysis.

6.4.2. Analysis of the Surface Reaction Mechanism Under High Temperature Steam Reforming of Ethanol

Figure 6.13 shows the main pathways for steam reforming of ethanol. The continuous line represent the main pathway, *i.e.*, which is responsible for the overall rate, and the dashed lines represent the secondary pathway which has a lower contribution to the overall rate. The first step in the ethanol dehydrogenation agrees

well with experimental findings reported by Gates *et al.* (Gates et al., 1986). The presence of the ethoxy species and the production of CH_3CHO from steam reforming of ethanol are well documented in the literature. Dehydrogenation follows via C^{α}-H of CH_3CHO, generating CH_3CO. These steps are in agreement with the conclusions of the DFT analysis.

The link between C2 and C1 chemistries occurs via two different pathways. First, C-C bond breaking of CH_3CO to CH_3 and CO is the responsible for 47% of the CH_3CO consumption. Second, C-O bond breaking of CH_3CO links the ethanol and ethane chemistries. Ethane intermediates participates actively of the kinetics, also being responsible for the formation of CHCH on the surface. In this pathway, the C-C bond breaking of CHCH links C2 and C1 chemistries. The role of water on the steam reforming of ethanol is also observed in Figure 6.13. Water is decomposed into atomic oxygen. Then, oxygen is responsible for oxidizing C1 species CH and CO. Oxidation of C2 species is secondary in the overall rate, however, it is responsible for the formation of CCOOH on the surface via CHCO + OH ⇌ CHCOOH ⇌ CCOOH + H. Oxidation of aldehydes to carboxylate species is described by Davis and Barteau (Davis and Barteau, 1988) on Pd (111) surface.

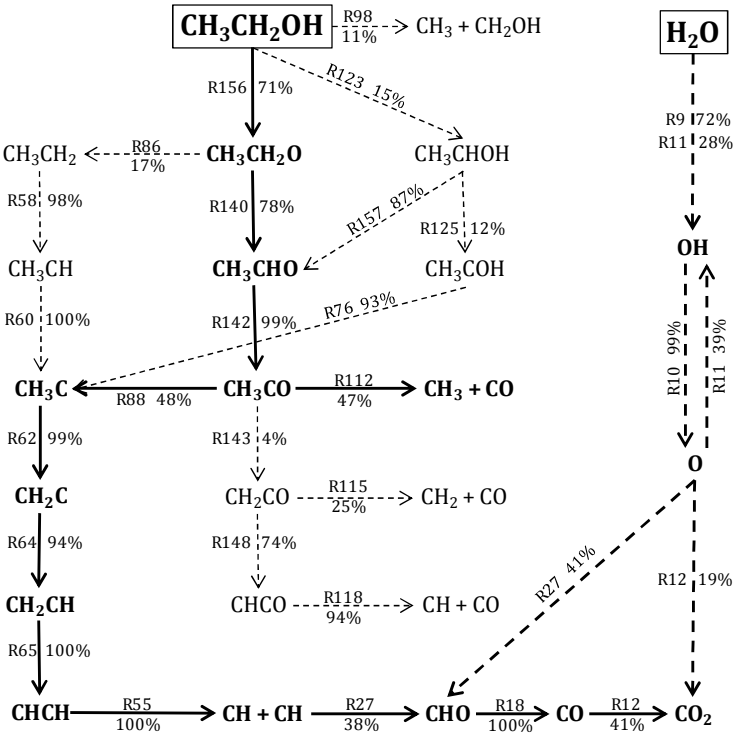

Figure 6.13. Surface reaction mechanism for high temperature (T = 898 K, water/ethanol molar ratio of 5.4 and space time of 0.27 mg_{cat} min / mol) steam reforming of ethanol on Ni catalyst.

6.4.3. Validation of the Kinetic Parameters

In order to verify if the values tuned to experimental data are consistent, the same parameters were predicted based on periodic DFT calculations. Table 6.4 shows a comparison among the lateral interaction parameters estimated by linear regression, DFT and fitted to experimental data. In general, linear regression method is adequate to represent experimental data and few adjustments were required. Nonetheless, one must look at the lateral interaction parameters as an approximation of real systems (Salciccioli, Chen and Vlachos, 2011; Podkolzin et al., 2002). The interaction energy may depend of several factors which include the orientation of the adsorbates on the surface and binding site as well as formation of

clusters, case of H_2O (Hodgson and Haq, 2009), which is not captured by periodic calculations. These parameters carry uncertainties and must be viewed as the trend of occurrence of a pairwise interaction. In the Table 6.4, it may be noted that DFT values are in general higher than the linear regression. This is thought to be due to the use of a 2x2 slab with C2 adsorbates. The only interaction that does not agree qualitatively is the interaction between CO + H_2O. However, for the purposes of quantitative prediction by the microkinetic model, the linear regression value is efficient.

Table 6.4. Comparison among the different methods to calculate the lateral interaction parameters.

Pair interaction	Linear regression [kJ/mol]	Tuned to exp. data [kJ/mol]	DFT-predicted [kJ/mol]
CO + CO	-83	-152	-152
H_2O + CO	-64	-63	45
CHCH + CHCH	-48	-59	-224
CCOOH + CCOOH	-154	-42	-281
CCOOH + CHCH	-62	-62	-73
CHCH + CCOOH	-62	-21	-73

As the methodology that is used here is based on tuning the kinetic parameters to the experimental data and assessing such parameters via sensitivity analysis, the surface mechanism reported here is only valid within the range of experimental conditions analyzed. To construct a mechanism valid on a more general region of interest, designing dedicated experiments to assess such regions is highly desirable, as for example, in the work of Prasad *et al.* (Prasad et al., 2009).

6.5. CONCLUSIONS

A microkinetic model was developed using the energetics predicted in chapter 5. A thermodynamic consistent surface thermochemistry database was developed based on semi-empirical methods. A hierarquical procedure was applied for the assessment of the kinetic parameters. The data reported by Mas *et al.* (Mas, Bergamini, Baronetti, Amadeo and Laborde, 2008) on steam reforming of ethanol on Ni/Al_2O_3 catalyst was chosen as a case

study to the applicability of the surface mechanism. A reaction path analysis of the high temperature steam reforming of ethanol was performed. The comparison of the model prediction and the experimental data shows that the model is capable of recovering the trends observed in the range of experimental conditions analyzed. The kinetics is coverage dependent in the range of conditions. Mostly, CHCH and CCOOH species populate the surface and they have a significant influence on the activity of this catalyst. The population of these two species is governed by the ratio of water/ethanol. For low water concentration, CHCH dominates the surface and for high water concentration CCOOH dominates the surface. The reaction path analysis shows that the ethanol steam reforming follows: $CH_3CH_2OH \rightarrow CH_3CH_2O \rightarrow CH_3CHO \rightarrow CH_3CO \rightarrow CH_3 + CO$ or $CH_3CO \rightarrow CH_3C \rightarrow CH_2C \rightarrow CH_2CH \rightarrow CHCH \rightarrow 2CH \rightarrow CHO \rightarrow CO \rightarrow CO_2$. Water is mostly decomposed into atomic oxygen, which is responsible for oxidizing C1 species CH and CO. At high water concentration, OH is responsible for the formation of CCOOH on the surface via $CHCO + OH \rightleftharpoons CHCOOH \rightleftharpoons CCOOH + H$. To the author's knowledge, this is the first time that a full analysis of the ethanol steam reforming mechanism on nickel catalyst is performed in a comprehensive and thermodynamic consistent way.

CHAPTER 7. CONCLUDING REMARKS AND SUGGESTIONS FOR FUTURE WORK

The present thesis consisted in the multiscale modeling and analysis of the steam reforming of ethanol and water-gas shift reaction on Ni catalysts. At the molecular level, *Density Functional Theory* (DFT) was applied to study the intermediates and reactions mostly on the flat surface of nickel (Ni (111)). The mean field assumption, *i.e.*, considering adsorbates and reactions homogenously distributed over the catalyst particle, has been evoked to develop a microkinetic model based on the most recent techniques and concepts. The main outcome of the microkinetic model developed here is a surface reaction mechanism composed of 205 elementary-like steps among 70 adsorbates to represent the steam reforming of ethanol and the WGS reactions over nickel. Specific conclusions were reported at the end of each chapter. Here, a series of concluding remarks and suggestions for future works are presented.

Chapter 3 reported results of the DFT analysis of the WGS reaction on flat (Ni (111)) and stepped (Ni (211)) surfaces. Results revealed that the sites play different roles in the reaction framework. For this reaction, the energetics on Ni (111) surface offers a reasonable representation of the activity of this catalyst. This conclusion is supported by the results of the microkinetic model reported in chapter 4. However, the DFT analysis also showed that the coke formation and methanation are enhanced in the stepped surface. This contrasts with the most accepted point of view in the analysis of heterogeneous catalyst at the molecular level in which the reaction is represented by one single active site. The combination of the information provided on both sites draws a more realistic picture of the reaction and such information is useful in the synthesis of more stable and active catalysts.

In the chapter 5, the energetics of the ethanol intermediates on Ni (111) were calculated via DFT. Based on these results, a series of *Brønsted-Evans-Polanyi* (BEP) correlations were proposed to calculate the activation energies of the elementary-like reactions. In the chapter 6, a microkinetic model for the steam reforming of ethanol developed over the energetics reported in the chapter 5 is presented. The model predictions compares well with the

experimental data reported in the literature for a range of experimental conditions. To achieve such consistency, the kinetic parameters, mostly the Arrhenius pre-exponentials and activation energies, had to be tuned to represent experimental data. This need for fitting may be a consequence of the uncertainties in the BEP correlations used to predict activation energies as well as it can be related to the presence of a second active site, not represented in the microkinetic model. The DFT analysis of a second site for ethanol reactions is suggested as future developments of the present thesis.

One point that must be emphasized here is that the results reported for the microkinetic model of the steam reforming of ethanol are valid under the specific experimental conditions, *i.e.*, temperature, pressure and reactants in the feed, as well as under the catalyst used. To build a mechanism valid on a wider region of interest, the design of dedicated experiments to assess such region is highly desired. Thus, it is evidenced the importance of a solid methodology for accessing the kinetic parameters of a microkinetic model in a thermodynamic and consistent way. Developing a microkinetic model as the one reported in chapters 4 and 6 for water-gas shift and steam reforming of ethanol, respectively, is a way to access a reliable kinetic model. The same methodology may be applied to develop a dedicated model to represent the kinetics of a specific Ni-based catalyst.

The development of kinetic models that comprise the entire framework of active sites and adsorbates, in particular for oxygenates, is object of intense research nowadays. Nevertheless, the importance of a microkinetic model based on a single active site arise from the use of such mechanism in the reactor design i) by using it directly in a in-house code, ii) by deriving global rate expressions to be used in CFD codes available commercially or iii) to analyze the interaction between gas-phase and heterogeneous chemistries in high temperature applications.

REFERENCES

Abild-Pedersen, F., Greeley, J., Studt, F., Rossmeisl, J., Munter, T. R., Moses, P. G., Skúlason, E., Bligaard, T. and Nørskov, J. K. (2007), 'Scaling properties of adsorption energies for hydrogen-containing molecules on transition-metal surfaces', *PHYSICAL REVIEW LETTERS* **99**(1), 016105.

Abild-Pedersen, F., Lytken, O., Engbæk, J., Nielsen, G., Chorkendorff, I. and Nørskov, J. K. (2005), 'Methane activation on Ni(1 1 1): Effects of poisons and step defects', *SURFACE SCIENCE* **590**(2-3), 127 – 137.

Akande, A., Aboudheir, A., Idem, R. and Dalai, A. (2006), 'Kinetic modeling of hydrogen production by the catalytic reforming of crude ethanol over a co-precipitated catalyst in a packed bed tubular reactor', *International Journal of Hydrogen Energy* **31**(12), 1707 – 1715.

Akpan, E., Akande, A., Aboudheir, A., Ibrahim, H. and Idem, R. (2007), 'Experimental, kinetic and 2-d reactor modeling for simulation of the production of hydrogen by the catalytic reforming of concentrated crude ethanol (CRCCE) over a Ni-based commercial catalyst in a packed-bed tubular reactor', *CHEMICAL ENGINEERING SCIENCE* **62**(12), 3112 – 3126.

Alavi, A., Hu, P., Deutsch, T., Silvestrelli, P. L. and Hutter, J. (1998), 'CO oxidation on Pt(111): An ab initio Density Functional Theory study', *PHYSICAL REVIEW LETTERS* **80**(16), 3650–3653.

Alcalá, R., Mavrikakis, M. and Dumesic, J. (2003), 'DFT studies for cleavage of C-C and C-O bonds in surface species derived from ethanol on Pt(111)', *Journal of Catalysis* **218**(1), 178 – 190.

Alcalá, R., Shabaker, J. W., Huber, G. W., Sanchez-Castillo, M. A. and Dumesic, J. A. (2005), 'Experimental and DFT studies of the conversion of ethanol and acetic acid on PtSn-based catalysts', *Journal of Physical Chemistry B* **109**(6), 2074–2085.

Aparicio, L. (1997), 'Transient isotopic studies and microkinetic modeling of methane reforming over nickel catalysts', *Journal of Catalysis* **165**(2), 262 – 274.

Beebe, Jr, T. P., Goodman, D. W., Kay, B. D. and Yates, Jr., J. T. (1987), 'Kinetics of the activated dissociative adsorption of methane on the low index planes of nickel single crystal surfaces', *Journal of Chemical Physics* **87**(4), 2305–2315.

Bengaard, H. S., Nørskov, J. K., Sehested, J., Clausen, B. S., Nielsen, L. P., Molenbroek, A. M. and Rostrup-Nielsen, J. R. (2002), 'Steam reforming and graphite formation on Ni catalysts', *Journal of Catalysis* **209**(2), 365 – 384.

Benziger, J. and Madix, R. J. (1979), 'The decomposition of formic acid on Ni(100)', *SURFACE SCIENCE* **79**(2), 394 – 412.

Blaylock, D. W., Ogura, T., Green, W. H. and Beran, G. J. O. (2009), 'Computational investigation of thermochemistry and kinetics of steam methane reforming on Ni(111) under realistic conditions', *The Journal of Physical Chemistry C* **113**(12), 4898–4908.

Boisen, A., Janssens, T., Schumacher, N., Chorkendorff, I. and Dahl, S. (2010), 'Support effects and catalytic trends for water gas shift activity of transition metals', *Journal of Molecular Catalysis A: Chemical* **315**(2), 163 – 170.

Busca, G., Montanari, T., Resini, C., Ramis, G. and Costantino, U. (2009), 'Hydrogen from alcohols: IR and flow reactor studies', *Catalysis Today* **143**(1-2), 2 – 8.

Campbell, C. T. (1994), 'Future directions and industrial perspectives micro- and macro-kinetics: Their relationship in heterogeneous catalysis', *Topics in Catalysis* **1**, 353–366.

Cao, D.-B., Li, Y.-W., Wang, J. and Jiao, H. (2009), 'CO_2 dissociation on Ni(2 1 1)', *SURFACE SCIENCE* **603**(19), 2991 – 2998.

CASTEP (n.d.). Available at http://www.cse.scitech.ac.uk/cmg/networks/ukpc/castep.shtml on February 2011

Catapan, R. C., Christiansen, M. A., Oliveira, A. A. M. and Vlachos, D. G. (to be published), *Heterogeneous Catalysis at the Nanoscale for Energy Applications*, Wiley-VCH.

Catapan, R., Oliveira, A., Salciccioli, M. and Vlachos, D. (2011), 'Water-gas shift reaction on Ni/Al_2o_3 catalysts: a DFT-driven microkinetic modeling approach', *in preparation* .

Chen, Y. and Vlachos, D. (2010*a*), Ethanol decomposition on Pt (111). in preparation.

Chen, Y. and Vlachos, D. G. (2010*b*), 'Hydrogenation of ethylene and dehydrogenation and hydrogenolysis of ethane on Pt(111) and Pt(211): A density functional theory study', *The Journal of Physical Chemistry C* **114**(11), 4973–4982.

Cheng, J., Hu, P., Ellis, P., French, S., Kelly, G. and Lok, C. M. (2010), 'Density functional theory study of iron and cobalt carbides for Fischer-Tropsch synthesis', *The Journal of Physical Chemistry C* **114**(2), 1085–1093.

Coltrin, M. E., Kee, R. J. and Rupley, F. M. (1991), 'Surface chemkin: A general formalism and software for analyzing heterogeneous chemical kinetics at a gas-surface interface', *International Journal of Chemical Kinetics* **23**(12), 1111–1128.

Comas, J., Mariño, F., Laborde, M. and Amadeo, N. (2004), 'Bio-ethanol steam reforming on Ni/Al_2o_3 catalyst', *Chemical Engineering Journal* **98**(1-2), 61 – 68.

DACAPO (n.d.). Available at https://wiki.fysik.dtu.dk/dacapo on February 2011.

Davis, J. and Barteau, M. (1988), 'The influence of oxygen on the selectivity of alcohol conversion on the pd(111) surface', *SURFACE SCIENCE* **197**(1-2), 123 – 152.

de Lima, S. M., da Cruz, I. O., Jacobs, G., Davis, B. H., Mattos, L. V. and Noronha, F. B. (2008), 'Steam reforming, partial oxidation, and oxidative steam reforming of ethanol over $Pt/CeZrO_2$ catalyst', *Journal of Catalysis* **257**(2), 356 – 368.

de Lima, S. M., da Silva, A. M., da Costa, L. O., Assaf, J. M., Jacobs, G., Davis, B. H., Mattos, L. V. and Noronha, F. B. (2010), 'Evaluation of the performance of Ni/La_2O_3 catalyst prepared from $LaNiO_3$ perovskite-type oxides for the production of hydrogen through steam reforming and oxidative steam reforming of ethanol', *Applied Catalysis A: General* **377**(1-2), 181 – 190.

Deng, J., Wang, J., Xu, X., Liao, Y. and Hong, B. (1995), 'In situ surface raman spectroscopy studies on the interaction between oxygen

and ethanol on electrolytic silver catalyst', *Catalysis Letters* **35**, 75–88.

Dumesic, J. (1999), 'Analyses of reaction schemes using de donder relations', *Journal of Catalysis* **185**(2), 496 – 505.

Fajardo, H. V. and Probst, L. F. D. (2006), 'Production of hydrogen by steam reforming of ethanol over Ni/Al_2O_3 spherical catalysts', *Applied Catalysis A: General* **306**, 134 – 141.

Fang, Y.-H. and Liu, Z.-P. (2010), 'Mechanism and tafel lines of electro-oxidation of water to oxygen on RuO_2(110)', *Journal of the American Chemical Society* **132**(51), 18214–18222.

Ferrin, P., Simonetti, D., Kandoi, S., Kunkes, E., Dumesic, J. A., Nørskov, J. K. and Mavrikakis, M. (2009), 'Modeling ethanol decomposition on transition metals: A combined application of scaling and brÃ¸nstedâ˜evansâ˜polanyi relations', *Journal of the American Chemical Society* **131**(16), 5809–5815.

Frenklach, M., Wang, H., Goldenberg, M., Smith, G. P., Golden, D. M., Bowman, C. T., Hanson, R. K., Gardiner, W. C. and Lissianski, V. (n.d.). http://www.me.berkeley.edu/gri_mech/ (Accessed April 1, 2010).

Gates, S., Jr., J. R. and Jr., J. Y. (1986), 'Bond activation sequence observed in the chemisorption and surface reaction of ethanol on Ni(111)', *SURFACE SCIENCE* **171**(1), 111 – 134.

Gokhale, A. A., Dumesic, J. A. and Mavrikakis, M. (2008), 'On the mechanism of low-temperature water gas shift reaction on copper', *Journal of the American Chemical Society* **130**(4), 1402–1414.

Goodman, D. W., Kelley, R. D., Madey, T. E. and Yates, J. T. (1980), 'Kinetics of the hydrogenation of CO over a single crystal nickel catalyst', *Journal of Catalysis* **63**(1), 226 – 234.

Goos, E., Burcat, A. and Ruscic, B. (2011), 'Ideal gas thermochemical database with updates from active thermochemical tables'. Available at http://garfield.chem.elte.hu/Burcat/burcat.html

Grabow, L. C., Gokhale, A. A., Evans, S. T., Dumesic, J. A. and Mavrikakis, M. (2008), 'Mechanism of the water gas shift reaction

on Pt: First principles, experiments, and microkinetic modeling', *The Journal of Physical Chemistry C* **112**(12), 4608–4617.

Grenoble, D. C., Estadt, M. M. and Ollis, D. F. (1981), 'The chemistry and catalysis of the water gas shift reaction : 1. the kinetics over supported metal catalysts', *Journal of Catalysis* **67**(1), 90 – 102.

Gu, X.-K. and Li, W.-X. (2010), 'First-principles study on the origin of the different selectivities for methanol steam reforming on Cu(111) and Pd(111)', *The Journal of Physical Chemistry C* **114**(49), 21539–21547.

Gursahani, K. I., Alcalá, R., Cortright, R. D. and Dumesic, J. A. (2001), 'Reaction kinetics measurements and analysis of reaction pathways for conversions of acetic acid, ethanol, and ethyl acetate over silica-supported Pt', *Applied Catalysis A: General* **222**(1-2), 369 – 392.

Hammer, B. (2001), 'Coverage dependence of n_2 dissociation at an N, O, or H precovered Ru(0001) surface investigated with density functional theory', *Phys. Rev. B* **63**(20), 205423.

Hammer, B., Hansen, L. B. and Nørskov, J. K. (1999), 'Improved adsorption energetics within density-functional theory using revised Perdew-Burke-Ernzerhof functionals', *PHYSICAL REVIEW B* **59**(11), 7413–7421.

Hansgen, D. A., Vlachos, D. G. and Chen, J. G. (2010), 'Using first principles to predict bimetallic catalysts for the ammonia decomposition reaction', *Nature Chemistry* **2**(6), 484–489.

Hilaire, S., Wang, X., Luo, T., Gorte, R. J. and Wagner, J. (2004), 'A comparative study of water-gas-shift reaction over ceria-supported metallic catalysts', *Applied Catalysis A: General* **258**(2), 271 – 276.

Hodgson, A. and Haq, S. (2009), 'Water adsorption and the wetting of metal surfaces', *Surface Science Reports* **64**(9), 381 – 451.

Hohenberg, P. and Kohn, W. (1964), 'Inhomogeneous electron gas', *PHYSICAL REVIEW* **136**(3B), B864–B871.

Honkala, K., Hellman, A., Remediakis, I. N., Logadottir, A., Carlsson, A., Dahl, S., Christensen, C. H. and Nørskov, J. K. (2005),

'Ammonia synthesis from first-principles calculations', *Science* **307**(5709), 555–558.

Houtman, C., Brown, N. and Barteau, M. (1994), 'The chemistry of acetates on the Rh(111) surface', *Journal of Catalysis* **145**(1), 37 – 53.

Huang, S.-C., Lin, C.-H. and Wang, J.-H. (2010), 'Trends of water gas shift reaction on close-packed transition metal surfaces', *The Journal of Physical Chemistry C* **114**(21), 9826–9834.

Inoglu, N. and Kitchin, J. R. (2010), 'Simple model explaining and predicting coverage-dependent atomic adsorption energies on transition metal surfaces', *PHYSICAL REVIEW B* **82**(4), 045414.

Jacobs, G., Chenu, E., Patterson, P. M., Williams, L., Sparks, D., Thomas, G. and Davis, B. H. (2004), 'Water-gas shift: comparative screening of metal promoters for metal/ceria systems and role of the metal', *Applied Catalysis A: General* **258**(2), 203 – 214.

Jelic, J. and Meyer, R. J. (2010), 'A density functional theory study of water gas shift over pseudomorphic monolayer alloy catalysts: Comparison with no oxidation', *Journal of Catalysis* **272**(1), 151 – 157.

Jensen, F. (2007), *Introduction to Computational Chemistry*, 2nd edn, Wiley: England.

Jiang, T., Mowbray, D. J., Dobrin, S., Falsig, H., Hvolbæk, B., Bligaard, T. and Nørskov, J. K. (2009), 'Trends in co oxidation rates for metal nanoparticles and close-packed, stepped, and kinked surfaces', *The Journal of Physical Chemistry C* **113**(24), 10548–10553.

Kapur, N., Hyun, J., Shan, B., Nicholas, J. B. and Cho, K. (2010), 'Ab initio study of CO hydrogenation to oxygenates on reduced Rh terraces and stepped surfaces', *The Journal of Physical Chemistry C* **114**(22), 10171–10182.

Kitchin, J. R., Nørskov, J. K., Barteau, M. A. and Chen, J. G. (2005), 'Trends in the chemical properties of early transition metal carbide surfaces: A density functional study', *Catalysis Today* **105**(1), 66 – 73.

Kohn, W. and Sham, L. J. (1965), 'Self-consistent equations including exchange and correlation effects', *PHYSICAL REVIEW* **140**(4A), A1133–A1138.

Kolasinski, K. W. (2008), *Surface Science: Foundations of Catalysis and Nanoscience*, 2nd edn, Wiley.

Koryabkina, N. A., Phatak, A. A., Ruettinger, W. F., Farrauto, R. J. and Ribeiro, F. H. (2003), 'Determination of kinetic parameters for the water-gas shift reaction on copper catalysts under realistic conditions for fuel cell applications', *Journal of Catalysis* **217**(1), 233 – 239.

Kresse, G. and Furthmüller, J. (1996), 'Efficient iterative schemes for ab initio total-energy calculations using a plane-wave basis set', *PHYSICAL REVIEW B* **54**(16), 11169–11186.

Lee, A. F., Gawthrope, D. E., Hart, N. J. and Wilson, K. (2004), 'A fast XPS study of the surface chemistry of ethanol over Pt111', *SURFACE SCIENCE* **548**(1-3), 200 – 208.

Li, M., Guo, W., Jiang, R., Zhao, L. and Shan, H. (2010), 'Decomposition of ethanol on Pd(111): A density functional theory study', *Langmuir* **26**(3), 1879–1888.

Liberatori, J., Ribeiro, R., Zanchet, D., Noronha, F. and Bueno, J. (2007), 'Steam reforming of ethanol on supported nickel catalysts', *Applied Catalysis A: General* **327**(2), 197 – 204.

Liguras, D. K., Kondarides, D. I. and Verykios, X. E. (2003), 'Production of hydrogen for fuel cells by steam reforming of ethanol over supported noble metal catalysts', *Applied Catalysis B: Environmental* **43**(4), 345 – 354.

Liu, Z.-P., Gong, X.-Q., Kohanoff, J., Sanchez, C. and Hu, P. (2003), 'Catalytic role of metal oxides in gold-based catalysts: A first principles study of CO oxidation on TiO_2 supported Au', *Phys. Rev. Lett.* **91**, 266102.

Madix, R. J., Gland, J., Mitchell, G. and Sexton, B. (1983), 'Identification of the intermediates in the dehydration of formic acid on Ni(110) by high resolution electron energy loss vibrational spectroscopy', *SURFACE SCIENCE* **125**(2), 481 – 489.

Maestri, M., Beretta, A., Faravelli, T., Groppi, G., Tronconi, E. and Vlachos, D. G. (2008), 'Two-dimensional detailed modeling of fuel-rich H2 combustion over Rh/Al_2O_3 catalyst', *CHEMICAL ENGINEERING SCIENCE* **63**(10), 2657 – 2669.

Mas, V., Baronetti, G., Amadeo, N. and Laborde, M. (2008), 'Ethanol steam reforming using Ni(II)-Al(III) layered double hydroxide as catalyst precursor: Kinetic study', *Chemical Engineering Journal* **138**(1-3), 602 – 607.

Mas, V., Bergamini, M., Baronetti, G., Amadeo, N. and Laborde, M. (2008), 'A kinetic study of ethanol steam reforming using a nickel based catalyst', *Topics in Catalysis* **51**, 39–48.

Mavrikakis, M. and Barteau, M. A. (1998), 'Oxygenate reaction pathways on transition metal surfaces', *Journal of Molecular Catalysis A: Chemical* **131**(1-3), 135 – 147.

Meng, S., Wang, E. G. and Gao, S. (2004), 'Water adsorption on metal surfaces: A general picture from density functional theory studies', *PHYSICAL REVIEW B* **69**(19), 195404.

Mezalira, D. Z., Probst, L. D., Pronier, S., Batonneau, Y. and Batiot-Dupeyrat, C. (2011), 'Decomposition of ethanol over Ni/Al_2O_3 catalysts to produce hydrogen and carbon nanostructured materials', *Journal of Molecular Catalysis A: Chemical* **340**(1-2), 15 – 23.

Mhadeshwar, A. B. and Vlachos, D. G. (2004), 'Microkinetic modeling for water-promoted CO oxidation, water-gas shift, and preferential oxidation of CO on Pt', *Journal of Physical Chemistry B* **108**(39), 15246–15258.

Mhadeshwar, A. B., Wang, H. and Vlachos, D. G. (2003), 'Thermodynamic consistency in microkinetic development of surface reaction mechanisms', *Journal of Physical Chemistry B* **107**(46), 12721–12733.

Mhadeshwar, A., Kitchin, J., Barteau, M. and Vlachos, D. (2004), 'The role of adsorbate-adsorbate interactions in the rate controlling step and the most abundant reaction intermediate of NH_3 decomposition on Ru', *Catalysis Letters* **96**, 13–22.

Mhadeshwar, A. and Vlachos, D. (2005*a*), 'Is the water-gas shift reaction on pt simple?: Computer-aided microkinetic model reduction, lumped rate expression, and rate-determining step', *Catalysis Today* **105**(1), 162 – 172.

Mhadeshwar, A. and Vlachos, D. (2005*b*), 'A thermodynamically consistent surface reaction mechanism for co oxidation on pt', *Combustion and Flame* **142**(3), 289 – 298.

Michaelides, A., Hu, P. and Alavi, A. (1999), 'Physical origin of the high reactivity of subsurface hydrogen in catalytic hydrogenation', *Journal of Chemical Physics* **111**(4), 1343–1345.

Ni, M., Leung, D. Y. and Leung, M. K. (2007), 'A review on reforming bio-ethanol for hydrogen production', *International Journal of Hydrogen Energy* **32**(15), 3238 – 3247.

Nørskov, J. K., Bligaard, T., Logadottir, A., Bahn, S., Hansen, L. B., Bollinger, M., Bengaard, H., Hammer, B., Sljivancanin, Z., Mavrikakis, M., Xu, Y., Dahl, S. and Jacobsen, C. J. H. (2002), 'Universality in heterogeneous catalysis', *Journal of Catalysis* **209**(2), 275 – 278.

Paier, J., Hirschl, R., Marsman, M. and Kresse, G. (2005), 'The Perdew-Burke-Ernzerhof exchange-correlation functional applied to the G2-1 test set using a plane-wave basis set', *Journal of Chemical Physics* **122**(23), 234102.

Pallassana, V. and Neurock, M. (2002), 'Reaction paths in the hydrogenolysis of acetic acid to ethanol over Pd(111), Re(0001), and PdRe alloys', *Journal of Catalysis* **209**(2), 289 – 305.

Pang, X.-Y., Wang, C., Zhou, Y.-H., Zhao, J.-M. and Wang, G.-C. (2010), 'DFT study of the structure sensitivity for the adsorption of methyl, methoxy, and formate on Ni(1 1 1), Ni(1 0 0), and Ni(1 1 0) surfaces', *Journal of Molecular Structure: THEOCHEM* **948**(1-3), 1 – 10.

Perdew, J. P. (1991), *Electronic Structure of Solids '91*, Akademie Verlag, Berlin.

Perdew, J. P., Burke, K. and Ernzerhof, M. (1996), 'Generalized gradient approximation made simple', *PHYSICAL REVIEW LETTERS* **77**(18), 3865–3868.

Phatak, A. A., Delgass, W. N., Ribeiro, F. H. and Schneider, W. F. (2009), 'Density functional theory comparison of water dissociation steps on Cu, Au, Ni, Pd, and Pt', *The Journal of Physical Chemistry C* **113**(17), 7269–7276.

Podkolzin, S. G., Alcala, R., de Pablo, J. J. and Dumesic, J. A. (2002), 'Monte Carlo simulations of reaction kinetics for ethane hydrogenolysis over Pt', *Journal of Physical Chemistry B* **106**(37), 9604–9612.

Prasad, V., Karim, A. M., Arya, A. and Vlachos, D. G. (2009), 'Assessment of overall rate expressions and multiscale, microkinetic model uniqueness via experimental data injection: Ammonia decomposition on Ru/Al_2O_3 for hydrogen production', *INDUSTRIAL & ENGINEERING CHEMISTRY RESEARCH* **48**(11), 5255–5265.

Raimondeau, S. and Vlachos, D. G. (2002), 'Recent developments on multiscale, hierarchical modeling of chemical reactors', *Chemical Engineering Journal* **90**(1-2), 3 – 23.

Remediakis, I. N., Abild-Pedersen, F. and Nørskov, J. K. (2004), 'DFT study of formaldehyde and methanol synthesis from CO and H_2 on Ni(111)', *Journal of Physical Chemistry B* **108**(38), 14535–14540.

Rostrup-Nielsen, J. and Nørskov, J. (2006), 'Step sites in syngas catalysis', *Topics in Catalysis* **40**, 45–48.

Salciccioli, M., Chen, Y. and Vlachos, D. G. (2010), 'Density functional theory-derived group additivity and linear scaling methods for prediction of oxygenate stability on metal catalysts: Adsorption of open-ring alcohol and polyol dehydrogenation intermediates on pt-based metals', *The Journal of Physical Chemistry C* **114**(47), 20155–20166.

Salciccioli, M., Chen, Y. and Vlachos, D. G. (2011), 'Microkinetic modeling and reduced rate expressions of ethylene hydrogenation and ethane hydrogenolysis on platinum', *INDUSTRIAL & ENGINEERING CHEMISTRY RESEARCH* **50**(1), 28–40.

Salciccioli, M., Stamatakis, M., Caratzoulas, S. and Vlachos, D. G. (2011), 'A review of multiscale modeling of catalytic reactions:

Mechanism development for complexity and emergent behavior', *CHEMICAL ENGINEERING SCIENCE* .

Sanchez-Escribano, V., Vargas, M. L., Finocchio, E. and Busca, G. (2007), 'On the mechanisms and the selectivity determining steps in syngas conversion over supported metal catalysts: An IR study', *Applied Catalysis A: General* **316**(1), 68 – 74.

Santiago, M. A. N., Sánchez-Castillo, M. A., Cortright, R. D. and Dumesic, J. A. (2000), 'Catalytic reduction of acetic acid, methyl acetate, and ethyl acetate over silica-supported copper', *Journal of Catalysis* **193**(1), 16 – 28.

Schulze, M., Reißner, R., Bolwin, K. and Kuch, W. (1995), 'Interaction of water with clean and oxygen precovered nickel surfaces', *FRESENIUS JOURNAL OF ANALYTICAL CHEMISTRY* **353**, 661–665.

Schumacher, N., Boisen, A., Dahl, S., Gokhale, A., Kandoi, S., Grabow, L., Dumesic, J., Mavrikakis, M. and Chorkendorff, I. (2005), 'Trends in low-temperature water-gas shift reactivity on transition metals', *Journal of Catalysis* **229**(2), 265 – 275.

Seelam, P., Huuhtanen, M., Sápi, A., Szabó, M., Kordás, K., Turpeinen, E., Tóth, G. and Keiski, R. (2010), 'CNT-based catalysts for H_2 production by ethanol reforming', *International Journal of Hydrogen Energy* **35**(22), 12588 – 12595.

Sehested, J. (2006), 'Four challenges for nickel steam-reforming catalysts', *Catalysis Today* **111**(1-2), 103 – 110. Frontiers in Catalysis: A Molecular View of Industrial Catalysis - Frontiers in Catalysis: A Molecular View of Industrial Catalysis.

Sehested, J., Dahl, S., Jacobsen, J. and Rostrup-Nielsen, J. R. (2005), 'Methanation of CO over nickel: Mechanism and kinetics at high H_2/CO ratios', *Journal of Physical Chemistry B* **109**(6), 2432–2438.

Seok, S.-H., Han, S. H. and Lee, J. S. (2001), 'The role of MnO in Ni/MnO-Al_2O_3 catalysts for carbon dioxide reforming of methane', *Applied Catalysis A: General* **215**(1-2), 31 – 38.

Sheng, P.-Y., Yee, A., Bowmaker, G. and Idriss, H. (2002), 'H_2 production from ethanol over Rh-Pt/CeO_2 catalysts: The role of

Rh for the efficient dissociation of the carbon-carbon bond', *Journal of Catalysis* **208**(2), 393 – 403.

Sholl, D. S. and Steckel, J. A. (2009), *Density Functional Theory: A Pratical Introduction*, John Wiley & Sons, Inc.

Shustorovich, E. and Sellers, H. (1998), 'The UBI-QEP method: A practical theoretical approach to understanding chemistry on transition metal surfaces', *Surface Science Reports* **31**(1-3), 1 – 119.

Silva, A., Costa, L., Barandas, A., Borges, L., Mattos, L. and Noronha, F. (2008), 'Effect of the metal nature on the reaction mechanism of the partial oxidation of ethanol over CeO_2-supported Pt and Rh catalysts', *Catalysis Today* **133-135**, 755 – 761.

Sim, W. S., Gardner, P. and King, D. A. (1996), 'Surface-bound helical polyacetaldehyde chains and bidentate acetate intermediates on Ag(111)', *Journal of the American Chemical Society* **118**(41), 9953–9959.

Skoplyak, O., Barteau, M. A. and Chen, J. G. (2008), 'Ethanol and ethylene glycol on Ni/Pt(111) bimetallic surfaces: A DFT and HREELS study', *SURFACE SCIENCE* **602**(23), 3578 – 3587.

Soler, J. M., Artacho, E., Gale, J. D., Garcia, A., Junquera, J., Ordejon, P. and Sanchez-Portal, D. (2001), 'The SIESTA method for ab initio order-N materials simulation', *Journal of Physics-Condensed Matter* **14**(11), 22.

Stamatakis, M., Chen, Y. and Vlachos, D. G. (2011), 'First-principles-based kinetic Monte Carlo simulation of the structure sensitivity of the water-gas shift reaction on platinum surfaces', *The Journal of Physical Chemistry C* **115**(50), 24750–24762.

Stuckless, J. T., Alsarraf, N., Wartnaby, C. and King, D. A. (1993), 'Calorimetric heats of adsorption for CO on nickel single-crystal surfaces', *Journal of Chemical Physics* **99**(3), 2202–2212.

Stuckless, J. T., Wartnaby, C. E., Al-Sarraf, N., Dixon-Warren, S. J. B., Kovar, M. and King, D. A. (1997), 'Oxygen chemisorption and oxide film growth on Ni(100), (110), and (111): Sticking probabilities and microcalorimetric adsorption heats', *Journal of Chemical Physics* **106**(5), 2012–2030.

Studt, F., Abild-Pedersen, F., Bligaard, T., Sørensen, R. Z., Christensen, C. H. and Nørskov, J. K. (2008), 'Identification of non-precious metal alloy catalysts for selective hydrogenation of acetylene', *Science* **320**(5881), 1320–1322.

Sun, J., Qiu, X.-P., Wu, F. and Zhu, W.-T. (2005), 'H_2 from steam reforming of ethanol at low temperature over Ni/Y_2O_3, Ni/La_2O_3 and Ni/Al_2O_3 catalysts for fuel-cell application', *International Journal of Hydrogen Energy* **30**(4), 437 – 445.

Sutton, J. and Vlachos, D. (2010), BEP correlations for C2 chemistry on surfaces. in preparation.

Tingcheng, L. (2003), Surface chemistry of organic carbonyl compounds and their derivatives on Ni (111), PhD thesis, National University of Singapore.

Titulaer, M. K., Jansen, J. B. H. and Geus, J. W. (1994), 'The quantity of reduced nickel in synthetic takovite: effects of preparation conditions and calcination temperature', *Clay Minerals Society* **42-3**, 249–258.

Troullier, N. and Martins, J. L. (1991), 'Efficient pseudopotentials for plane-wave calculations', *PHYSICAL REVIEW B* **43**(3), 1993–2006.

Vaidya, P. D. and Rodrigues, A. E. (2006*a*), 'Insight into steam reforming of ethanol to produce hydrogen for fuel cells', *Chemical Engineering Journal* **117**(1), 39 – 49.

Vaidya, P. D. and Rodrigues, A. E. (2006*b*), 'Kinetics of steam reforming of ethanol over a Ru/Al_2O_3 catalyst', *INDUSTRIAL & ENGINEERING CHEMISTRY RESEARCH* **45**(19), 6614–6618.

van Grootel, P. W., Hensen, E. J. and van Santen, R. A. (2009), 'DFT study on H_2O activation by stepped and planar Rh surfaces', *SURFACE SCIENCE* **603**(22), 3275 – 3281.

Vang, R. T., Honkala, K., Dahl, S., Vestergaard, E. K., Schnadt, J., Lægsgaard, E., Clausen, B. S., Nørskov, J. K. and Besenbacher, F. (2006), 'Ethylene dissociation on flat and stepped Ni(1 1 1): A combined STM and DFT study', *SURFACE SCIENCE* **600**(1), 66 – 77.

VASP (n.d.). Available at http://cms.mpi.univie.ac.at/vasp/ on February 2011.

Vesselli, E., Rogatis, L. D., Ding, X., Baraldi, A., Savio, L., Vattuone, L., Rocca, M., Fornasiero, P., Peressi, M., Baldereschi, A., Rosei, R. and Comelli, G. (2008), 'Carbon dioxide hydrogenation on Ni(110)', *Journal of the American Chemical Society* **130**(34), 11417–11422.

Wambach, J., Illing, G. and Freund, H. J. (1991), 'CO_2 activation and reaction with hydrogen on Ni(110): formate formation', *Chemical Physics Letters* **184**(1-3), 239 – 244.

Wang, E. D., Xu, J. B. and Zhao, T. S. (2010), 'Density functional theory studies of the structure sensitivity of ethanol oxidation on palladium surfaces', *The Journal of Physical Chemistry C* **114**(23), 10489–10497.

Wang, G., Wang, H., Tang, Z., Li, W. and Bai, J. (2009), 'Simultaneous production of hydrogen and multi-walled carbon nanotubes by ethanol decomposition over Ni/Al_2O_3 catalysts', *Applied Catalysis B: Environmental* **88**(1-2), 142 – 151.

Wang, J.-H., Lee, C. S. and Lin, M. C. (2009), 'Mechanism of ethanol reforming: Theoretical foundations', *The Journal of Physical Chemistry C* **113**(16), 6681–6688.

Wang, S.-G., Liao, X.-Y., Hu, J., Cao, D.-B., Li, Y.-W., Wang, J. and Jiao, H. (2007), 'Kinetic aspect of CO_2 reforming of CH_4 on Ni(1 1 1): A density functional theory calculation', *SURFACE SCIENCE* **601**(5), 1271 – 1284.

Watwe, R., Bengaard, H., Rostrup-Nielsen, J., Dumesic, J. and Nørskov, J. (2000), 'Theoretical studies of stability and reactivity of CH_x species on Ni(111)', *Journal of Catalysis* **189**(1), 16 – 30.

Wei, J. and Iglesia, E. (2004), 'Isotopic and kinetic assessment of the mechanism of reactions of CH_4 with CO_2 or H_2O to form synthesis gas and carbon on nickel catalysts', *Journal of Catalysis* **224**(2), 370 – 383.

Wheeler, C., Jhalani, A., Klein, E. J., Tummala, S. and Schmidt, L. D. (2004), 'The water-gas-shift reaction at short contact times', *Journal of Catalysis* **223**(1), 191 – 199.

Xie, C., Chen, Y., Li, Y., Wang, X. and Song, C. (2011), 'Influence of sulfur on the carbon deposition in steam reforming of liquid hydrocarbons over CeO_2-Al_2O_3 supported Ni and Rh catalysts', *Applied Catalysis A: General* **394**(1-2), 32 – 40.

Xu, J. and Froment, G. F. (1989), 'Methane steam reforming, methanation and water-gas shift: I. intrinsic kinetics', *AICHE JOURNAL* **35**(1), 88–96.

Yamakata, A., Kubota, J., Kondo, J. N., Hirose, C., Domen, K. and Wakabayashi, F. (1997), 'In situ observation of the dehydration of formate on Ni(110)', *Journal of Physical Chemistry B* **101**(26), 5177–5181.

Yee, A., Morrison, S. and Idriss, H. (1999), 'A study of the reactions of ethanol on CeO_2 and Pd/CeO_2 by steady state reactions, temperature programmed desorption, and in situ FT-IR', *Journal of Catalysis* **186**(2), 279 – 295.

Yee, A., Morrison, S. and Idriss, H. (2000), 'The reactions of ethanol over M/CeO_2 catalysts: Evidence of carbon-carbon bond dissociation at low temperatures over Rh/CeO_2', *Catalysis Today* **63**(2-4), 327 – 335.

Yeo, Y. Y., Vattuone, L. and King, D. A. (1997), 'Calorimetric heats for CO and oxygen adsorption and for the catalytic CO oxidation reaction on Pt111', *Journal of Chemical Physics* **106**(1), 392–401.

Zhai, Y., Pierre, D., Si, R., Deng, W., Ferrin, P., Nilekar, A. U., Peng, G., Herron, J. A., Bell, D. C., Saltsburg, H., Mavrikakis, M. and Flytzani-Stephanopoulos, M. (2010), 'Alkali-stabilized Pt-OH_x species catalyze low-temperature water-gas shift reactions', *Science* **329**(5999), 1633–1636.

Zhang, C. J., Hu, P. and Lee, M. H. (1999), 'A density functional theory study on the interaction between chemisorbed CO and S on Rh(111)', *SURFACE SCIENCE* **432**(3), 305 – 315.

Zhou, Y.-H., Lv, P.-H. and Wang, G.-C. (2006), 'DFT studies of methanol decomposition on Ni(1 0 0) surface: Compared with Ni(1 1 1) surface', *Journal of Molecular Catalysis A: Chemical* **258**(1-2), 203 – 215.

Zhu, Y.-A., Chen, D., Zhou, X.-G. and Yuan, W.-K. (2009), 'DFT studies of dry reforming of methane on Ni catalyst', *Catalysis Today* **148**(3-4), 260 – 267.

APPENDIX A - ENNERGIES IN VACUUM OF THE SPECIES AND RADICALS

Table A1. Energy in vacuum for the species calculated in this work.

Species	E [eV]	Species	E [eV]
CH_3OO	-1069.750017	CCOO	-1173.25767
CH_3OOH	-1086.753639	CCOOH	-1190.82247
$C(OH)_2$	-1055.228674	CH_2COO	-1208.7782
$H_2C(OH)_2$	-1089.332539	CH_2COOH	-1226.740901
H_2COO	-1053.318719	CH_3COO	-1226.641659
H_2COOH	-1071.429295	CH_3COOH	-1244.587805
$HC(OH)_2$	-1071.548916	CHCOO	-1193.273809
HCOOH	-1057.297661	CHCOOH	-1208.480594
HCOO	-1039.2256	CCOH	-754.779139
OCOO	-1456.464936	CCO	-739.29081
		CC	-300.945784

Table A2. Energy in vacuum for the species taken from the in-house database (Chen and Vlachos, 2010a).

Species	E [eV]	Species	E [eV]	Species	E [eV]
CH_3CH_2OH	-841.0382	CH_3OH	-653.9304	CH_3CH_3	-405.9389
CH_3CHOH	-823.3895	CH_2OH	-636.1794	CH_3CH_2	-388.0693
CH_2CH_2OH	-822.9983	CHOH	-618.7323	CH_3CH	-369.6297
CH_3COH	-805.1869	COH	-601.8491	CH_2CH_2	-372.571
CH_2CHOH	-807.9091	CH_3O	-635.7306	CH_3C	-352.0914
$CHCH_2OH$	-804.8175	CH_2O	-621.0223	CH_2CH	-354.047
CHCHOH	-789.4631	CHO	-603.5847	CHCH	-338.532
CH_2COH	-789.6498	CO	-588.7894	CH_2C	-336.8839
CCH_2OH	-787.2203	O_2	-867.2017	CHC	-319.2814
CCHOH	-771.5935	O from O_2	-433.60085	CH_4	-219.1484
CHCOH	-773.5005	O	-430.8268	CH_3	-200.9495
CH_3CH_2O	-823.0438	H_2	-31.4029	CH_2	-182.6079
CH_3CHO	-808.4119	H from H_2	-15.70145	CH	-163.7439
CH_2CH_2O	-807.3647	H	-13.5759	C	-147.21115
CH_2CHO	-790.7148	H_2O	-467.4604		
CH_3CO	-790.5234	OH	-448.4849		
CHCHO	-772.4775	COOH	-1039.4477		
CH_2CO	-775.1999	CO_2	-1025.4623		
CHCO	-757.1027				
$CHCH_2O$	-787.0399				
CCH_2O	-772.7085				
CCHO	-755.036				

APPENDIX B - SUMMARY OF THE DFT CALCULATIONS OF THE WGS ADSORBATES AND REACTIONS

Table B1 - Detailed data for the adsorbates on the Ni (111) surface.

	Energy [eV]			
2x2x4 slab	-19993.65355			
3x3x4 slab	-44985.74428			
Adsorbate	**atop**	**bridge**	**hcp**	**fcc**
C*	-20145.16174	-20146.96527	**-20147.47508**	-20147.41603
CH*	n.a.	n.a.	n.a.	**-20164.23858**
CHO*	n.a.	**-20599.73126**	n.a.	n.a.
CO*	-20584.15194	-20584.36759	**-20584.53597**	-20584.52218
COH*	n.a.	n.a.	n.a.	**-20599.91951**
CO_2*	**-21019.23777**	-21019.20924	n.a.	n.a.
trans-COOH*	-21035.26375	**-21035.6425**	n.a.	-21035.50806
cis-COOH*	-21034.27391	-21034.03085	n.a.	-21035.22226
H*	-20009.40644	-20009.84418	-20009.98365	**-20009.99965**
H_2O*	**-20461.57967**	-20461.40504	-20461.26670	-20461.27029
HCOO*	**-21035.89445**	-21035.26234	n.a.	n.a.
mono_HCOO*	n.a.	n.a.	-21035.07703	n.a.
O*	-20427.52141	-20428.76221	-20429.15678	**-20429.29025**
OH*	-20444.41756	-20445.17562	-20445.34906	**-20445.48254**

Table B2 - Detailed data for the adsorbates on the Ni (211) surface.

	Energy [eV]					
2x1x12 slab	-29989.83905					
Adsorbate	**t1**	**br1**	**h1**	**4-fold**	**br1_d**	**h1_d**
C*	-30141.23269	-30142.78158	-30143.64978	**-30144.50095**	n.a.	n.a.
CH*	n.a.	n.a.	-30160.29849	**-30160.60513**	n.a.	n.a.
CHO*	-30595.67096	-30595.88781	n.a.	**-30595.94402**	n.a.	n.a.
CO*	n.a.	-30580.60053	**-30580.71920**	-30579.74957	-30580.46350	-30579.71389
COH*	n.a.	n.a.	**-30596.04045**	-30593.67494	n.a.	n.a.
CO_2*	**-31015.60640**	-31015.46194	n.a.	n.a.	n.a.	n.a.
COOH*	**-31031.81744**	-31031.33350	n.a.	n.a.	n.a.	n.a.
H*	-30005.57003	-30006.06150	**-30006.14713**		n.a.	n.a.
H_2O*	**-30458.02185**	n.a.	n.a.	-30457.85569	-30457.94370	n.a.
HCOO*	**-31032.47944**	n.a.	n.a.	n.a.	n.a.	n.a.
O*	-30424.02296	-30425.22464	**-30425.47944**	n.a.	n.a.	-30425.11939
OH*	-30440.97086	**-30441.79742**	-30441.77734	n.a.	-30441.17907	n.a.

Table B3 - Detailed data for surface reactions on Ni (111) and (211) surfaces used to derive BEP correlations in the Chapter 3.

Elementary step	Ni (111)		Ni (211)	
	E_{FS} [kJ/mol]	E_{TS} [kJ/mol]	E_{FS} [kJ/mol]	E_{TS} [kJ/mol]
C-H and O-H bond breaking				
$CO_2^* + H^* \rightleftharpoons HCOO^* + *$	-308.8	-208.4	-347.3	-225.8
$CHO^* + * \rightleftharpoons CO^* + H^*$	-351.2	-221.0	-347.3	-207.4
$H_2O^* + * \rightleftharpoons H^* + OH^*$	-68.5	42.5	-78.2	7.7
$OH^* + * \rightleftharpoons H^* + O^*$	-337.7	-224.8	-333.8	-221.9
$CO_2^* + H^* \rightleftharpoons COOH^* + 2^*$	-284.6	-199.7	-283.7	-223.8
$COH^* + * \rightleftharpoons CO^* + H^*$	-519.1	-344.5	-515.2	-339.6
C-O bond breaking				
$CO_2^* \rightleftharpoons CO^* + O^*$	-102.3	45.3	-102.3	50.2
$COOH^* + * \rightleftharpoons CO^* + OH^*$	-314.5	-196.8	-327.1	-189.1
$COH^* + O^* \rightleftharpoons COOH^* + *$	-898.3	-753.6	-897.3	-769.0
$CHO^* + O^* \rightleftharpoons HCOO^*$	-755.5	-633.9	-794.1	-650.3
$C^* + O^* \rightleftharpoons CO^* + *$	-1238.9	-948.5	-1238.9	-955.2
$CHO^* + * \rightleftharpoons CH^* + O^*$	-254.7	-116.7	-272.1	-160.2
$C^* + OH^* \rightleftharpoons COH^* + *$	-1019.9	-820.1	-1014.1	-913.7

APPENDIX C - ATOMIC COORDINATES, SURFACE REACTION MECHANISM AND THERMODYNAMIC DATABASE

Attached to the present thesis, there is a DVD with all data required to reproduce the results presented. The objective is to provide a database to allow the reader the reproduction of the DFT results presented in the Chapter 3 and 5 as well as the microkinetic modeling results presented in the Chapters 4 and 6.

The list of the data attached includes:

Appendix C.1 - Coordinates of the water-gas shift adsorbates and reactions on Ni (111) (Chapter 3);

Appendix C.2 - Coordinates of the water-gas shift adsorbates and reactions on Ni (211) (Chapter 3);

Appendix C.3 - Surface reaction mechanism of the water-gas shift on Ni in CHEMKIN format (Chapter 4);

Appendix C.4 - Coordinates of the ethanol steam reforming adsorbates and reactions on Ni (111) (Chapter 5);

Appendix C.5 - Surface reaction mechanism of the ethanol steam reforming on Ni in CHEMKIN format (Chapter 6);

Appendix C.6 - Thermodynamic database of adsorbates on Ni in CHEMKIN format (Chapter 4 and 6).

Fell free to contact the author for any questions:

Rafael de Camargo Catapan
rcatapan@yahoo.com.br
catapan@labcet.ufsc.br